# DESIGN AND MODELING OF A MEMS-BASED ACCELEROMETER WITH PULL IN ANALYSIS


by

Akila Kannan

B. E. (Electrical and Electronics Engineering), Anna University, 2005


A THESIS SUBMITTED IN PARTIAL FULFILLMENT OF

THE REQUIREMENTS FOR THE DEGREE OF

Master of Applied Science

in

THE FACULTY OF GRADUATE STUDIES

(Electrical & Computer Engineering)

THE UNIVERSITY OF BRITISH COLUMBIA

(Vancouver)

October 2008

# Abstract

This thesis reports the design and modelling of a MEMS (Micro Electro Mechanical system) based inertial accelerometer. The main motivation to design a differential type of accelerometer is that such a kind of structure allows differential electrostatic actuation and capacitive sensing. They can be operated at the border of stability also so that the "pull in" operation mode can be explored. Such kinds of structures have a wide range of applications because of their high sensitivity. One is in the field of minimally invasive surgery where accelerometers will be combined with gyroscopes to be used in the navigation of surgical tools as a inertial micro unit (IMU). The choice for the design of a structure with 1 Degree of Freedom(DOF) , instead of a 2-DOF device was instigated by the simplicity of the design and by a more efficient 1-DOF dynamic model. The accelerometers were designed and optimized using the MATLAB simulator and COVENTORWARE simulation tool. First set of devices is fabricated using a commercial foundry process called SOIMUMPs. The simulation tests show that the SOI accelerometer system yields 8.8kHz resonant frequency, with a quality factor of 10 and 2.12mV/g sensitivity. To characterize the accelerometer a new semi automatic tool was formulated for the noise analysis and noise based optimization of the accelerometer design and the analysis estimation shows that there is a trade off between the S/N ratio and the sensitivity and for the given design could be made much better in-terms of S/N by tuning its resonant frequency.

# Table of Contents

# List of Tables

# List of Figures

# Acronyms

**MEMS** Micro Electro Mechanical Systems

**SOI** Silicon On Insulator

**IMU** Inertial Micro Unit

**MIS** Minimally Invasive Surgery

**MUMPS** Multi User MEMS Process

**DOF** Degree of Freedom

**DSP** Digital Signal Processing

# Acknowledgements

I would like to express my deep and sincere gratitude to my supervisor, Dr.Edmond Cretu, whose personal and professional guidance has motivated me to perform better all the time. His wide knowledge and constructive guidance has helped me in completing my thesis on time with success. I would like to thank Dr. Lukas Chrostowski's and Dr. Mu Chiao for kindly providing simulation and characterization tools and instruments. I would also like to thank CMC Microsystems for their help in providing us with softwares like Coventorware for simulations.I would also like to acknowdge Miguel Angel Guillen-Torres and Mrigank Sharma for their helpful discussions and suggestions regarding my research. I would also like to thank the undergraduate student, Mohammed Al-Taha for helping out with the read out circuit. Above all I am grateful to my family and friends Mohit Bhatnagar and Vijayalakshmi Sridhar for their constant words of encouragement and moral support.

*"I dedicate this thesis to my family who mean the world to me"*

# 1 INTRODUCTION

Micro machined inertial sensors consisting of accelerometers and gyroscopes are one of the most important types of silicon-based sensors. Micro accelerometers alone have the second largest sales volume after pressure sensors. The first micro machined accelerometer was designed in the year 1979 at Stanford University but ever since the device has been the most popular MEMS device[1]. The large volume demand for accelerometers is due to their diversified applications which covers a much broader spectrum where their small size and low cost have even a larger impact.

An accelerometer is defined as a "*device that can be used for measuring linear acceleration.*" They can be used to measure tilt, inertial acceleration and shocks or vibration as shown in Figure 1-1..

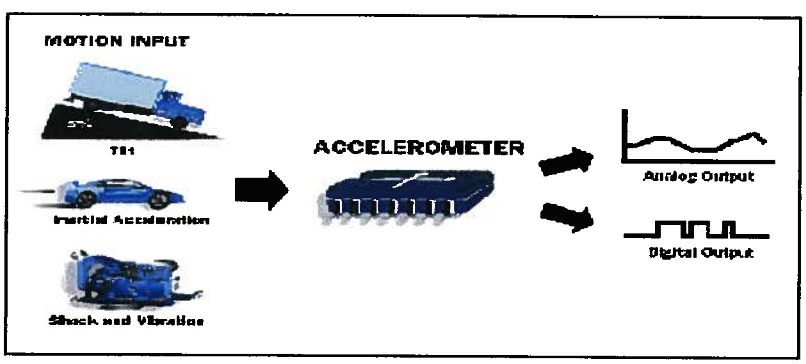


Figure 1-1. .The Fuctionality of an Accelerometer

To extract the acceleration value, the sensor has a movable proof mass which is connected to a fixed frame via spring structures. An external acceleration will displace the proof mass from its rest position. The magnitude of this displacement is proportional to the magnitude of the acceleration and inversely proportional to the stiffness of the spring structures. Hence, the acceleration input that is applied to the sensor is converted to the proof mass displacement in the sensor. The sensor then extracts the magnitude of this displacement using its sensing scheme.

One can divide the sensors as [2]:

* Out-of-plane accelerometers where the sensitive axis is perpendicular to the wafer surface.

*In-Plane accelerometers where the sensitive axis parallel to the wafer plane.

Out-of-plane accelerometers were the first designs to be proposed. But In-plane accelerometers offer the following advantages: (i) fabrication of beams and seismic mass in one etching step, and (ii) a high degree of symmetry which allows one to increase the seismic mass without changing its gravitational center[3].

### 1.0.1. Applications of Accelerometers

Acceleration is a measure of the physical characteristic of any system. The measurement of acceleration is used as an input into some types of control systems. The control systems use the measured acceleration to correct for the changing dynamic conditions.Acceleration is usually measured in (ft/s)/s or (m/s)/s. But we use a more universally accepted factor "g"($m/s^2$). A"$g$" is a unit of acceleration equal to the Earth's gravity at sea-level which is equal to $32.2 ft/s^2$ or $9.8 m/s^2$.

Table 1-1. Some common "g" reference points[4]

| **Description** | **"g" level** |
|---:|---:|
| Earth's Gravity | 1g |
| Parked car | 1g |
| Bumps in a road | 2g |
| Car Driver in a corner | 3g |
| Bobsled driver in a corner | 5g |
| Human Unconsciousness | 7g |
| Orbiting Space Shuttle | 10g |

Depending on the characteristics, there is diverse range of applications for accelerometers. The sensitivity, resolution, size, cost etc. are some of the factors that determine the type of the applications for the accelerometer. Based on this its wide rage of applications include mlitary,aerospace,medical systems,navigation,automotive industry. This is shown in Figure1-2. The typical functions an accelerometer can be used are [4]:

- Tilt/Roll Sensing
- Vibration-Can be used to isolate vibration of the mechanical system from the outside sources.*Example:*Rough Road detection.
- Vehicle Skid Detection- Often used with systems that deploy smart breaking to regain the control of vehicle.
- To determine the severity of the impact or to log when an impact has occurred.
- Input/Feedback for active suspension control systems- keeps the vehicle level.

- Lately it has been used in medical industry along with micro gyroscopes which form a microinetrial unit which helps in the navigation of the tools during surgeries.

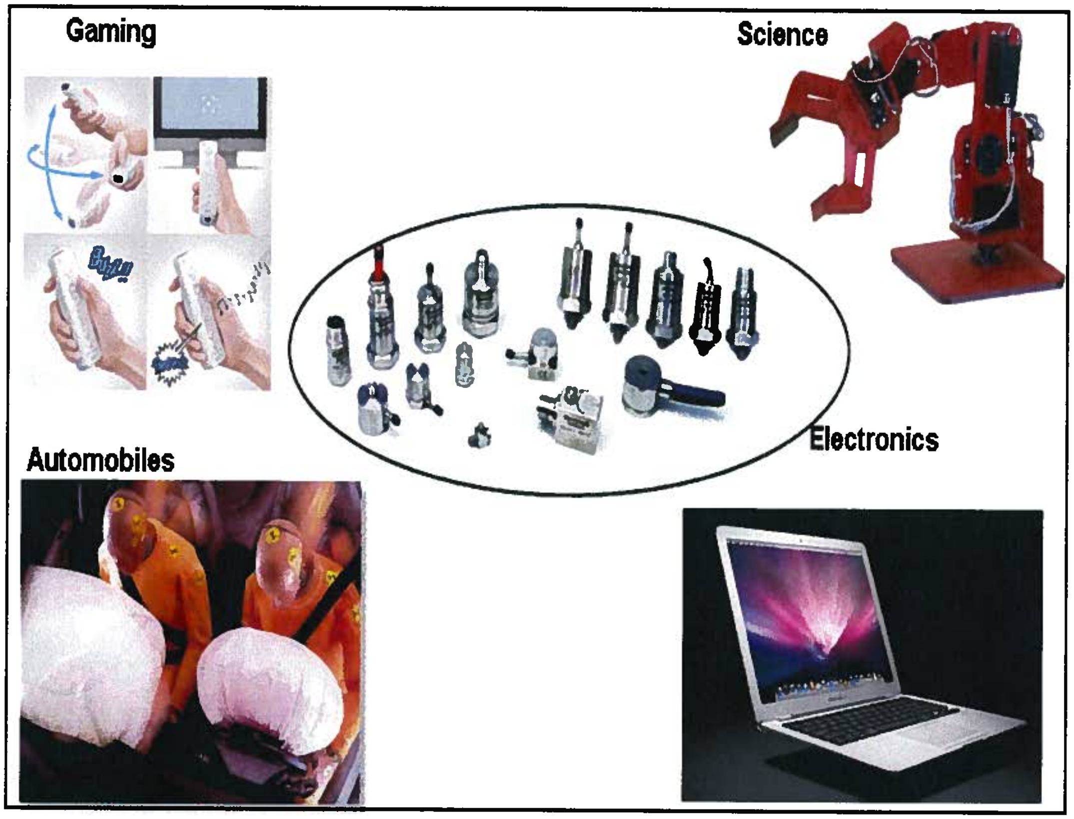


Figure 1-2. The different application areas for accelerometers [5]

## 1.1. TYPES OF ACCELEROMETERS

There are different types of accelerometers which are classified on the basis of transduction principle. Some of them include Capacitive, Piezoresistive, Piezoelectric, Tunnelling, Optical, Heat Transfer, Hall Effect,Thermal, Interferometric etc.A few of the types are explained below:

- Capacitive-Metal beam or micro machined feature produces capacitance; change in capacitance related to acceleration[1].

- Piezoelectric-Piezoelectric crystal mounted to mass -voltage output converted to acceleration[6].
- Piezoresistive-Beam or micro machined feature whose resistance changes with acceleration[7].
- Hall Effect-Motion converted to electrical signal by sensing of changing magnetic fields[8].
- Magneto resistive-Material resistivity changes in presence of magnetic field[9].
- Heat Transfer-Location of heated mass tracked during acceleration by sensing temperature[10].
- Tunneling-A cantilever structure with a variable gap between an integrated tunneling tip and a conducting electrode causes electron tunneling in the gap and this principle can be used to detect extremely sensitive accelerations[11].
- Interferometric- The inter digital system forms an optical diffraction grating where the displacement of the proof mass relative to the support substrate is measured with a standard laser diode and photo detector[12].

Of these different types of accelerometers, differential capacitive sensing and actuation mechanism is chosen as the principle of the design. One of the main reasons that a capacitive scheme is used is because of its high sensitivity and wide range of applications [1].

## 1.2. Overview and Motivation

There are several kinds of accelerometers available commercially. The main question that would tend to arise will be the significance of this particular accelerometer.The reason for choosing capacitive accelerometer is because of its following advantages:

- High Sensitivity
- Repeatability
- Temperature Stability
- Design Flexibility
- Low cost and power usage

The main disadvantage is the complex read out circuit design and one such possible design has been proposed using a 555 timer circuit. This project is motivated by the fact that the accelerometer will be integrated with a MEMS gyroscope and will be used as an inertial cluster in minimally invasive surgery. This would help in navigation of the surgical tool more reliably and quickly. Medical navigation systems are mainly used for monitoring the position of surgical instruments relative to patient body. The idea is to attach the micro-inertial measurement unit (IMU) to the instrument to track its position. The MEMS-based unit will comprise of accelerometers as well as gyroscopes, together with associated electronics. A low cost, high precision IMU encompasses in fact a much larger application horizon, ranging from medical to automotive field. One of the main goals is to improve the resolution and accuracy of the present MEMS-based inertial sensors. The presently available resolutions of (commercial) MEMS sensors are in the range of mg for accelerometers, and around 0.1deg/sec for gyroscopes. Advanced medical navigation systems require sensing linear accelerations in the micro-g or lower ranges and very high sensitivities.

The main objective of this study to construct an accelerometer system which has satisfactory noise-floor/nonlinearity performance for IMUs and is powered with ±12 DC batteries. The system is to yield a voltage output proportional to the externally applied acceleration. The Table1-2 below summarizes the performance goals of this accelerometer system.

Table 1-2. Performance Goals Targeted

| Parameter | Performance Goals |
|---|---|
| Sensitivity | 1 V/g |
| NonLinearity | 1% |
| Noise Drift | 500μg/Hz$^{1/2}$ |
| Bias Drift | 20mg |
| Quality Factor | 10 |
| Resonant Frequency | 10kHz |

## 1.3. THESIS ORGANISATION

*Chapter 1* gives a basic outline to the thesis. *Chapter 2* explains some basic principles about accelerometers and *Chapter 3* describes the device design together with the simulations that were performed on CoventorWare© 2006 and Matlab along with the explanation of the fabrication process. *Chapter 4* shows the experimental measurements and explains the pull in operation mode of the accelerometer with numerical simulations to confirm the theory. It also explains the device characterization and optimization. The *fifth Chapter* explains the application for which this accelerometer is designed. The *last chapter* presents the conclusion and the future work which includes the read out electronics associated with the device and a possible future design.

# 2 THERORETICAL BACKGROUND

## 2.1. Review of the Basic Principles

Before proceeding to the device design, there are some theoretical concepts that are needed to be understood which help in explaining the fundamental principles of the accelerometer better. This chapter reviews the mechanics and electronics of a MEMS device and later explains the principle of operation of an accelerometer.

### 2.1.1. Basic Mechanics

Lets begin with defining the various mechanical quantities. Stress is the defined as the force per unit area acting on the surface of a differential volume element of a solid body. The equation shows that when F is the applied force acting along an element with cross sectional area A.

$$\text{Stress}(\sigma) = \frac{F}{A}\ [N/m^2]$$

Another important mechanical term is the strain, which can be defined as the deformation resulting from a stress, and measured as the ratio of deformation to the total dimension of the body in which the deformation is occurred. The deformation depends on the direction of the applied force. The compressive force causes the body to be shortened and the tensile force causes the body to be stretched. The normal strain is formulated as:

$$\varepsilon = \frac{\text{Change in the amount of Deformation}}{\text{Original Dimension}} = \frac{\delta}{L}$$

The Figure 2.1 shows the Stress-Strain relationship of a general material[13].

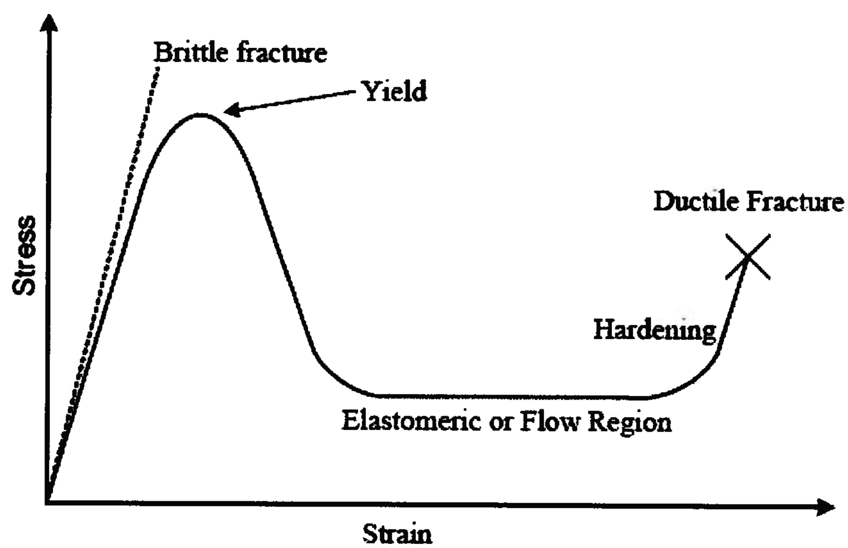


Figure 2-1. Stress-Strain relationship of a general material.

In a MEMS design, designers try to stay in the linear region of this graph where the strain values are relatively small. In this linear region, another mechanical property of the materials known as Young's Modulus is an important term in MEMS design. This is the proportionality constant in this linear region and can be expressed as:

$$E = \frac{\sigma}{\varepsilon}\ [\text{Pa}]$$

Moment of inertia of an area with respect to an axis is the sum of the products obtained by multiplying the infinitesimal area elements by the distance of this element from the axis. Moment of inertia is denoted by I and can be expressed as:

$$I = \int y^2 dA$$

*where* dA is the infinitesimal area element and y is the distance of this area element to the origin of interest.

#### 2.1.1.1. Spring Constant

The spring constants are an important parameter to which determine the characteristics of the sensor. The spring constant or the force constant as its otherwise called is the proportionality constant that relates the force and the displacement in Hooke's law. By increasing or decreasing the spring constant we can alter the movement of the proof mass in the corresponding direction.

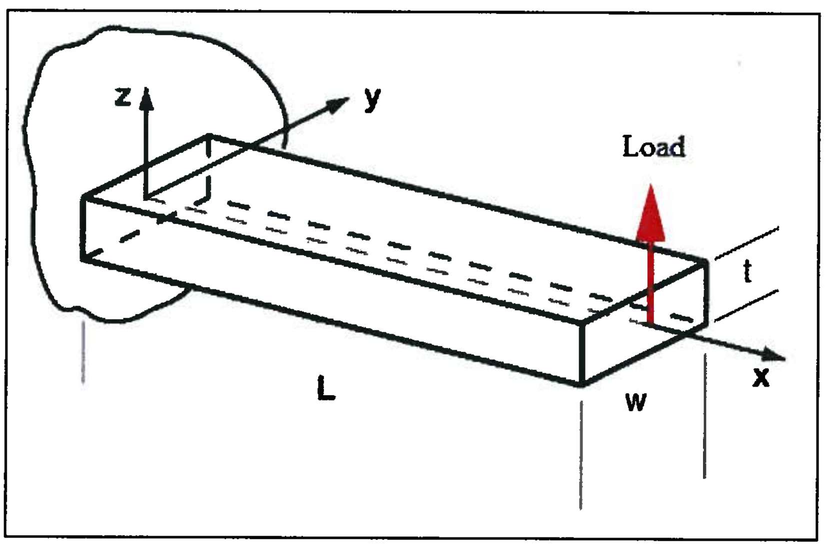


Figure 2-2. A simple beam at its rest position

The above figure 2-2 shows a simple beam at its initial postion.The spring constant will depend on the direction of application of force. The most common example is a cantilever Beam which is fixed at one end. All the translational and rotational degree of freedom are fixed at one end. Deflection of a cantilever beam condition is the basic condition to be analyzed. The spring constants for this condition along each direction are calculated as:

$$k_x = \frac{Etw}{l} \qquad k_y = \frac{Etw^3}{4l^3} \qquad k_z = \frac{Et^3w}{4l^3}$$

*where* the direction index denotes the direction of the applied force which bends the spring beam, E is the Young's Modulus, t is the thickness, w is the width, and l is the length of the beam. Spring constants for various shape beams can be extracted similarly using parallel series connection springs idea.

Figure 2-3 shows different beam structures that can be used in any sensor design.

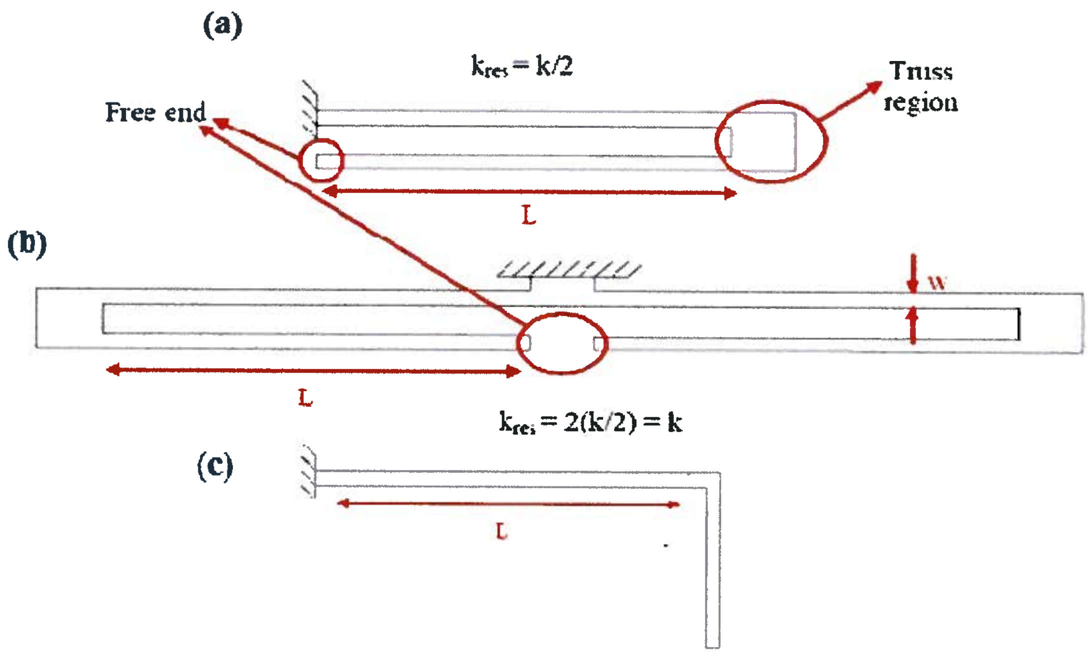


Figure 2-3. Different types of beams used in MEMS sensors

Based on the requirement the beams can be made stiffer or flexible in a certain direction. Usually the stiffness of beams is increased by adding truss as a sub-beam section. But one needs to precalculate the stiffness requirement cause making the beam too stiff can even lead to breakage of the beam. Also as in the case of a flexural vibrating fixed-fixed beam, the transverse deflection can cause the stretching of the neutral axis and this effect is called "hardening effect" of the springs. Due to this phenomenon, the resonant frequency increases. When the beam is not anchored firmly, the reverse phenomenon occurs which causes "softening" effect and here the resonant frequency decreases.

### 2.1.2. Capacitance Basics

MEMS capacitance configurations can be characterized into three parts. First one is parallel plate capacitor configuration where the capacitance is formed between two parallel plates, second one is transverse comb capacitance configuration, and the third one is lateral comb capacitance configuration. First two configurations are used generally in sensing elements, and the last configuration is generally used in actuating schemes, due to its linear force-voltage relationship.Capacitance, sensitivity, electrostatic force, and electrostatic spring constant are the main performance metrics for the performances of the capacitance configurations.

Table 2-1. shows the definitions of performance parameters [13]

| | |
|---|---|
| Capacitance | $N\varepsilon\frac{A}{d}$ |
| Sensitivity | $\frac{\partial C}{\partial x}$ |
| Electrostatic Force | $\frac{1}{2}\frac{\partial C}{\partial x}V^2$ |
| Electrostatic Force Constant | $\frac{1}{2}\frac{\partial^2 C}{\partial x^2}V^2$ |
| *where* N is the number of capacitance plate pairs, A is the overlapping area and d is the distance between the plates. | |

### 2.1.2.1. Parallel Plate Capacitor

Figure 2-4 shows the parallel plate configuration. In this configuration there are two plates that are parallel to each other and the capacitance formed between these plates changes when the distance between these plates changes. This configuration is generally used to sense in the z-axis sensing schemes. Due to the possibility of large capacitance areas, this configuration may result very high sensitivity, but the main disadvantage of this configuration is the non-linear force and sensitivity values, which occurs with the movement of one of the plates towards the other.

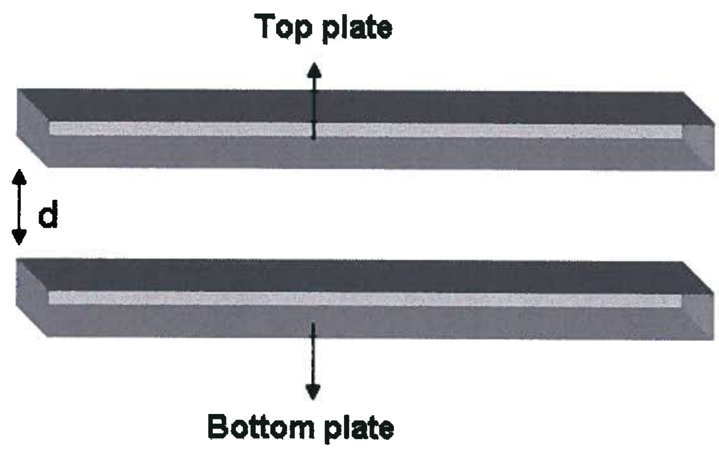


Figure 2-4. Parallel Plate Capacitor

.The table 2-2 summarizes the performance parameters for a parallel plate capacitor.

Table 2-2. Performance Metrics for a parallel Plate Capacitor[13]

| | |
|---|---|
| Capacitance | $N\varepsilon\frac{A}{d-x}$ |
| Sensitivity | $-N\varepsilon\frac{A}{(d-x)^2}$ |
| Electrostatic Force | $-\frac{1}{2}N\varepsilon\frac{A}{(d-x)^2}V^2$ |
| Electrostatic Force Constant | $N\varepsilon\frac{A}{(d-x)^3}V^2$ |

Another important parameter is the electrostatic spring constant. If the electrostatic spring constant trying to pull two electrodes towards each other is greater than the mechanical spring constant in that direction, "Pull-in" occurs. Analyses show that pull-in occurs when the distance of the two electrodes become 2/3 of the original distance. The voltage difference applied to the electrodes that causes pull-in is called pull-in voltage and can be calculated as[14]

$$V_{\text{pull-in}} = \sqrt{\frac{8d^3 k_{\text{mech}}}{27\varepsilon A}}$$

#### 2.1.2.2. Transverse Comb Capacitance Configuration

In this configuration there is a movable electrode between two stationary electrodes. Due to this differential topology, this configuration shows an almost linear force-displacement and voltage-displacement relationship. In addition to linearity, this configuration gives a high sensitivity due to varying distance topology. The nonlinearity comes from fringing field capacitances and this effect is reduced if high aspect ratio fingers are used.

Electrostatic force and electrostatic spring constant calculations for this configuration require a clear explanation of voltage sources applied to the electrodes. In this configuration, the general connection is to apply 0 and $V_0$ to fixed electrodes and to apply $V_0/2$ to the mid-electrode. The force occurs when the mid-electrode is not in the mid-point of two stationary electrodes. In fact, if the fixed electrodes are all applied with $V_0$ and the mid-electrode is applied with $V_0/2$, the same force expression can be found. In fact to case

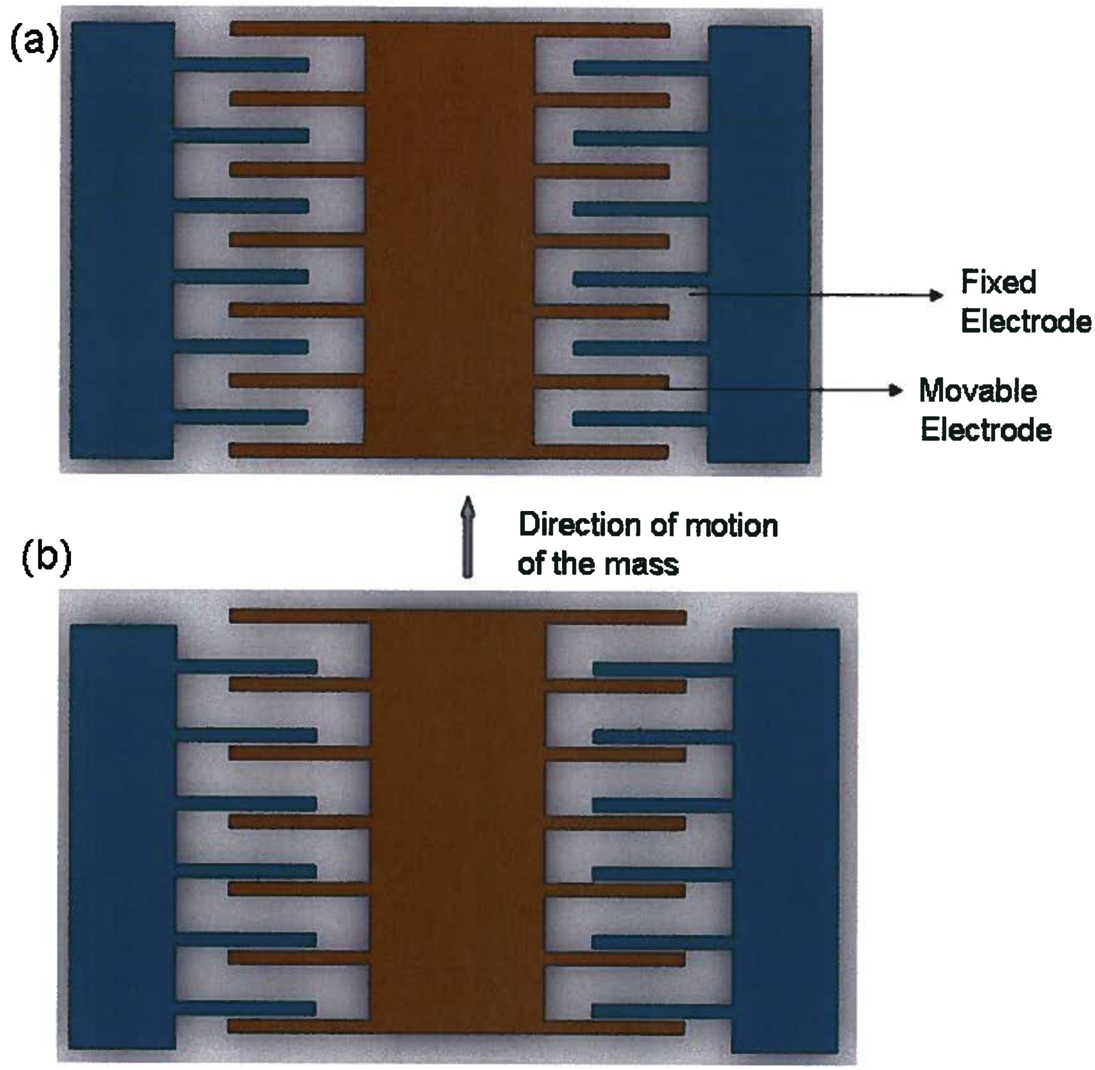


Figure 2-5. Transverse comb configuration:

(a) Before Movement (b) After Movement

that difference in electrostatic force so that the electrostatic force are unequal, there is an initial unequal difference between the electrodes as shown in figure 2-6.

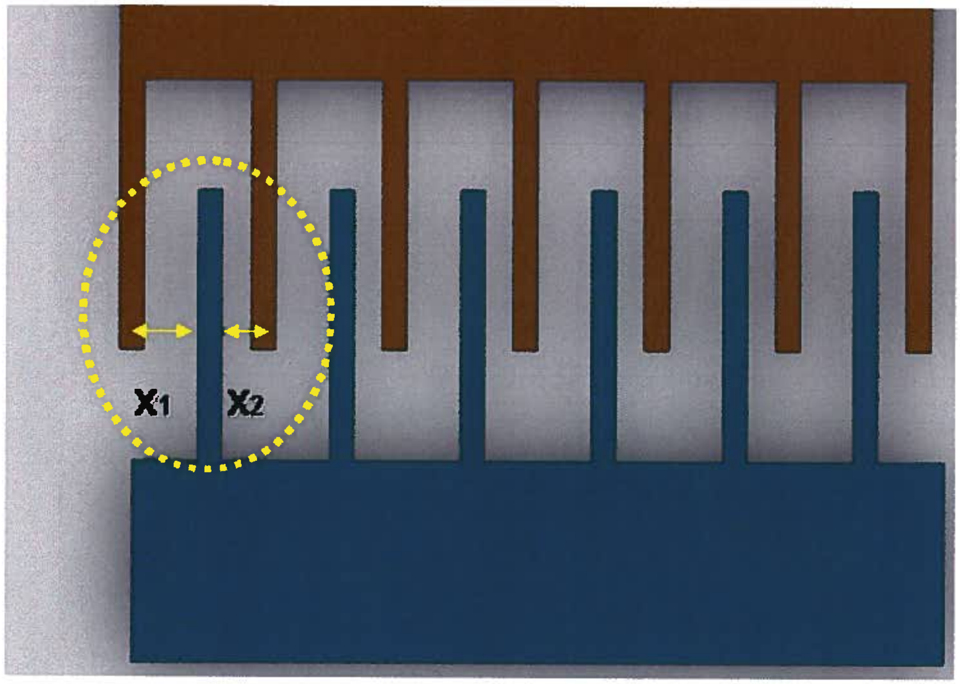


Figure 2-6. Zoomed in view of the transverse configuration

Table 2-3 summarizes the performance metrics of transverse comb capacitance configuration.

Table 2-3. Performance Metrics of a Transverse Comb Capacitance Configuration[13]

| | |
|---|---|
| Capacitance | $2C_0 = 2N\varepsilon\frac{A}{d}$ |
| Sensitivity | $\frac{C_0}{d}$ |
| Electrostatic Force | $2x\frac{C_0}{d^2}V^2$ |
| Electrostatic Force Constant | $2\frac{C_0}{d^2}V^2$ |

#### 2.1.2.3. Lateral Comb Configuration

In this configuration the capacitance forms between two combs looking each other. The change of the capacitance is formed by the change of the distance of these combs. This configuration shows a constant force-displacement characteristic, hence does not form an electrostatic spring constant, but has a very poor sensitivity due to varying overlap area topology. Due to this linearity and poor sensitivity this configuration is generally used in the actuating parts of the sensors. The table 2-4 gives the performance metrics of the configuration.

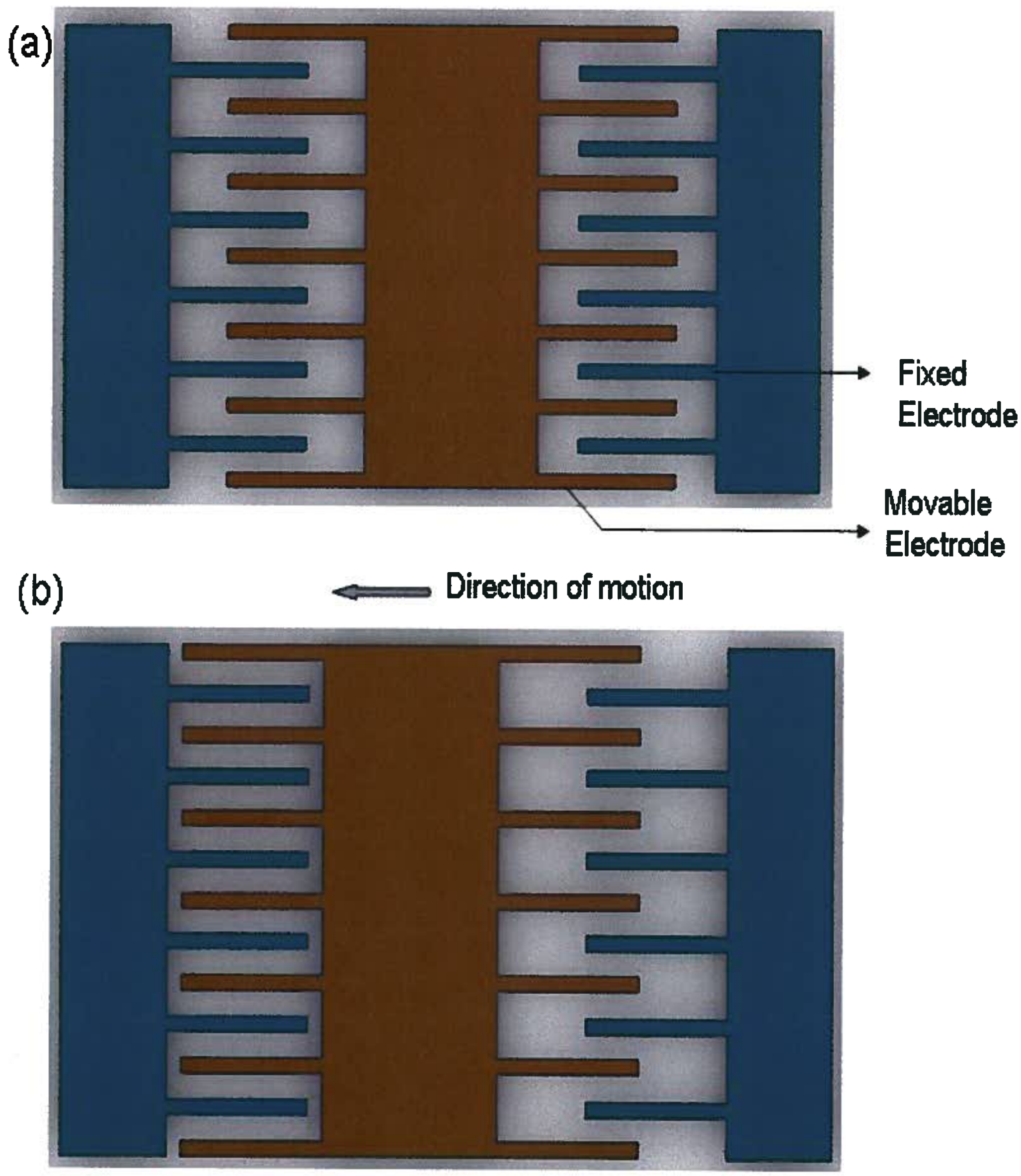


Figure 2-7. Lateral comb configuration:

(a) Before movement and (b) After movement

Table 2-4. Performance metrics of a Lateral Comb Configuration[13]

| | |
|---|---|
| Capacitance | $N\varepsilon\frac{A}{d}$ |
| Sensitivity | $N\varepsilon\frac{h}{d}$ |
| Electrostatic Force | $N\varepsilon\frac{h}{d}V^2$ |
| Electrostatic Force Constant | 0 |

## 2.2. Principle of Operation on an Accelerometer

An accelerometer generally consists of a proof mass suspended by compliant beams anchored to a fixed frame. The proof mass has a mass of m, the suspension beams have an effective spring constant stiffness k and there is a damping factor (b) affecting the dynamic movement of the mass generated by the air-structure interaction. The accelerometer can be modeled by a second-order Mass-damper-spring system, as shown in Fig. 2-8. External acceleration displaces the support frame relative to the proof mass, which in turn changes the internal stress in the suspension spring. Both this relative displacement and the suspension-beam stress can be used as a measure of the external acceleration.

The operation of the accelerometer can be modelled as a second order mechanical system. When force is acted upon on the accelerometer, the mass develops a force which is given by the D'Alembert's inertial force equation F= m*a. This force displaces the

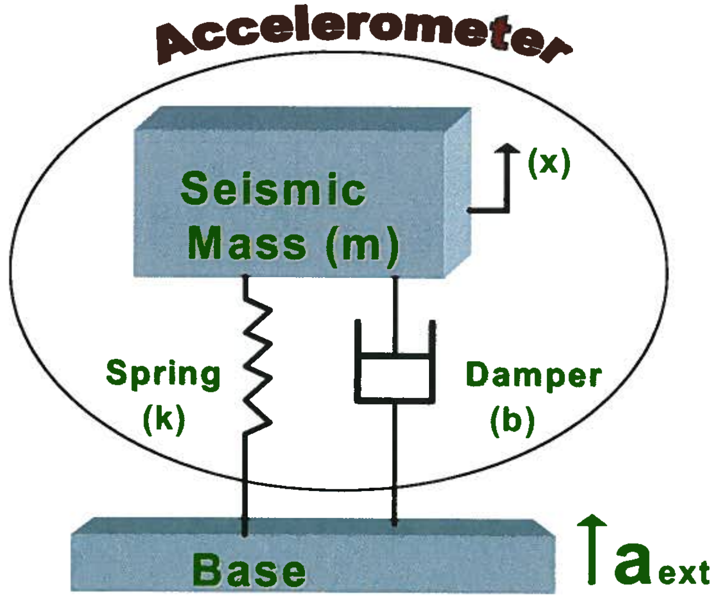


Figure 2-8. Dynamic Model of an Accelerometer

spring by a distance x. Hence the total force externally is balanced by the sum of internal forces given by,

$$F_{external} = F_{inertial} + F_{damping} + F_{spring}$$

The dynamic equation of the system vibration along the x direction can be given by the differential equation[15],

$$m\frac{d^2}{dt^2}x(t) + b\frac{d}{dt}x(t) + kx(t) = ma(t)$$

*where* 'm' is the mass of the system,'x(t)' is the displacement,'b' is the damping coefficient,'k' is the elastic spring constant and 'a(t)' is the acceleration. By using Newton's second law and the accelerometer model, the mechanical transfer function can be obtained,

$$H(s) = \frac{X(s)}{A(s)} = \frac{m}{ms^2 + bs + k} = \frac{1}{s^2 + 2\zeta\omega_r s + \omega_r^2}$$

*where*

Resonant Frequency $(\omega_r) = \sqrt{\frac{k}{m}}$ Damping Ratio$(\zeta) = \frac{b}{2\sqrt{km}}$ Quality Factor(Q) $= \frac{\sqrt{km}}{b}$

The resonant frequency is the frequency where the system has its sharp peak in amplitude.The range of frequencies for which the system oscillates is the bandwidth of the system. The Quality factor is the factor that defines the sharpness of the system.

Considering the dynamic equation, the characteristics equations given by

$$\lambda_{1,2} = -\zeta\omega_r \pm \omega_r\sqrt{\zeta^2 - 1}$$

From the above equation we can conclude that 3 different homogenous solution are possible based on the value of the damping ratio $\zeta$.

Case 1: $0<\zeta<1$ (underdamped - overshoot and oscillation)

$$x_n(t) = Ce^{-\zeta\omega_r t}\sin\omega_r\sqrt{1-\zeta^2}t \text{ -}\theta$$

Case 2: $\zeta$=1 (critically damped- shortest rise time and no overshoot)

$$x_n(t) = C_1 e^{\lambda_1 t} + C_2 e^{\lambda_2 t}$$

Case 3: $\zeta$>1 (overdamped - slowest rise time and no overshoot)

$$x_n(t) = C_1 e^{\lambda_1 t} + C_2 e^{\lambda_2 t}$$

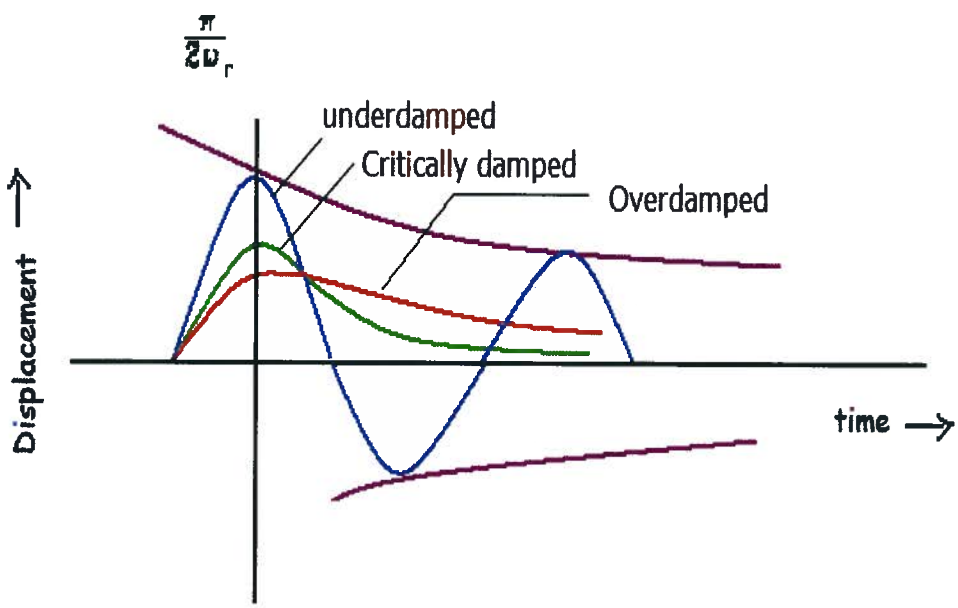


Figure 2-9. Step Response of a second order system

Under steady state conditions the static sensitivity (S) of the accelerometer is shown to be

$$S = \frac{m}{k} = \frac{1}{\omega_r^2}$$

The magnitude and phase response of the proof mass motion with respect to input acceleration can be derived as:

$$\left|\frac{X(j\omega)}{A(j\omega)}\right| = \frac{1}{\sqrt{(\omega_0^{\,2} - \omega_r^{\,2})^2 + \frac{\omega_r\omega_0}{Q}}}$$

$$\angle\frac{X(j\omega)}{A(j\omega)} = \tan^{-1}\left(\frac{\frac{\omega_r\omega_0}{Q}}{\omega_0^{\,2} - \omega_r^{\,2}}\right)$$

Figure 2-10(a) shows the plot of the magnitude of proof mass displacement under a constant magnitude external acceleration versus acceleration frequency. The accelerometer is operated in the low frequency region of this plot due to the fact that the response is almost constant. The magnitude of the response in this linear region is inversely proportional to the square of the resonance frequency of the accelerometer. Hence, the mechanical resonance frequency is a very important parameter determining the performance of the accelerometer. The length of this linear region is called the effective bandwidth of the accelerometer. The effective bandwidth of the accelerometer is a design goal and the designer should design the accelerometer properly to achieve reasonably small response errors in that bandwidth.

As evident, the resonance frequency of the structure can be increased by increasing the spring constant and decreasing the proof mass, while the quality factor of the device can be increased by reducing damping and by increasing proof mass and spring constant.

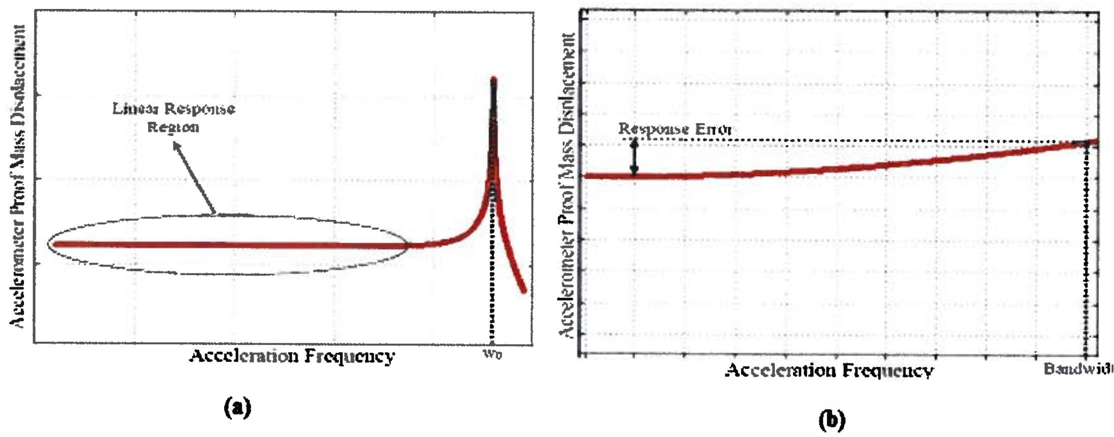


Figure 2-10. Accelerometer proof mass displacement under a constant amplitude acceleration versus acceleration frequency and (b) the response error

Last, the static sensitivity of the device can be increased by reducing its resonant frequency.

The primary mechanical noise source for the device is due to Brownian motion of the gas molecules surrounding the proof mass and the Brownian motion of the proof mass suspension or anchors. The total noise equivalent acceleration (TNEA) m/s$^2$)[16] is

$$\text{TNEA}=\frac{\sqrt{4k_B T b}}{m}$$

*where* $k_B$ is the Boltzmann constant and T is the temperature in kelvin. The equation clearly shows that to reduce mechanical noise, the quality factor and proof mass have to be increased.

### 2.2.1. Open Loop Accelerometer

The accelerometer discussed above is a perfect example of an open loop accelerometer. The figure 2-11 shows a simple schematic of operation of an open loop system.

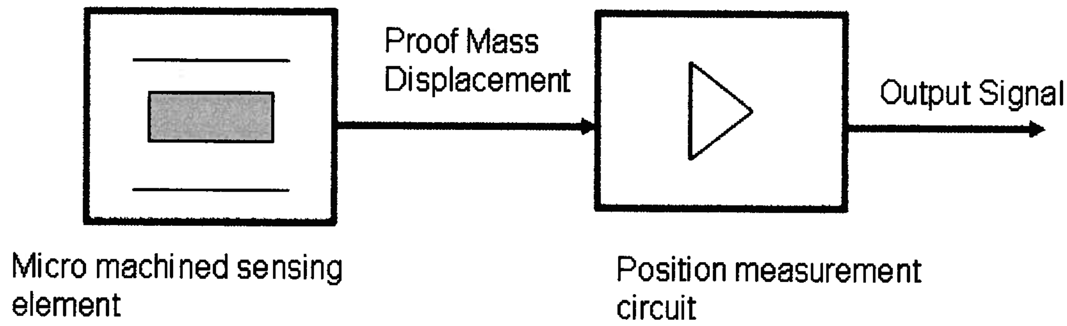


Figure 2-11. Open Loop Accelerometer

In this case, the electrical output signal of the position interface circuit is used directly to measure the external acceleration. The main advantages of such a system are its simplicity in design and low cost. But there are various disadvantages to this method. They include non linearity introduced into the system through the form of noise, drift etc. Also damping of the system will lower the amplitude of oscillations. Cross-sensitivities will also be high in this case.

### 2.2.2. Closed Loop Accelerometer

To overcome the disadvantages mentioned for a open loop system, often a feedback system is used to stabilize the system. Here the output signal from the position measurement of the interface circuit together with a suitable controller is used to actuate or drive the proof mass to its rest position. Thus the electric signal proportional to this feedback force is proportional to the input acceleration. The force feedback stabilizes the system and hence the performance of the system is improved. This greatly reduces the non linear effects caused due to damping. Also the sensitivity of the system can be increased by using a good controller scheme. The main disadvantage of such a closed loop system is the increased complexity and cost of system.

There are various controlling or feedback techniques used. These include magnetic, thermal and electrostatic. The type of actuating mechanism usually depends on the requirements and the application. In case of magnetic schemes, the actuation is done by changing the magnetic fields and in the case of thermal the operating principle is based on temperature variations. The most common and preferred scheme uses electrostatic principles. This is because in case of capacitive accelerometers, the same electrodes can be used for sensing and actuating. The problem to overcome in case of electrostatic principles are that electrostatic forces are always attractive and non linear because $F_{electrostatic}$ is directly proportional to the $(Voltage)^2$ and inversely proportional to the distance between the electrodes. Two common types of electrostatic feedback mechanisms are explained:

**(i) Analog Force Feedback system**

This is schematically shown in figure 2-12. Assuming the proof mass is at 0 potential at the bottom electrode, there will be a net electrostatic force acting on the system given by,

$$Force = F_1 - F_2 = \frac{1}{2}\varepsilon A \left[\frac{(V_B + V_F)^2}{(d-x)^2} - \frac{(V_B - V_F)^2}{(d+x)^2}\right]$$

where $V_B$ is the bias voltage at the electrode, $V_F$ is the feedback voltage, d is the distance between the electrodes and x is the displacement. Under a close loop feedback system the displacement is smaller when compared to the distance.Hence assuming that x--> 0, the equation is simplified to

$$F \approx -2\varepsilon A \frac{V_B V_F}{d^2}$$

This force is linear and has the desired negative feedback aimed.

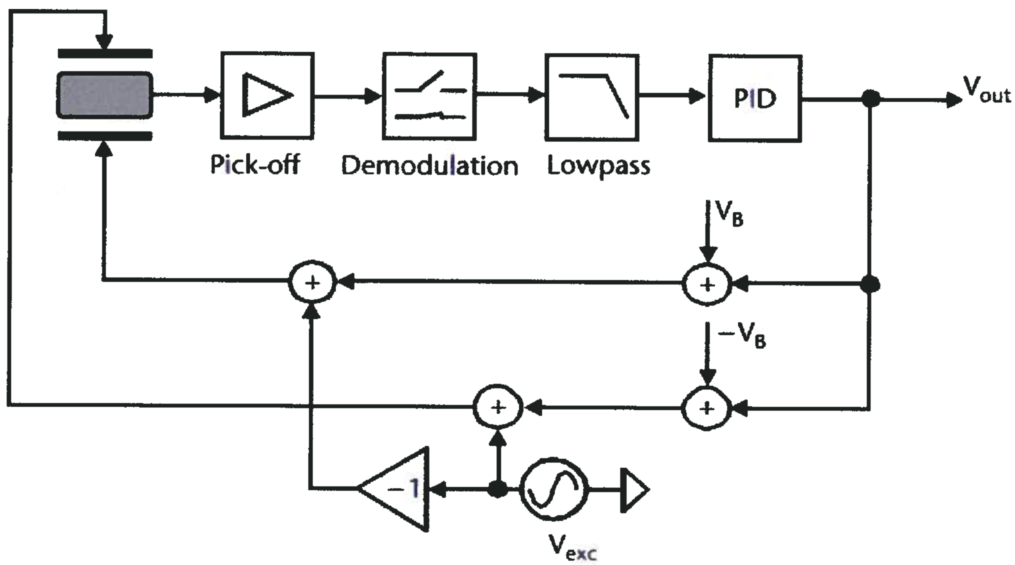


Figure 2-12. Capacitive Accelerometer in a Closed Loop System (with Analog force feedback loop)

### (i) Digital Force Feedback system

The main disadvantage of the analog feedback mechanism is that when the proof mass is deflected further away from its nominal position, then the electrostatic forces become nonlinear and hence this causes the feedback force to have a reversal in its polarity. This means that the electrodes would get stuck to or pulled towards each other. This concept is also called the pull-in mechanism. To overcome this disadvantage, in the recent times digital feedback system have been increasingly used.The figure 2-13 shows the schematic of a digital feedback system.

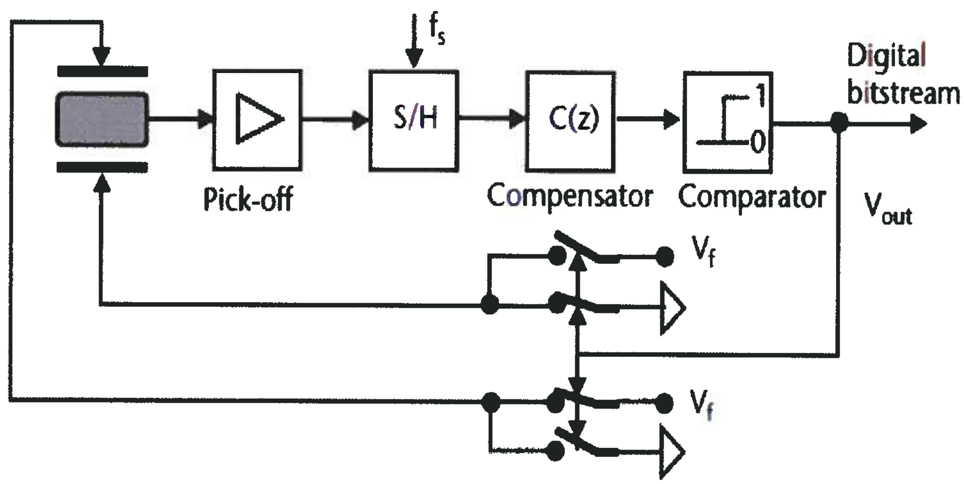


Figure 2-13. Capacitive Accelerometer in a Closed Loop System (with Digital Force Feedback)

In this system, the additional components include a comparator which gets the information about the extent of displacement of the proof mass and accordingly the compensator stabilizes the system. The comparator controls a range of switches which applies a feedback voltage to the electrode depending on the position of the proof mass while the other electrode is grounded. This is done for a fixed time interval, which is locked to the sampling frequency of the comparator. As with their electronic counterpart, this electromechanical sigma-delta modulator is an oversampling system; hence, the clock frequency has to be many times higher than the bandwidth of the sensor.

This method not only prevents the pull-in but also makes the system more convinient. Since the output signal is already digital in nature, it can be directly fed to a Digital

Signal Processor (DSP) for further processing of the signal. This makes the associated read out easy.

## 2.3. MEMS Capacitance Accelerometer Design

An inertial sensor like the accelerometer is a micro system by itself which may include:

- A sensor that understands the information from the system
- An electronic circuit that processes the signals associated with the system
- An actuator which reacts to the signals produced in the system.

Capacitors can operate both as sensors and actuators. They have excellent sensitivity and their transduction mechanism is intrinsically insensitive to temperature.

### 2.3.1. Electrostatic Actuation

Electrostatic Actuation is based on the simple concept that unlike charges attract each other. Hence if there are two plates of different charges as shown in figure 2-14, there exists an electrostatic force between them.

Capacitive sensing is independent of the base material and relies on the variation of capacitance when the geometry of a capacitor is changing. Neglecting the fringing effect near the edges, the parallel-plate capacitance is

$$C_0 = \varepsilon_0 \varepsilon_r \frac{A}{d}$$

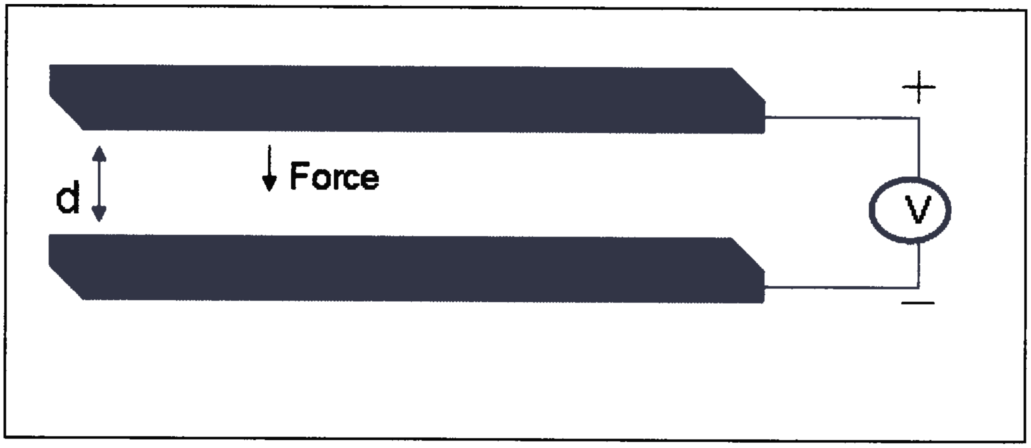


Figure 2-14. A simple parallel plate actuation principle

*where* A is the area of the electrodes, d the distance between them and $\varepsilon = \varepsilon_0\varepsilon_r$ is the permittivity of the material separating them. A change in any of these parameters will be measured as a change of capacitance and variation of each of the three variables has been used in MEMS sensing. For example, chemical or humidity sensors may be based on a change in permittivity whereas accelerometers are based on a change in distance or area. If the dielectric in the capacitor is air, capacitive sensing is essentially independent of temperature but contrary to piezoresistivity, capacitive sensing requires complex readout electronics. Still the sensitivity of the method can be very large.

The energy stored W is

$$W = \frac{1}{2}CV^2 = \frac{\varepsilon_0\varepsilon_r A V^2}{2d}$$

The electrostatic force is therefore given by differentiating W with respect to the distance of separation d,

$$F = \frac{\varepsilon_0 \varepsilon_r A V^2}{2d^2}$$

This equation shows that the force is a non linear function of the voltage and the distance.By varying the distance we can control the electrostatic force between the plates.

The type of actuation design used in this design is called the comb drive actuator.This is shown in figure 2-15.It consists of many interdigitated fingers that are actuated

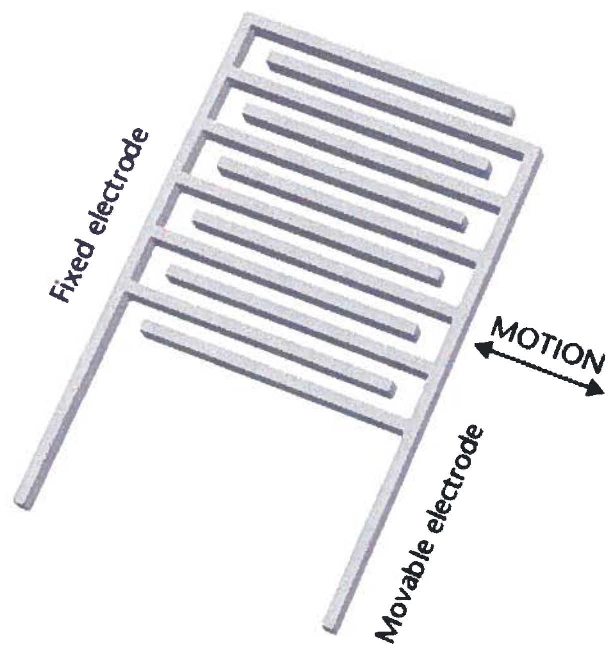

Figure 2-15. Electrostatic Comb Drive Actuator

by applying a voltage between them. The geometry is such that the thickness of the fingers is small in comparison to their lengths and widths.

The attractive forces are therefore mainly due to the fringing fields rather than the parallel plate fields, as seen in the simple structure above. The movement generated is in the lateral direction and because the capacitance is varied by changing the area of overlap and the gap remains fixed, the displacement varies as the square of the voltage. The fixed electrode is rigidly supported to the substrate, and the movable electrode must be held in place by anchoring at a suitable point away from the active fingers. Additional parasitic capacitances such as those between the fingers and the substrate and the asymmetry of the fringing fields can lead to out-of-plane forces, which can be minimized with more sophisticated designs.

Typical MEMS accelerometer is composed of movable proof mass with plates that is attached through a mechanical suspension system to a reference frame, as shown in Figure 2-16.

Movable plates and fixed outer plates represent capacitors. The deflection of proof mass is measured using the capacitance difference. The free-space (air) capacitances between the movable plate and two stationary outer plates $C_1$ and $C_2$ are functions of the corresponding displacements $x_1$ and $x_2$.If the acceleration is zero, the capacitances $C_1$ and $C_2$ are equal because $x_1 = x_2$. The proof mass displacement x results due to acceleration. If x not equal to 0, the capacitance on either side of the electrodes are found to be

$$C_1 = \varepsilon_o \varepsilon_r \frac{A}{d-x} = C_o \frac{d}{d-x}$$

$$C_2 = \varepsilon_o \varepsilon_r \frac{A}{d+x} = C_o \frac{d}{d+x}$$

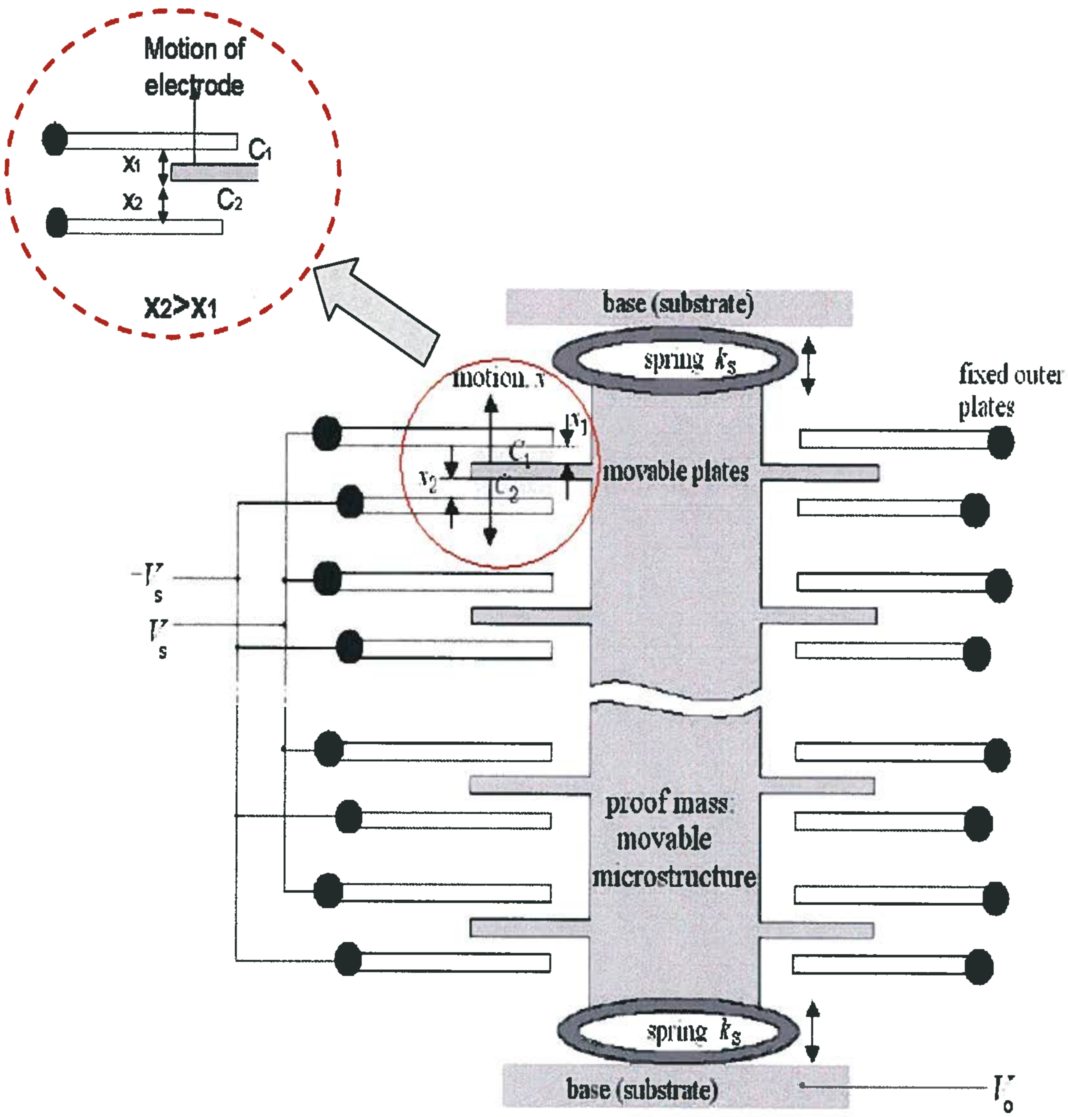


Figure 2-16. (a) Differential Capacitive Accelerometer

The differential capacitance is therefore found by,[18]

$$C_1 - C_2 = \Delta C = 2(\varepsilon_0 \varepsilon_r A)\left(\frac{x}{d^2 - x^2}\right)$$

$$\Delta C = 2C_o\left(\frac{xd}{d^2 - x^2}\right)$$

For only small displacements of x, $d^2 >> x^2$,

$$\Delta C \approx 2C_o\left(\frac{x}{d}\right)$$

We can conclude that the displacement is proportional to the capacitive difference.

Considering $V_s$ to be the voltage applied to actuate the system,

$$V_s = V_{DC} + V_{ac}\sin\omega t$$

The impedance Z is given by the equation,

$$Z = -j\left(\frac{1}{\omega C}\right)$$

The output Voltage of the proof mass is therefore

$$V_o = V_s - 2V_s\left(\frac{-\frac{j}{\omega C_1}}{-\frac{j}{\omega C_1} - \frac{j}{\omega C_2}}\right) = V_s - 2V_s\left(\frac{C_2}{C_2 + C_1}\right)$$

,

$$V_o = V_s\left(\frac{C_2 - C_1}{C_2 + C_1}\right) = \frac{x}{d}V_s$$

where

$$C_2 + C_1 = 2(\varepsilon_0\varepsilon_r A)\left(\frac{d}{d^2 - x^2}\right) \approx 2C_o$$

Finally making use of the basic principles outlined in the beginning of the chapter, the acceleration is formulated as shown below:

$$a = \frac{kd}{mV_s}V_o$$

### 2.3.2. Performance Characteristics of Accelerometers

Accelerometers are typically specified by their sensitivity, maximum operation range, frequency response, resonant frequency, resolution, full-scale nonlinearity, offset, off-axis sensitivity, and shock survival.Depending on the type of application one or more of these characteristics will be important with respect to the design aspects.

**(i) Accelerometer Sensitivity**: An accelerometer's sensitivity is a function of the required magnitude of acceleration to be sensed and the method of sensing. The inverse of this sensitivity can be described by the "k/m ratio", *where* k is the stiffness of the spring and m is the mass of the proof mass.The sensitivity can be expressed in terms of capacitive sensitivity and mechanical sensitivity.

**(ii)Accelerometer Response Time:** The response time of the device is dictated primarily by the natural frequency of the proof mass. For a simple spring mass second order system (assuming critical damping), the response time can be estimated by:

$$t_{response} = \frac{4}{\xi\omega_n}$$

*where* '$\zeta$' is the damping coefficient which is given by $\zeta$=1/2Q (Q is Quality Factor).

**(iii) Cross Sensitivity:** In single axis accelerometers, it is crucial that the main axis sensitivity be at least two orders of magnitude smaller than any other axis. Otherwise, the desired output signal from the accelerometer will include unwanted cross-axis behavior.

**(iv) Minimum detectable acceleration:**The minimum detectable acceleration is determined by the total noise referred back to the accelerometer input.Hence let the applied acceleration be a constant. Then the steady-state net stretch or compression of the spring is directly proportional to the applied acceleration. Suppose that the minimum measurable spring deflection is $x_{min}$, then the minimum detectable acceleration of the accelerometer is given by

$$a_{\min} = x_{\min}\omega_n^2.$$

**(v)Bandwidth:** Let the applied acceleration be a sinusoidal with circular frequency i.e. $a = a_0 \cos(\omega t)$. The steady-state deflection of the spring is of the form $x = x_0 \cos(\omega t + \phi)$. The deflection magnitude $x_0$ is related to the magnitude of the applied acceleration $a_0$ by

$$x_0(\omega) = \frac{a_0}{\omega_n^2} \cdot \frac{1}{\sqrt{[(\omega/\omega_n)^2 - 1]^2 + 4\zeta^2(\omega/\omega_n)^2}}$$

As indicated by the notation, $x_0$ depends on the driving frequency. In particular, $x_0$ becomes diminishingly small when $\omega_n$ is sufficiently large, and the accelerometer will cease to be useful for accelerations at such a frequency. In practice, the bandwidth within which the accelerometer is useful is given by the cut-off frequency $\omega_c$. This frequency is defined by the equation

$$x_0(\omega_c)/x_0(0) = 1/\sqrt{2},$$

and is given by,

$$\omega_c = \gamma\omega_n$$

*where*

$$\gamma = \sqrt{1 - 2\zeta^2 + \sqrt{(1-2\zeta^2)^2 + 1}}$$

### 2.3.3. Accelerometer Related Errors

**(i) Non Linearity**: This is very common problem that exits when the output fails to linearly vary with the input. There can be various reasons for the origin of this error. This includes irregularities with the fabrication process, imperfections with the material or temperature variations.

**(ii) Hysteresis**: This is related to the tendency of the accelerometer to remain in its perturbed state even after the source of perturbation is removed. This is similar to the concept of inertia where the mass of the accelerometer may continue to oscillate even after the external acceleration is removed and thus causes an instability in the system.

(iii) **Cross Coupling:** Accelerometers, usually operating in open loop tend to have unwanted oscillations or vibrations due to the presence of off axis oscillations of the proof mass. This can be eliminated to a great extent by using a force feedback system as in the case of closed loop accelerometers.

**(iv) Noise:** The device sensitivity is limited due to small signal and large noise coming from the electronic circuits. The noise affecting an accelerometer's signal typically increases with the sensor's bandwidth. For an inertial navigation system to function properly, it's noise floor must be less than the necessary sensing resolution. The various types of noises present in accelerometers and a method to increase the signal to noise ration has been explained in the fourth chapter.

## 2.4. Design Challenges for MEMS Accelerometers

The most common MEMS accelerometer design parameters are resolution,sensitivity (scale-factor), bandwidth, nonlinearity, bias drift, and scale factor asymmetry. To achieve the required design parameters, the first thing the designer should do is to choose a proper process. The process limitations directly affect the performance of the sensors. Moreover, some parameters like nonlinearity, bias drift and scale factor asymmetry cannot be estimated theoretically, because they are almost totally process dependent. Hence, the choice of the process is an important design issue. After choosing the process, the performance of the accelerometer can be optimized with a proper mechanical design and with using a proper readout circuit.

# 3 DIFFERENTIAL ACCELEROMETER DESIGN

## 3.1. Device Design

The basic structure of the accelerometer is as shown in the Figure 3-1. It can be broadly classified as a differential capacitive accelerometer. The word "differential" refers to the differential actuation and sensing mechanism.

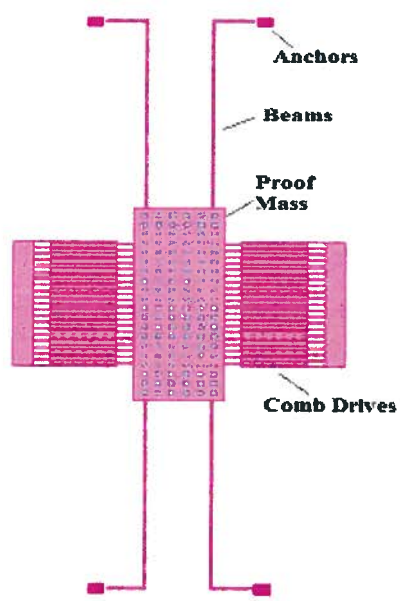


Figure 3-1. Initial Accelerometer Layout

### 3.1.1. Differential Accelerometer Topology

The design of the accelerometer consists of 3 parts - the mechanical structure, the associated electronics and the system level design. The design of the mechanical structure is usually with the help of certain simulation tools eg.CoventorWare 2006 in this case.The figure 3-2 shows the design of the accelerometer generated by the Layout Editor. It has a simple design consisting of a seismic mass at the centre with two sets of actuating and sensing fingers on its side.

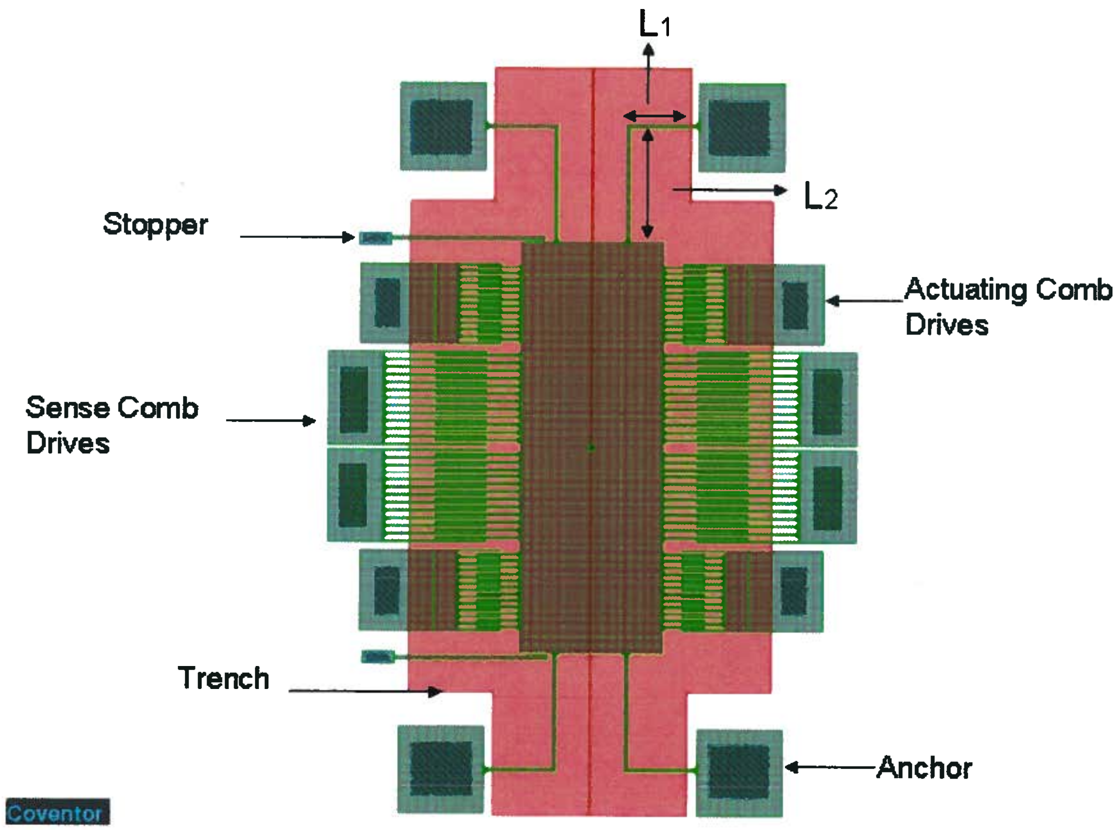


Figure 3-2. Differential Accelerometer Layout Created in CoventorWare

The dimensions of the accelerometer are given in Table 3-1.

Table 3-1. Main Parameters of the Accelerometer

| Fixed Parameter | Numerical Value |
|---|---|
| Length and width of the mass | 750μm x 250 μm |
| Length of the beam ($L_2$) | 215 μm |
| Length of the beam ($L_1$) | 125 μm |
| Width of the Beam | 5 μm |
| Thickness of the Beam | 12 μm |
| Actuation finger length | 75 μm |
| Sensing Finger Length | 180 μm |
| Initial Gap distance | 3.5 μm |
| Total number of fingers | 2*24 |

The main parts of the designed mechanical structure are as follows:

(i) **Proof Mass:** The movable mass is usually given by the total mass of the central movable frame and that of the movable fingers. But the technology design rules and the area constraints limit the total size of the structure and a compromise must be reach in dividing the given area into comb fingers and movable frame. The trench in the case of the SOI technology has the important role of releasing the movable portion of the structure. Figure 3-3 shows a zoomed in section of the different parts of the fabricated structure.

Depending on the mass distribution system, the value for m might be slightly different than the total movable mass. In this case the mass of the accelerometer is found to be **147.375μg**.

(

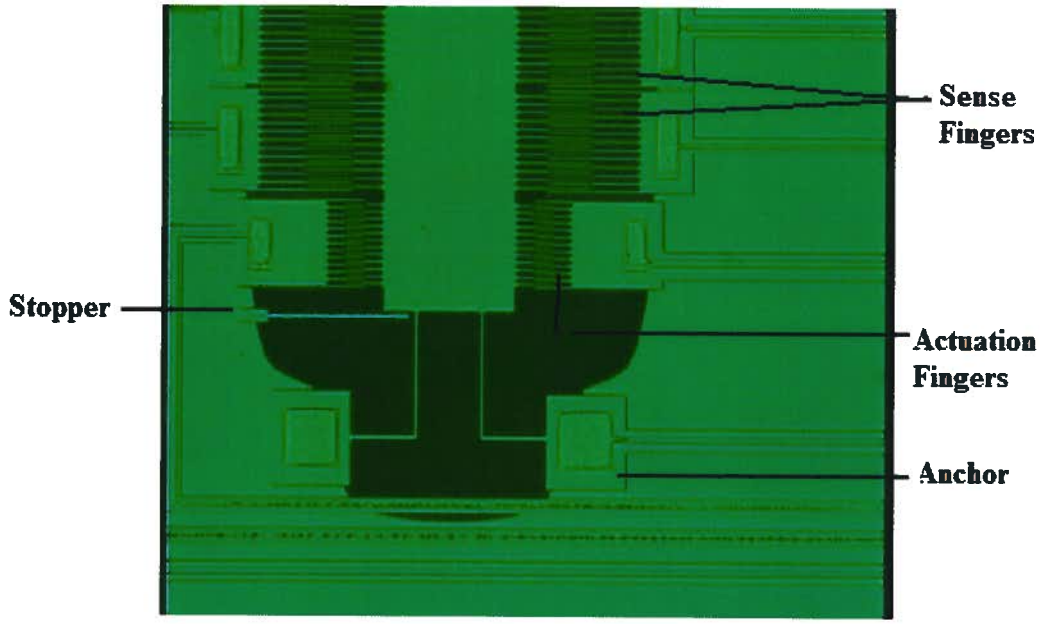


Figure 3-3. Picture of the fabricated Accelerometer

(ii) **<u>Comb Drives:</u>**

a.Actuation Fingers -

The actuation system also consists of the actuator and the associated electronics. But compared to the sense fingers, these are fewer in number and smaller. Their main function is providing an actuation which helps the proof mass to move. To provide a balance in the actuation we have 2 sets of the actuation fingers.The actuation fingers are laterally placed with a gap of 3.5 μm.The actuation set of capacitors is composed of 20 parallel plates have length $l_c$ =75μm and $d_0$ =3.5 μm. Neglecting the fringe fields, the total zero-displacement capacitance is

$$C_{a0} = N\varepsilon_0\varepsilon_r\frac{l_c w_c}{d_0} = 37.945 \times 10^{-15}F$$

b. Sense Fingers-

The sensing system consists of the sense fingers and the associated electronics. This comprises of a set of differential capacitor system wherein the displacement of the movable frame modifies the relative distance of the movable finger plates from the fixed one (anchored to the substrate).This change in capacitive vibration is sensed by the electronic read out circuit which thereby helps in measuring the input mechanical excitation. Hence the sense fingers are larger than the actuation fingers.The sense fingers are arranged on the transverse arrangement with the respective separation between the fingers and the plate as 3.5mm and 4.5mm.

Similarly we calculate the sense capacitance as,

$$C_{s0} = 109.28 \times 10^{-15}F$$

Figure 3-4 shows the normalized capacitance change with time is plotted.The figure shows a comparison with the numerical data and simulated data obtained from Matlab. The figure shows an agreement to some extent between the numerically calculated value and the simulated values for a change in the step input of about 13Volts.

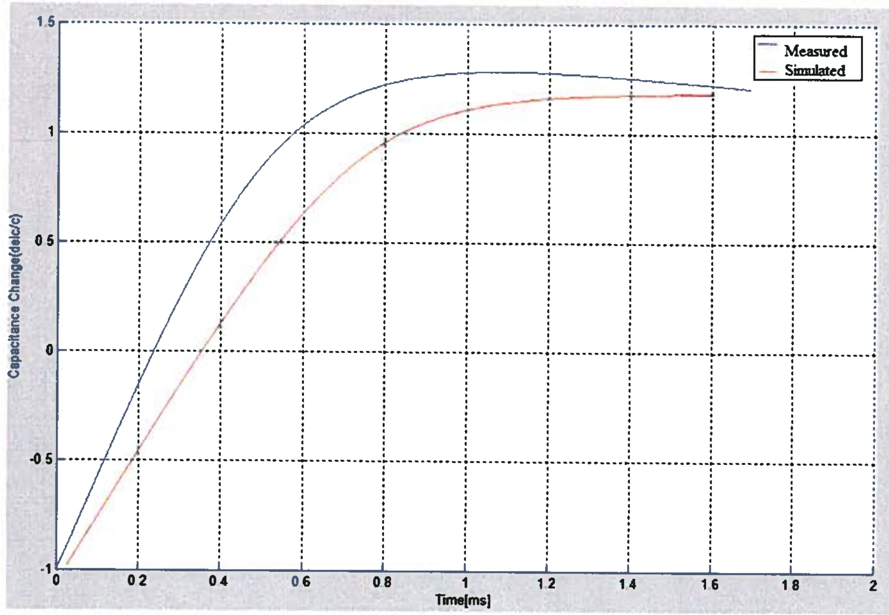


Figure 3-4. Measured and Simulated Capacitance Variation (ΔC/C) for a change in the step input of 13 V

(iii) **Support Beams:**

As explained earlier, the beams provide the stiffness required for the accelerometer. So, to achieve the desired resonance frequency, the designer usually fixes the mass to its maximum value and plays with the spring constants.There are various beam designs which are used depending on the application and the requirement. The most commonly used ones are cantilever beam, J beam (Box type) and folded structure (crab legged).To decide on the type of beam to be used, simulations were done to examine the stiffness obtanined.Using a simple schematic structure, Finite Element Modelling of a few of them was generated as follows. The schematic consisted of a simple Beam with anchor and a source (PWL).

From the simulations shown in Figure 3-5, the stiffness of the cantilever beam was found to be around 20 N/m with FEM analysis and about 18.25 N/m with Saber simulations.

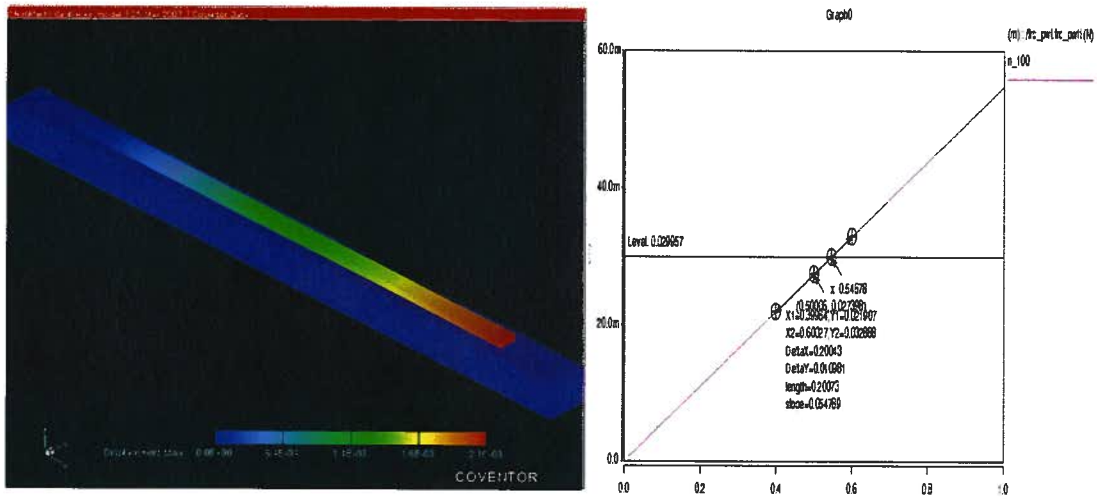


(a) (b)

Figure 3-5. Simulation Results of a Cantilever Beam (a) FEM Analysis (b) Force Vs. Displacement Curve

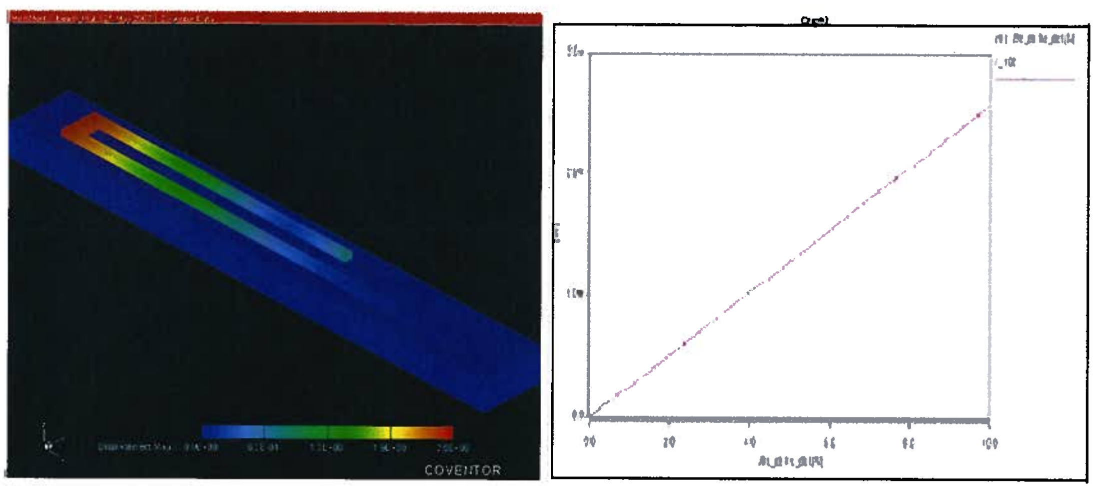


Figure 3-6. Simulation Results on a J Beam (a) FEM Simulations (b) Force Vs. Displacement Saber Simulation

In a similar way the stiffness of J type beam are simulated was found to be around 32.75 N/m with FEM analysis and about 44.5 N/m with Saber simulations (Figure 3-6).Since the stiffness matched the required range, a design was made using J type beam as shown in figure 3-7.But as we started carrying on simulations on the structure we found that the design was complex and it was difficult to match the constraints imposed by the SOI technology.Also the FEM simulation of the structure showed a high stiffness of the beam that led to a possibility of them breaking under large stresses.

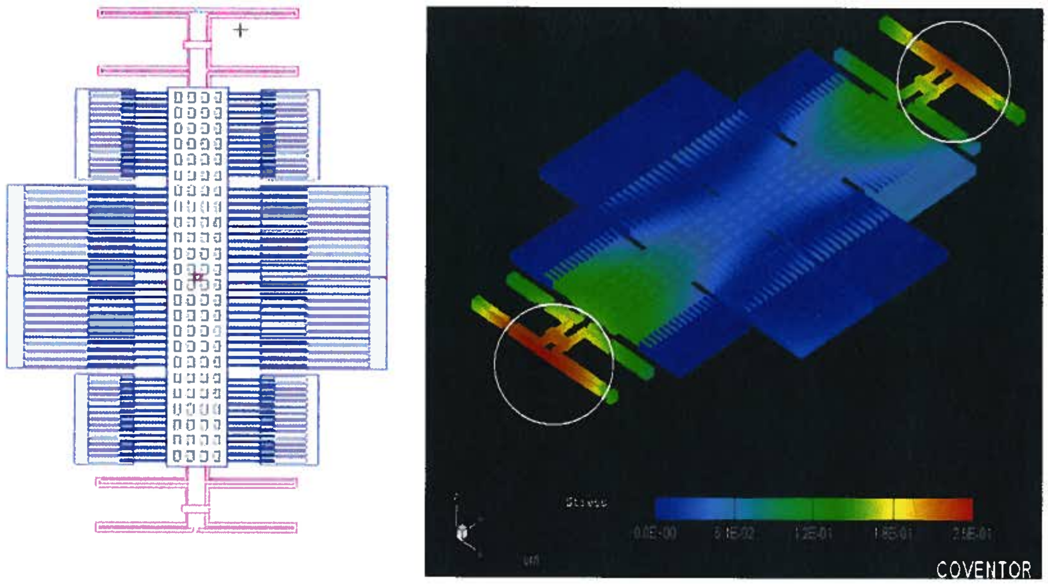


(a) (b)

Figure 3-7. (a) Complex Structure of accelerometer design having J type beam

(b) Finite Element Modelling of the structure showing the stress distribution

The reasons for using folded springs in this study are to achieve a low resonance frequency, hence a higher sensitivity, and also to decrease the total stress under an external shock. In some designs double-folded springs are used to realize even lower resonance frequencies and lower stress values, while some accelerometers have conventional folded springs to achieve higher resonance frequencies for wide bandwidth applications. Though the stiffness is very high in this case, due to the other difficulties imposed by the fabrication technology (SOI), in this case the simplest beam, crab legged beam is used; one of end which is anchored and the other end is connected to the proof mass.

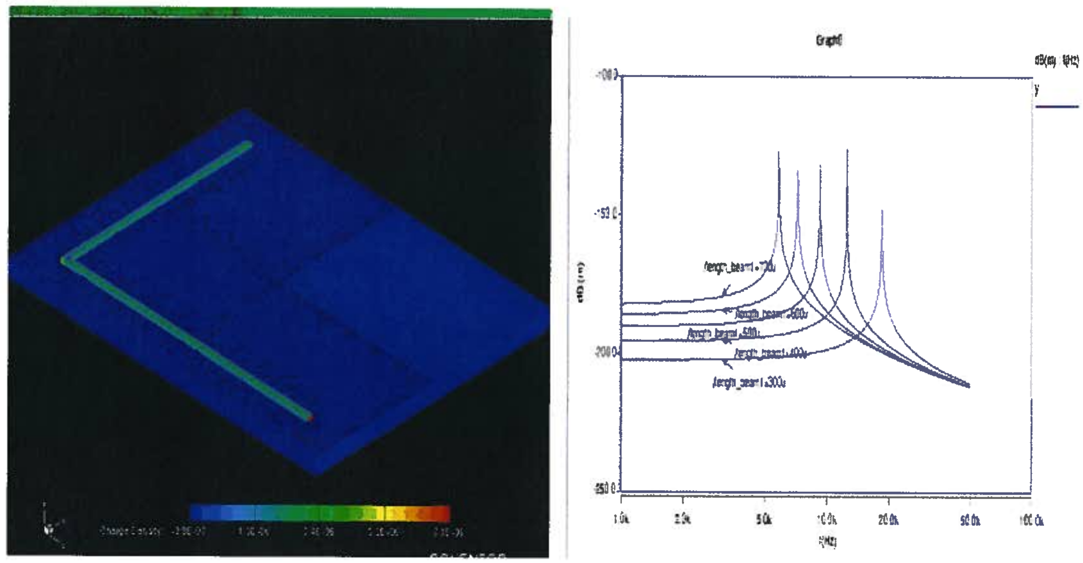

Figure 3-8. Simulation Results on a L Beam (a) FEM Simulations (b) Resonant Frequency Variation with the length

To determine the dimensions of the L beam, a graph is plotted with different lengths and widths which is shown in figure 3-8.

From the figure 3-9, we can conclude that the stiffness constant is linear for width of 5mm but becomes non-linear for 2mm and 10mm.

To determine the stiffness of the beams, one needs to know the Young's modulus of silicon (E) i.e.150 GPa and know the Cross Sectional Inertia(I).Using this in the formula

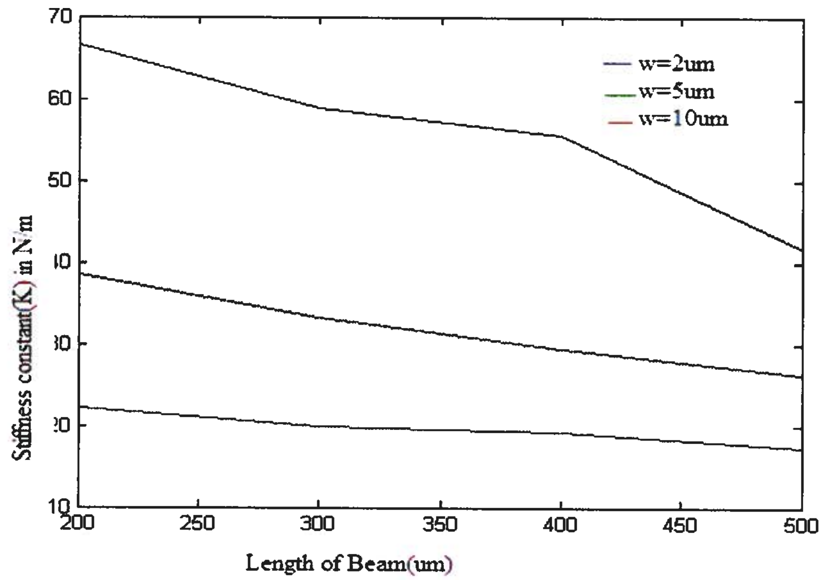


Figure 3-9. Variation of the stiffness constant for different widths of 3μm, 5μm and 10μm

for the stiffness, the stiffness in the X and Y direction is given by (refer Figure 3-10 for the dimensions).

$$K_x = \frac{Etw_x^3(l_x + 4l_y)}{l_x^3(l_x + l_y)}$$

$$K_y = \frac{Etw_y^3(l_y + 4l_x)}{l_y^3(l_x + l_y)}$$

In this case, since accelerometer should be easily able to move in the X direction, the stiffness in the Y direction is made higher i.e. $K_y$ is larger than $K_x$. From numerical calcula-

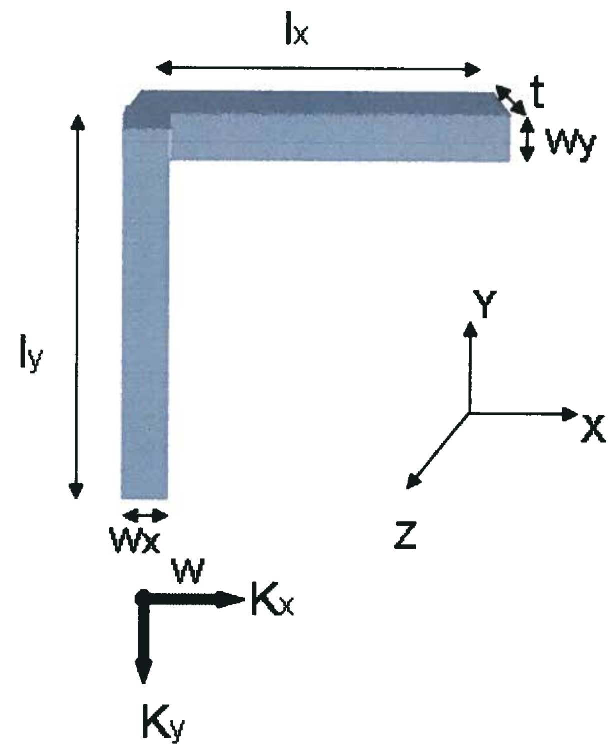


Figure 3-10. The different dimensions of the L beam

tions, we get the equivalent stiffness to be about 75.456 N/m for each of the beams. Hence, $K_{eq}$= 301.824 N/m. Also the maximum stress at the end of the beam is calculated as

$$Stress(max) = 3\frac{wx}{l^2}E = 4.008 N/\mathrm{m}^2$$

(iv) **Anchors:**

The anchors serve to fix the movable structure to the substrate as shown in the figure. The dimensions of the anchor used are 150μm x 150μm.

## (v) **Stoppers:**

Figure 3-11 shows the SEM picture of the anchors and the stoppers. A mechanical stopper is commonly used to avoid the over-range travel of the movable frame, in the case of large shocks. They also protect the sticking of the movable structure on the elements anchored to the substrate and simultaneously avoid large elongations of the suspension system. As the sticking phenomena depends on the contact area, it is important to design the stopper geometry for avoiding large contact surfaces with the movable part. The stoppers also help in pull-in mode of operation of the accelerometer. The stopper designed in this accelerometer is rectangular with a teeth shaped structure and its explained in detail in the next chapter.

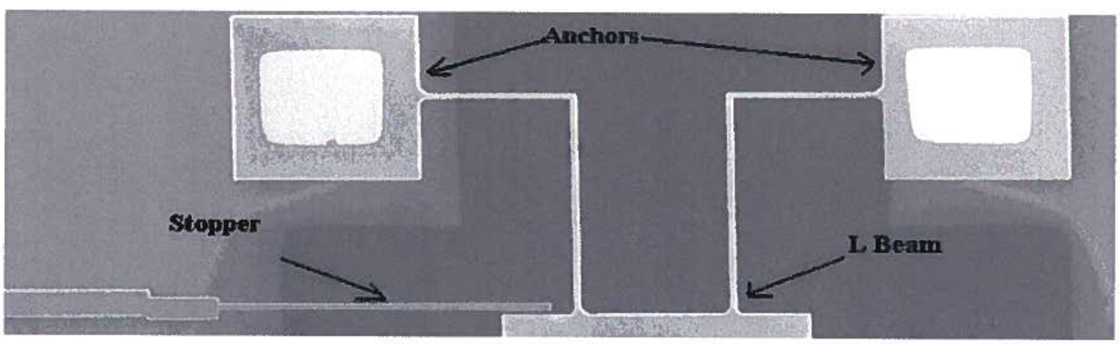


Figure 3-11. SEM picture showing the anchors and the stopper with its zigzag teeth structure

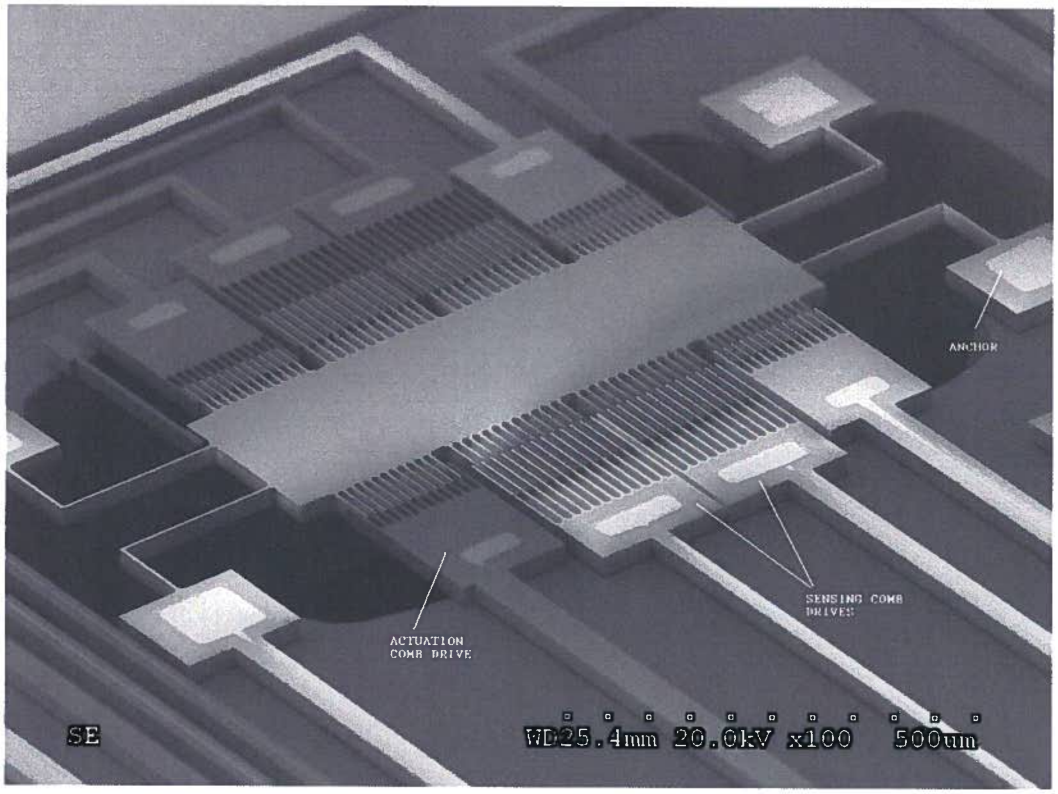


Figure 3-12. SEM Picture showing the entire structure

## 3.2. Simulation Results

The next step after the design of the mechanical structure is verification of the built model with system level simulations.Simulations were carried in Matlab as well Coventor-Ware 2005.

### 3.2.1. Simulink Model

The simulink model of the accelerometer is shown in figure 3-13. The principle of construction of the model is very simple. All the different numerical parameters of the accelerometer which are known from analytical calculations are directly entered as constants. The main model can be split to be consisting of 4 sub models:All the different set of equations relating to the accelerometer are plugged into the different blacks and the different parameters are plotted in the scope.

- Actuation Force - *calculates the force required to actuate the system.*
- Accelerometer ODE Solver-*solves all the equations with respect to the model and determines the displacement,velocity and acceleration.*
- Non Linearized Capacitance Calculation-*Calculates the capacitance change caused due to the displacement.*
- Capacitance to Frequency Calculation-*Determines the Resonant Frequency of the system.*

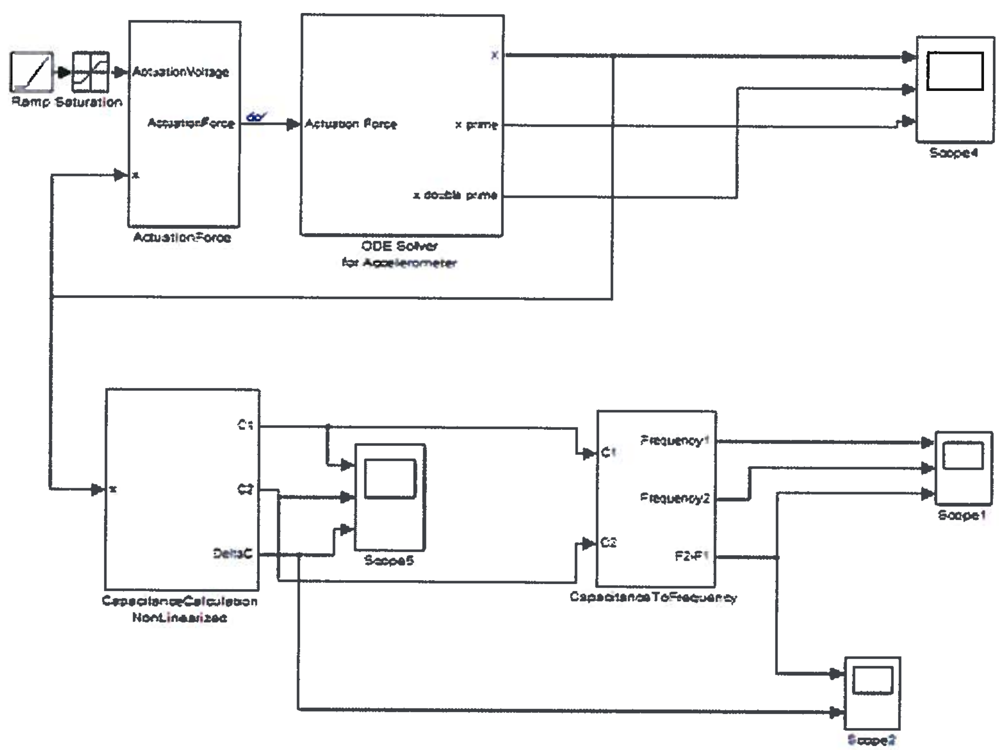


Figure 3-13. Simulink Model of the accelerometer

Figure 3-14 shows the displacement variation with respect to time. The region of interest is towards the pull-in region when displacement (x) tends to become equal to the gap ($d_0$). At the point when x=1.8μm (x=1/3$d_0$), x starts increasing slowly. When x becomes greater than $d_0$, the displacement curve suddenly shoots up along with time.

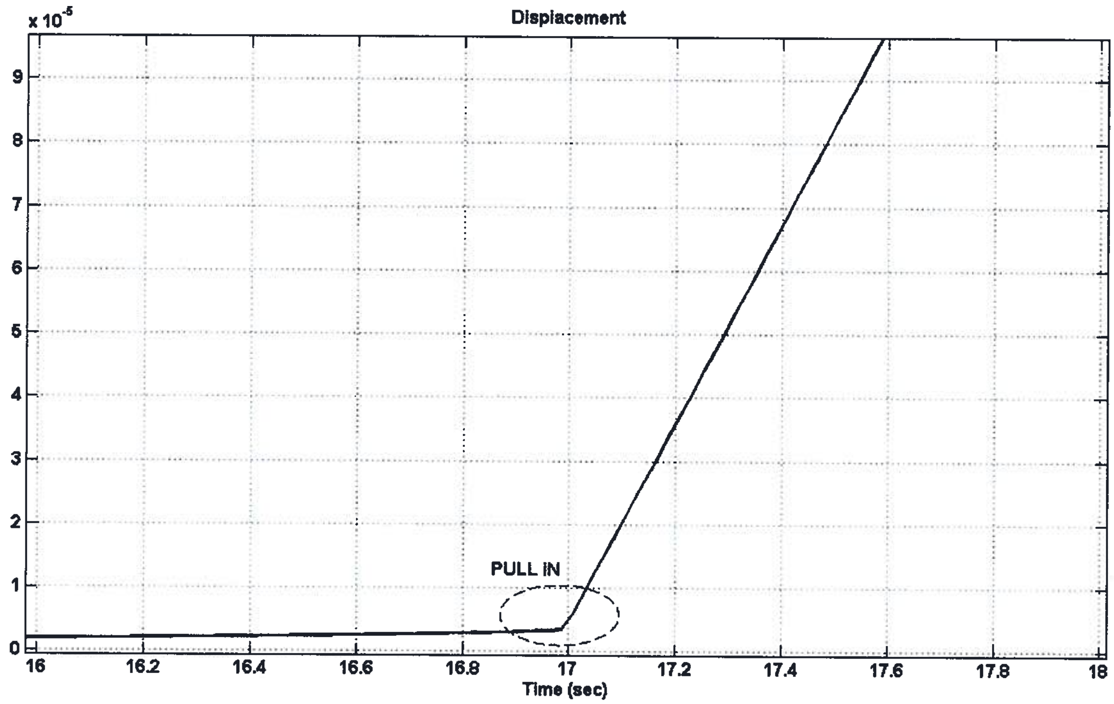


Figure 3-14. Displacement (μm) Vs. time(s)

Figure 3-15 shows the variation of capacitances $C_1$, $C_2$ and ΔC with time. It has been observed that $C_1$ and ΔC follow a very close pattern. This is because both have $d_0$-x in their denominator where as $C_2$ has $d_0$+x. Also its seen that the variation of capacitance is linear in the beginning and then suddenly starts getting unstable as $d_0$=x. Also at this point as the denominator tends to become almost 0, i.e when the electrodes touch each other, there is a sharp increase in capacitance. When x starts increasing beyond $d_0$ (which is physically not feasible as the electrodes cannot displace each other), the capacitance starts becoming negative.

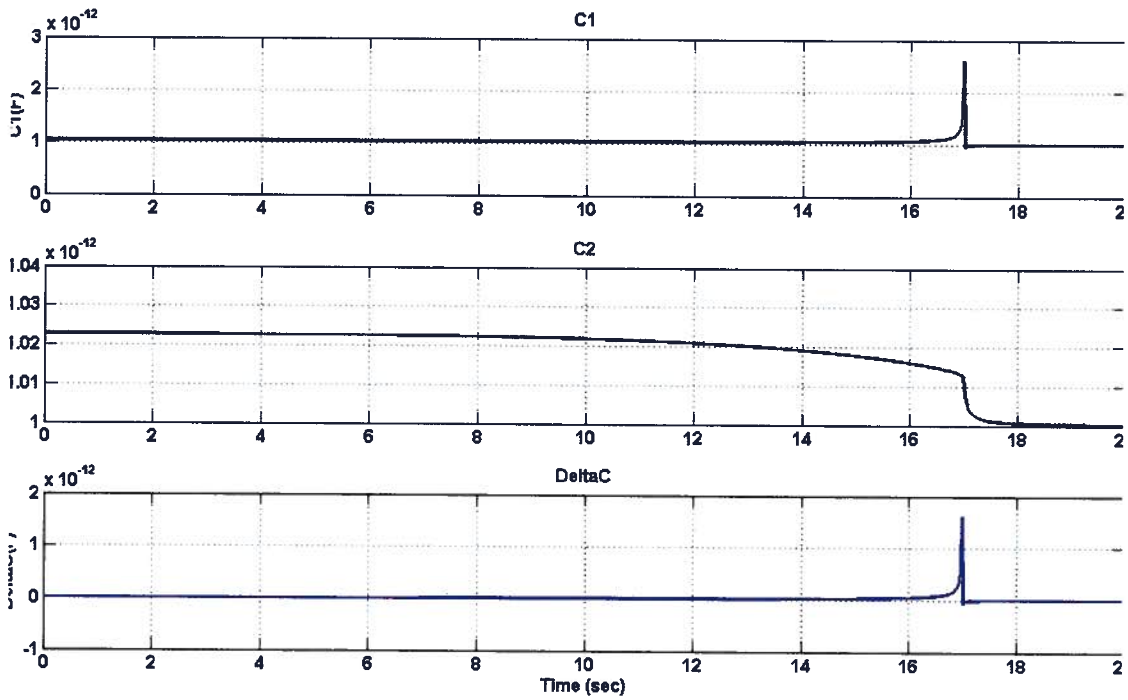


Figure 3-15. Capacitance Variation with time

The difference in capacitance has been zoomed in Figure 3-16.

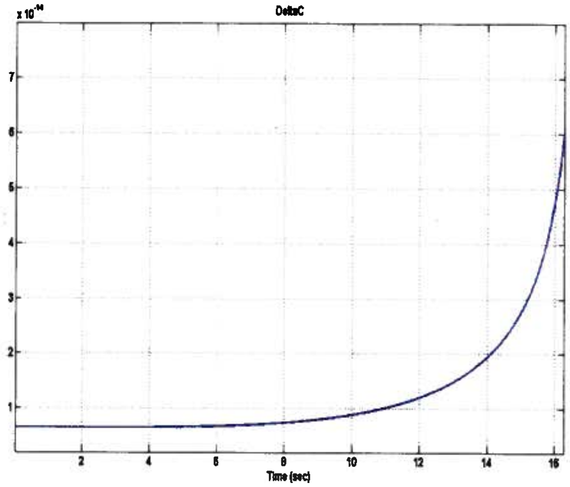


(a)

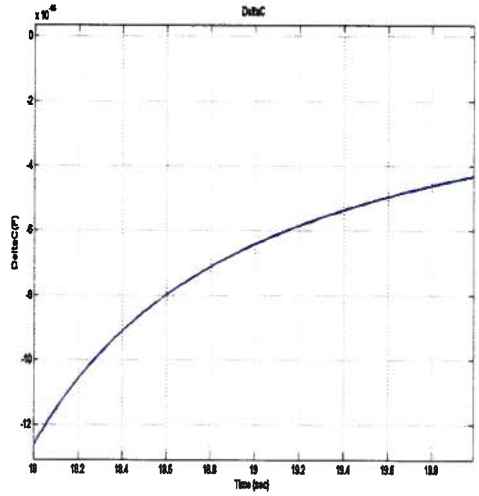


c)

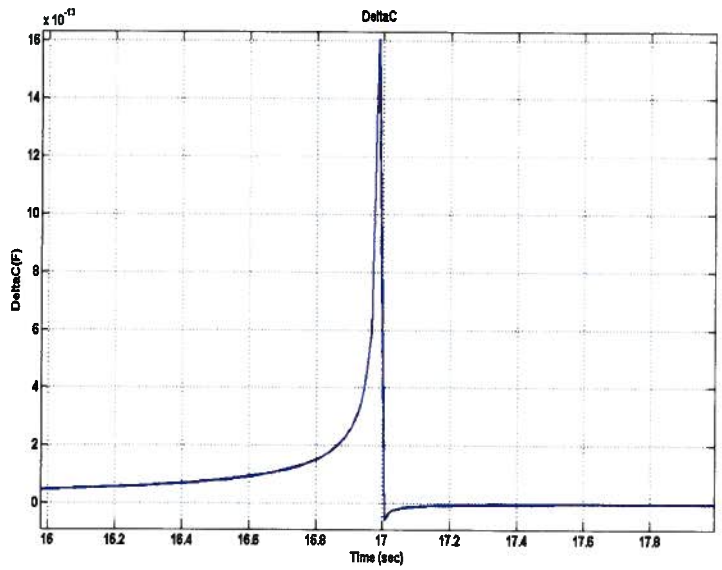


(b)

Figure 3-16. Zoomed ΔC graph (a) when $x<d_0$ (b) when $x=d_0$ (c) when $x>d_0$

Figure 3-17 shows the velocity changes with time. It follows a similar pattern as the displacement i.e, its linear for a while and then when pull-in happens it suddenly increases sharply and then becomes almost a constant.

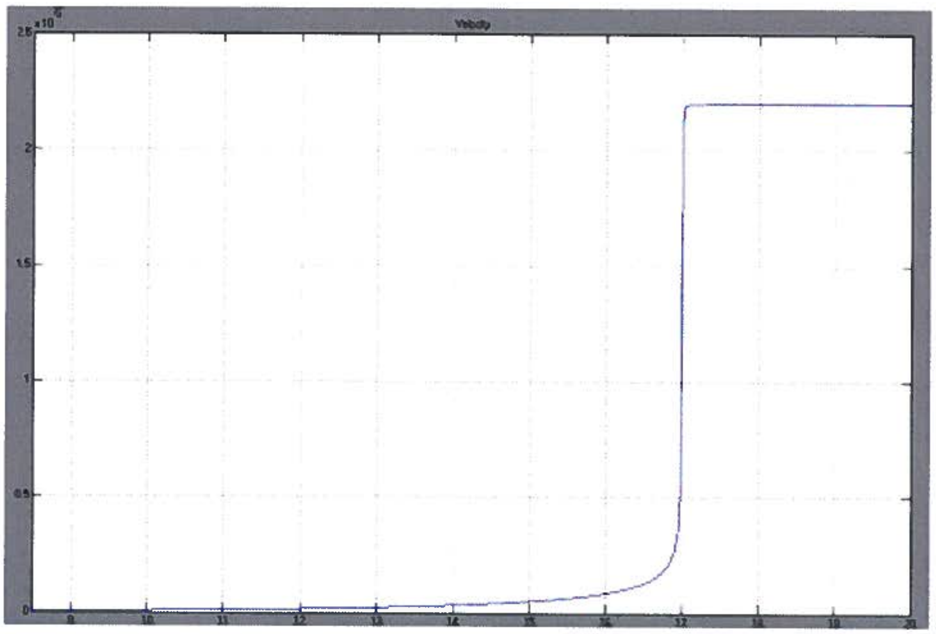


Figure 3-17. Velocity Change with respect to time (dx/dt)

Figure 3-18 shows the acceleration variation of the seismic mass with time.It has a peak during pull-in and then starts decreasing after the phenomenon has occurred. This represents the internal acceleration of the accelerometer which corresponds to the external applied acceleration of an open loop system.

### 3.2.2. Coventoware 2006 Simulation

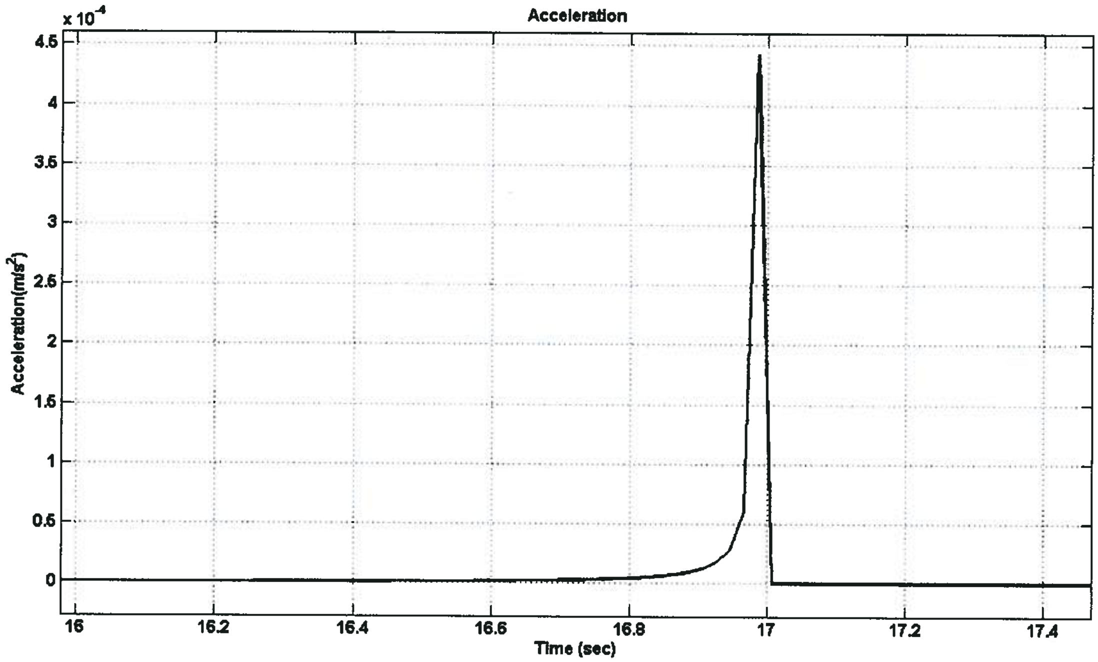


Figure 3-18. Measurement of the output acceleration

For this accelerometer model all the system level simulations have been performed using one of the most powerful existing software, CoventorWare© 2006. CoventorWare provides a comprehensive, integrated suite of tools for MEMS that enables rapid exploration of process and design options. The Architect suite allows system-level designers to simulate and rapidly evaluate multiple design configurations using a top-down, system-level approach. When the overall model has been sufficiently designed and analyzed, the layout can be extracted and viewed in the Designer's 2-D Layout Editor. This layout can then be combined with a process description to create a 3-D model, then meshed and simulated using the analyzer's FEM solvers. The Integrator suite allows users to create custom macro models from FEM meshes that can then be input to an Architect system model.

### 3.2.2.1. Saber Architect

The first step in simulating using CoventorWare will be to introduce the schematic in Saber as shown in figure 3-19.

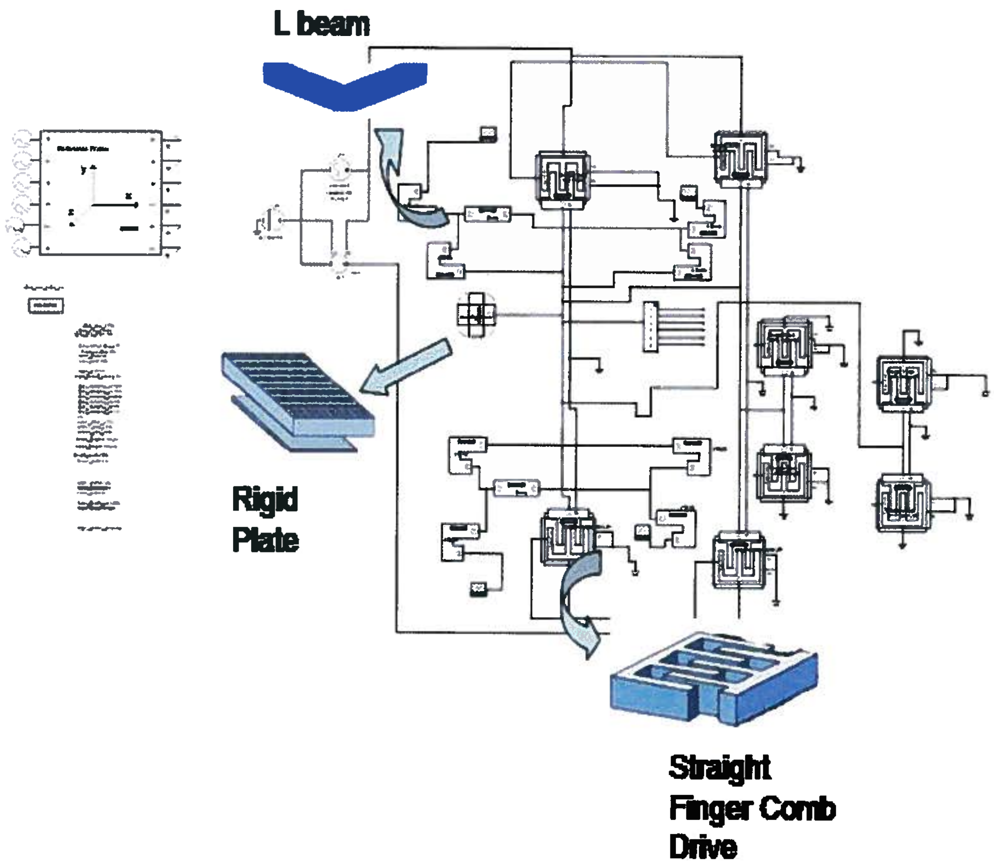


Figure 3-19. Saber Schematic showing the design for the differential accelerometer

The schematic is the backbone of the model.It contains the different parameters of the accelerometer model placed and connected by wires.Each block has the parameters fed into it.

### 3.2.2.2. DC Operating point

DC analysis is two-step verification for the completeness of the schematic. First, before performing the DC Operating Point Analysis, Saber generates a netlist. If some required attributes are missing or if some design variables have no numerical value, Saber will fail to read this netlist. Second, DC analysis results give a fast overview of attribute correctness: X, Y, and Z coordinate values. One of the first analysis done is the DC operating point analysis in order to determine the stability of the designed system. Figure 3-20 shows a snapshot of the output of the DC operating point simulation done in Coventorware.

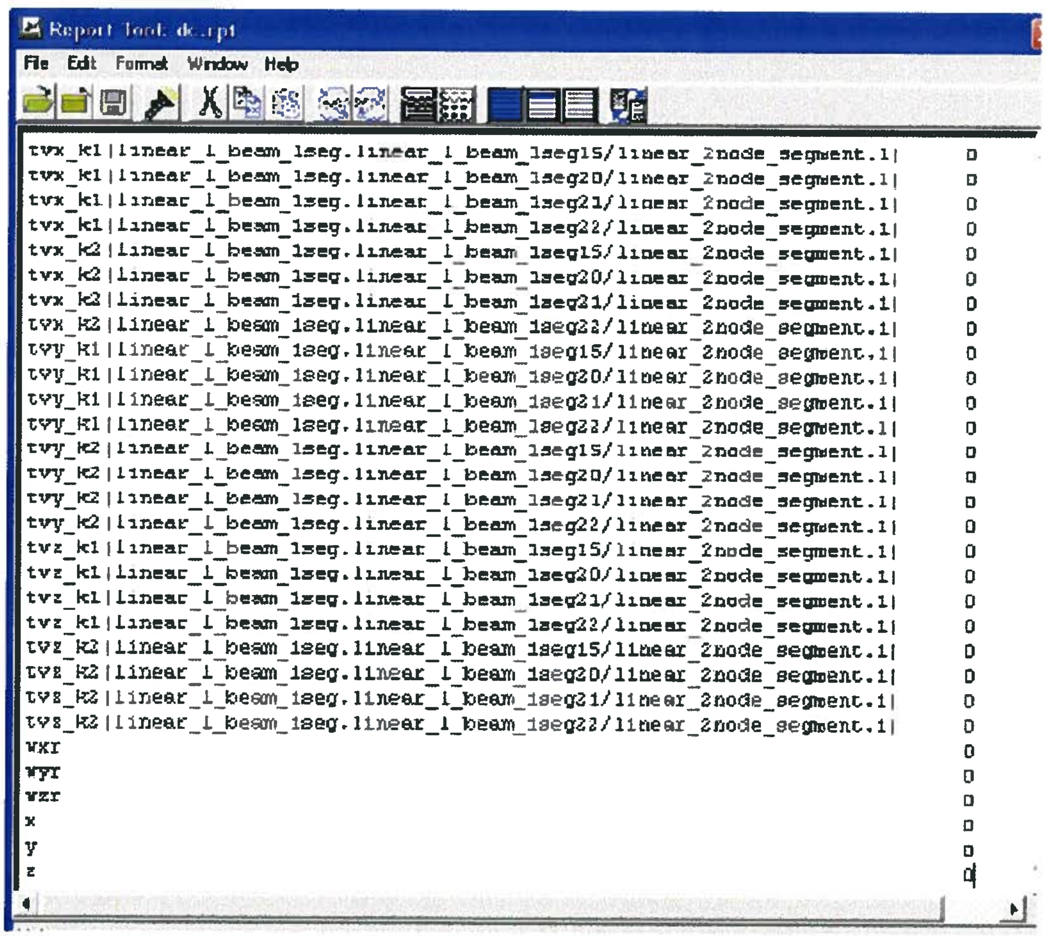


Figure 3-20. Snapshot of the showing a stable DC Operating point of the system

#### 3.2.2.3. DC Transfer Analysis

In this analysis the DC voltage is applied to the system and the system is actuated to the system is set to vibration at a frequency. The displacement is studied for the force applied. From the inverse of the slope of the graph which gives the stiffness. The figure 3-21 shows the simulation of the force applied to the displacement of the beams.

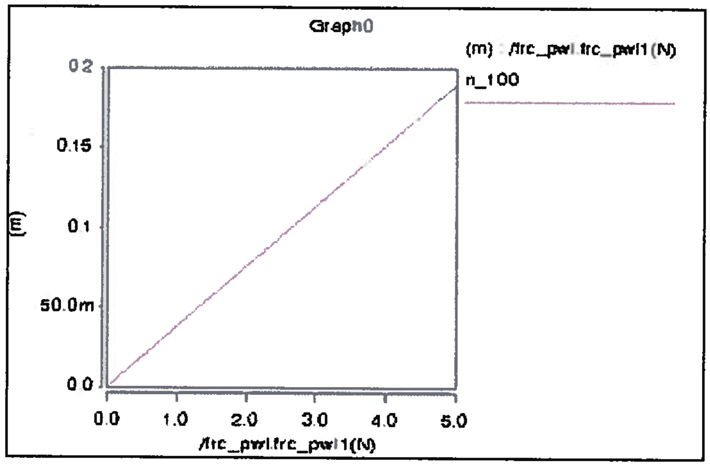


Figure 3-21. Force Vs. Displacement to determine the stiffness of the beam

As per definition

$$k = \frac{1}{\text{slope of the curve}} = \frac{1}{0.0111607} = 89.54 N/\text{m}$$

and hence the total stiffness is found to be 89.54 x 4 =358.16 N/m which is close to the numerically calculated value of 301.824 N/m.

### 3.2.2.4. Pull-in Analysis

Using Coventoware the electromechanical response of the beam. The basis of the simulation was subjecting the model of the accelerometer created to be subjected to an increased growth of electrostatic force to a point until the critical pull in voltage is reached. At this point the growth of the electrostatic force becomes dominant over the restoring force and the comb drives snap quickly i.e pulls in. Figure 3-22 shows the simulation of the pull-in analysis. The voltage applied was slowly increased till the calculated value of pull-in voltage to cross verify the numerical and the simulated value of the pull-in voltage.

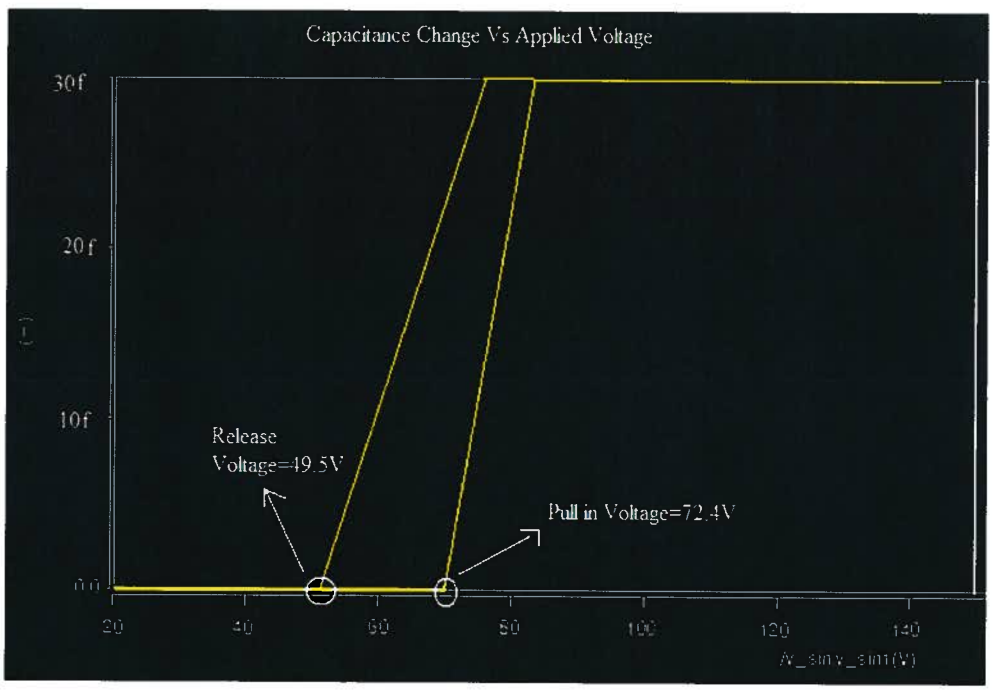


Figure 3-22. Capacitance Change Vs. Applied Voltage

This phenomenon is explained more in detail in the next chapter.

#### 3.2.2.5. AC Analysis

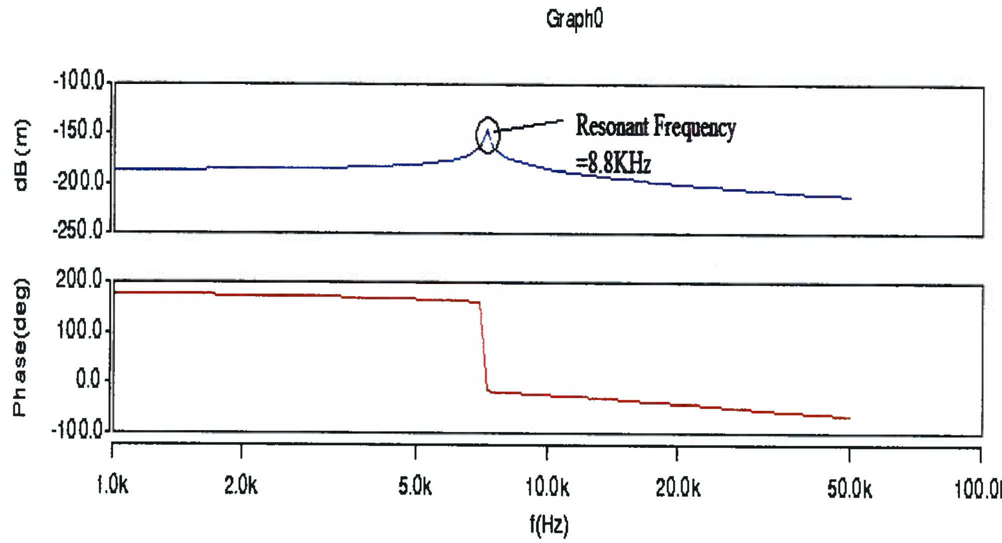


Figure 3-23. Saber simulation showing the resonant frequency (phase and magnitude)

This analysis is very important and it determines the resonant frequency of the system. From the Figure 3-23, the resonant frequency is found to be around 8.8kHz which is close to the numerical value found to be 7.192kHz.

#### 3.2.2.6. Transient Analysis

Transient Analysis refers to the time domain analysis which explains the behavior of the sensor with variation in time. This is important especially to check the cross sensitivities. In such a kind of simulation, the device is actuated and the behavior is studied for a specified time interval and the displacement readings of the proof mass was recorded. These values were plotted in excel to see the variation in displacement over the period of time. The figure 3-24 shows the displacement time characteristics.

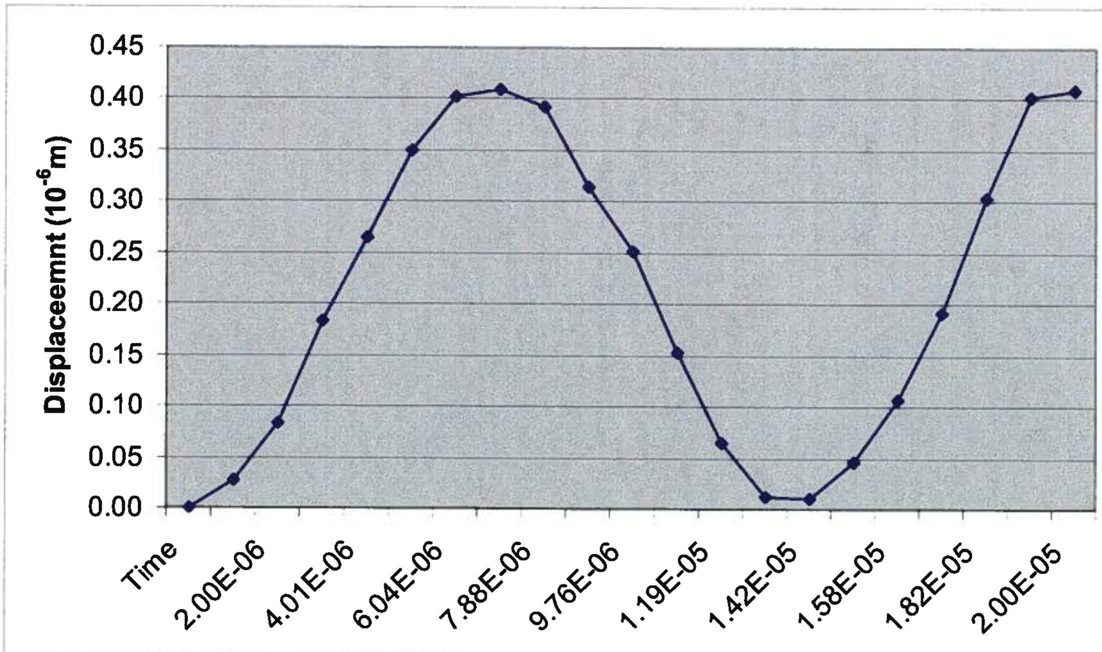


Figure 3-24. Displacement(μm) variation with respect to time

### 3.2.2.7. Sensitivity

The sensitivity of a sensor is defined by the ratio of the output voltage over input acceleration. This can be expressed as:

$$\frac{\Delta V}{a} = \frac{\Delta x}{a} \times \frac{\Delta C}{\Delta x} \times \frac{\Delta V}{\Delta C} = \frac{m}{k} \times \frac{C_s}{d} \times \frac{V}{C_s + \frac{C_p}{2}}$$

where $C_s$ refers to the sense capacitance and $C_p$ is the parasitic capacitance.

Using this formula the sensitivity of the accelerometer is calculated to be around 2.129mV/g. The figure 3-25 shows the measure of the output voltage with respect to the output acceleration i.e. is a measure of sensitivity. The equation of the straight line obtained is given by y=0.006137x+0.784. From this, we obtain the sensitivity as 6.137mV/g..

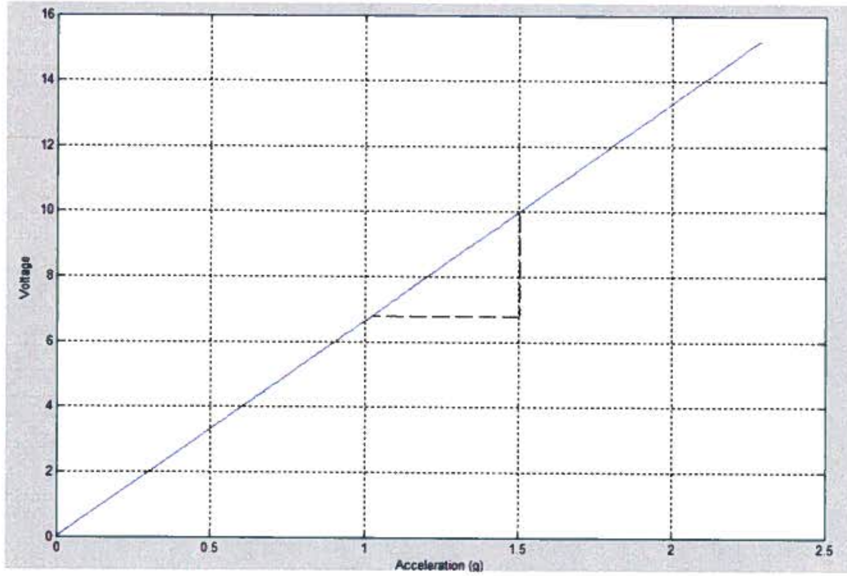


Figure 3-25. Sensitivity of the Accelerometer

### 3.2.2.8. Generation of the 2D Layout and Solid Model with Mesh

Using the settings from the Analyzer module in CoventorWare, a solid model of the structure was created. This was then meshed using Extruded bricks Mesh type.This is shown in figure 3-26.

After meshing the next step is perform Finite Element Modelling to verify the functionality of the system.The displacement of the fingers was closely observed and was found to vary between 0.27μm and 2.7μm.

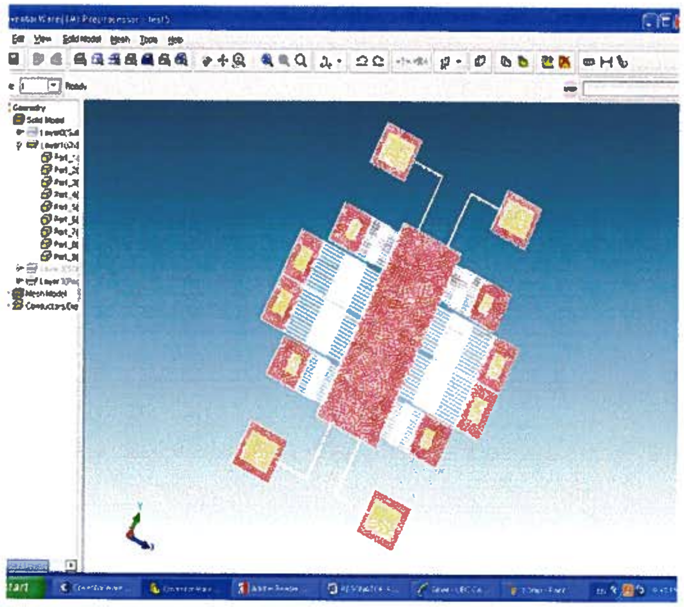

Figure 3-26. Meshed Solid Model of the Accelerometer

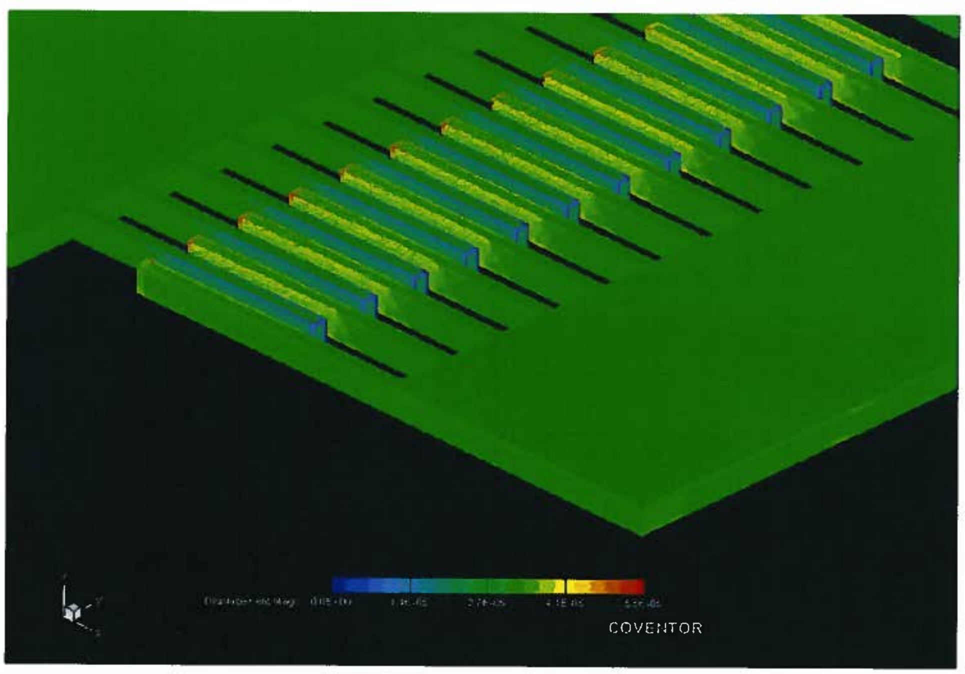


Figure 3-27. A zoomed in image showing the displacement of the fingers (Finite Element Modelling Using Coventorware)

## 3.3. Device Fabrication

SOIMUMPs process is a commercial MUMPs (Multi-User MEMS Processes) provided by MEMPSCAP. The following Figure 3-28 shows the overview of the SOIMUMPs process. The process uses an SOI (Silicon on Insulator) wafer and patterns the top silicon layer for the structural layer. The SOI wafers consist of a 10μm Silicon layer, a 1μm Oxide layer, and a 400μm Substrate layer. A Bottom Side Oxide layer is also initially present on the wafers. The process starts with the phosphorus doping of top silicon layer. This doping is to arrange the resistivity values of the silicon layer. A phospho silicate glass layer (PSG) is deposited, and the wafers are annealed at 1050°C for 1 hour in Argon to drive the Phosphorous dopant into the top surface of the Silicon layer. After this step, Cr/Au metal layer is patterned. The wafers are coated with negative photoresist and lithographically patterned by exposing the photoresist with light through the first level mask (PAD METAL), and then developing it. A metal stack consisting of 20 nm chrome and 500 nm gold is deposited over the photoresist pattern by E-beam evaporation. The photoresist is then dissolved to leave behind metal in the opened areas. A successful lift-off step patterns the metal layer. After first metallization, structural layer is patterned. To achieve this, masking photoresist is coated, exposed and developed according to structural mask. After lithography, the structural silicon is etched with DRIE up to the oxide layer. After this point, the front part of the wafer is coated with a protective layer and a masking photoresist layer is patterned on to the backside of the layer. The bulk silicon part of the wafer is etched all the way with DRIE up to the oxide layer. This etching defines the suspended regions of the sensors. After this step the oxide layer and the protective layer is etched. From this point on, the substrate connection can be achieved and the structures are suspended. A shadow mask technique is used to pattern second metallization which provides substrate connection. The process ends after the shadow mask is removed.

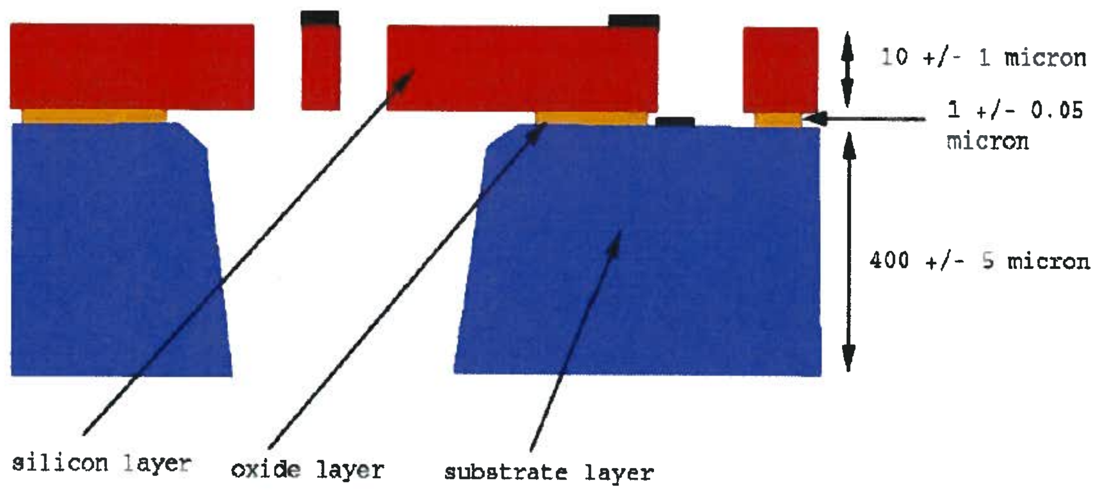


Figure 3-28. SOI MUMPS Cross Section

The main advantage of this process is using single crystal silicon as its structural layer. Single crystal silicon shows great mechanical and electrical properties and is highly preferred is MEMS devices. Moreover, DRIE patterning on the front size provide 5 aspect ratio capacitive walls for vertical comb structures. Combining this moderately high aspect ratio with 10 μm structural height, reasonably high capacitances can be achieved with this process. Due to these advantages, SOIMUMPs process was chosen as the fabrication processes for fabricating the sensors. The dimension of each layer has been defined together with its tolerances. The most crucial reason why the SOI MUMPS technology was chosen instead of the other MUMPS technologies is because this technology provides highly planarized surfaces. This is essential for the creation of mirrors because mirrors need to be flat. The mirrors are then formed by depositing metal on the flat surface. Several ensuing advantages come from the choice of using SOI MUMPS, namely increased reliability in fabrication as well as lower cost. These advantages can be attributed to the fact that because less number of layers are needed, less fabrication steps are needed. SOI MUMPS has only one structural layer whereas other technologies like Poly MUMPS has three structural poly silicon layers. The disadvantage of using this technology is that there is only one structural layer, namely the silicon layer. This excludes the use of conventional hinges and joints, making the design more difficult and more restricted.

The following Figure 3-29 is the process file from CoventorWare which describes the exact details of the SOI MUMPS template.

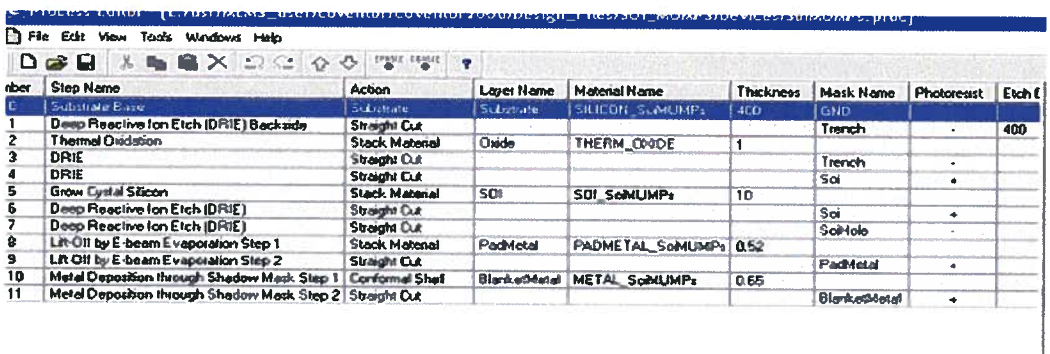

File Edit View Tools Windows Help

| ber | Step Name | Action | Layer Name | Material Name | Thickness | Mask Name | Photoresist | Etch ( |
|---|---|---|---|---|---|---|---|---|
| 0 | Substrate Base | Substrate | Substrate | SILICON_SoMUMPs | 400 | GND | | |
| 1 | Deep Reactive Ion Etch (DRIE) Backside | Straight Cut | | | | Trench | - | 400 |
| 2 | Thermal Oxidation | Stack Material | Oxide | THERM_OXIDE | 1 | | | |
| 3 | DRIE | Straight Cut | | | | Trench | - | |
| 4 | DRIE | Straight Cut | | | | Soi | + | |
| 5 | Grow Cystal Silicon | Stack Material | SOI | SOI_SoMUMPs | 10 | | | |
| 6 | Deep Reactive Ion Etch (DRIE) | Straight Cut | | | | Soi | + | |
| 7 | Deep Reactive Ion Etch (DRIE) | Straight Cut | | | | SoiHole | - | |
| 8 | Lift-Off by E-beam Evaporation Step 1 | Stack Material | PadMetal | PADMETAL_SoMUMPs | 0.52 | | | |
| 9 | Lift Off by E-beam Evaporation Step 2 | Straight Cut | | | | PadMetal | + | |
| 10 | Metal Deposition through Shadow Mask Step 1 | Conformal Shell | BlanketMetal | METAL_SoMUMPs | 0.65 | | | |
| 11 | Metal Deposition through Shadow Mask Step 2 | Straight Cut | | | | BlanketMetal | + | |

Figure 3-29. Snapshot of the SOI process file used in CoventorWare

The surface of the fabricated structure were studied under a Olympus Confocal Laser Scanning Microscope. It could capture the surface profile to a high precision. This is clearly demonstrated from Figures 3-30 and 3-31.


Figure 3-30. A zoomed view of the surface of Fabricated Silicon

This shows a very high degree of smoothness with the SOI fabrication technology.


Figure 3-31. Surface Roughness of the Silicon in the Y direction

The figure 3-32 shows the SEM picture of fabricated SOI accelerometer.

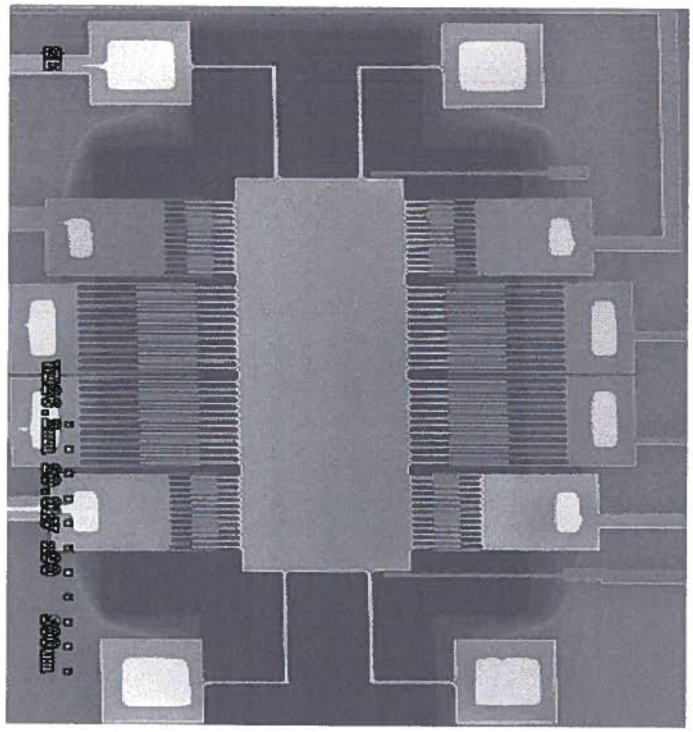

Figure 3-32. SEM picture of the fabricated SOI Differential Accelerometer

# 4 EXPERIMENTAL VERIFICATION AND DEVICE CHARACTERIZATION

Once the structure has been designed and fabricated the next step is to check if the device is working.Experimental measurements are done to verify if the simulated and the analytical values match with the experimental results.This chapter describes some of the experimental verification done.The later half of the chapter describes the pull-in analysis of the accelerometer and its different operational modes.

## 4.1. Experimental Verification

The first thing analyzed was to check if the samples were released and that was done by viewing the trench in the microscope. From the SEM pictures, the samples looked to have been released. Then the samples were put on to the probe station with the front sides looking up. Using a probe, the proof mass was pushed a little in the sensitive direction. There was a deflection is seen in the springs, which confirmed that the structure was released.The figure 4-1 shows the visible trench as seen in a microscope.

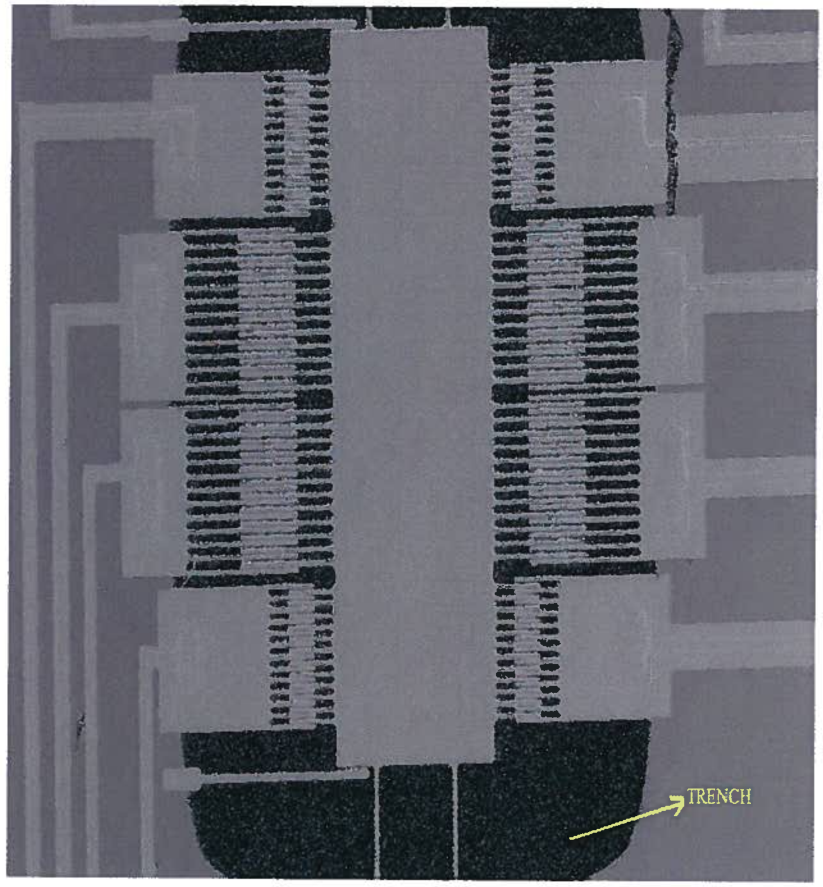


Figure 4-1. SEM Picture showing the trench and validating the release of the struture

The short circuit test was also performed using the probe station. Using two probes and connecting these probes to the multimeter, it was verified if there was any short circuit associated anywhere in the device.

The third test was the pull- in voltage test. This can also be called the DC Test. The samples that showed positive result from the previous two tests were measured for their pull in voltage. Pull- in voltage test can identify if the devices actually move and its value along with the release voltage can be used to identify the stiffness constants as. The set-up requires DC voltage source, probe station and the software (in this case a matlab program was used) to plot the Current Vs. Voltage and resistance Vs. the voltage graphs. The key point in these measurements is the calibration step. Before taking any data, the calibration should be done not to measure false values.The probes were attached to the bond pads. The DC voltages was applied to the bond pads in the sense comb drives as shown in the figure 4-2.

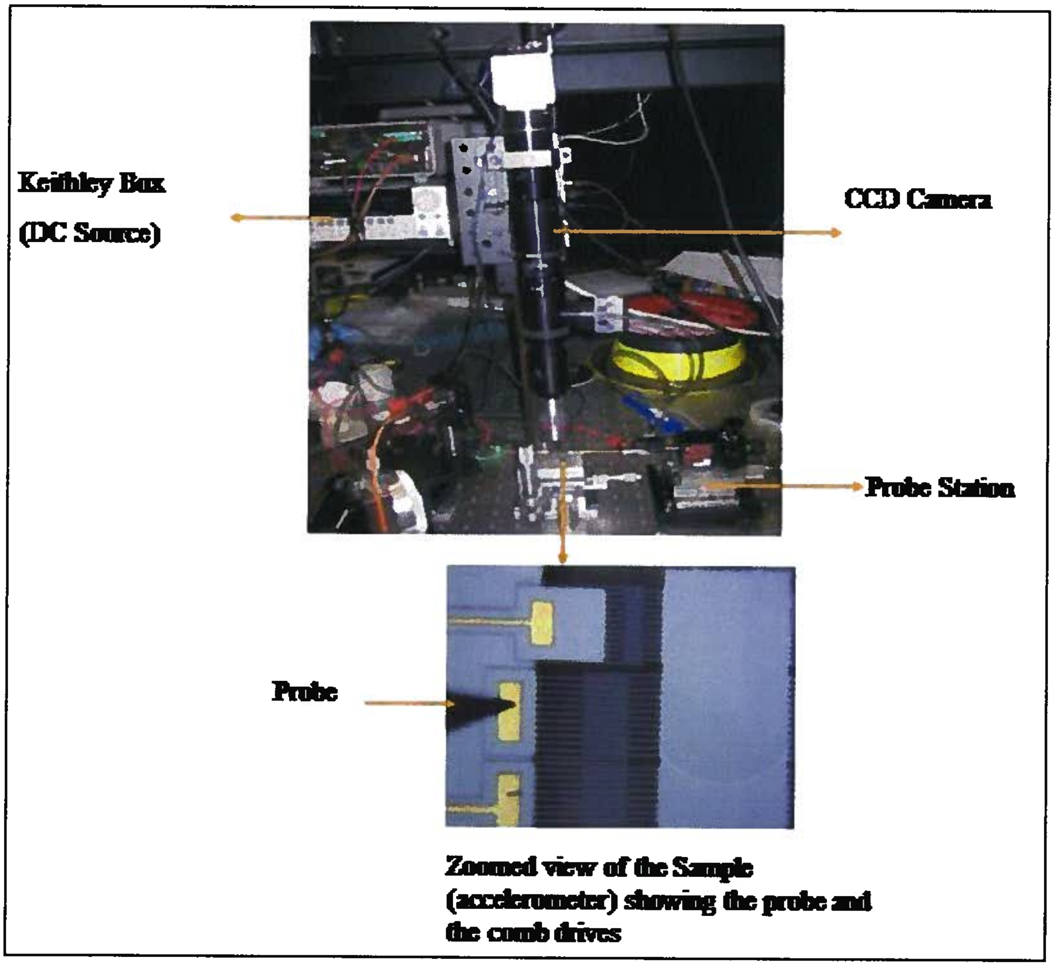


Figure 4-2. The DC Measurement set up to determine the pull-in Voltage

The voltages were slowly applied to the pad metal of the sense comb drive, limiting the current to 10μA and varying the DC voltages from 40-65 Volts. From the calculations we know that around this voltage when a short circuit occurs, the fingers get pulled in. We notice that at around 64.9V pull in occurs.

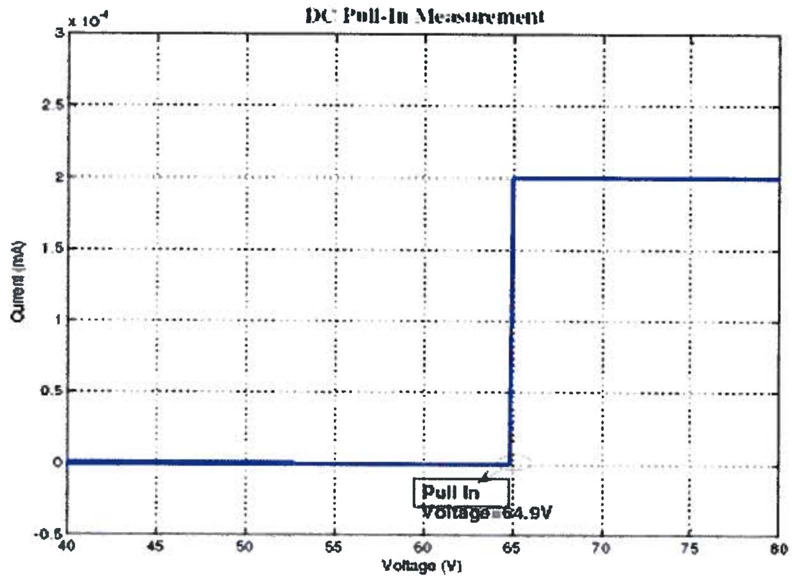


Figure 4-3. Experimental Verification of pull in voltage

Pull-in occurs when the elastic force can no longer balance with the electrostatic one. After pull-in the structure will stop at the designed stopper position where the electro-static force equals the sum of the elastic force and the reaction force of the stopper. To verify this phenomenon experimentally, a voltage is applied till the distance between the fingers reduces gradually. After the fingers are pulled in, a reverse process is followed up wherein the applied DC Voltage is slowly decreased and at one point the fingers return back to their initial rest positon.This voltage is called the release Voltage (Figure 4-4).

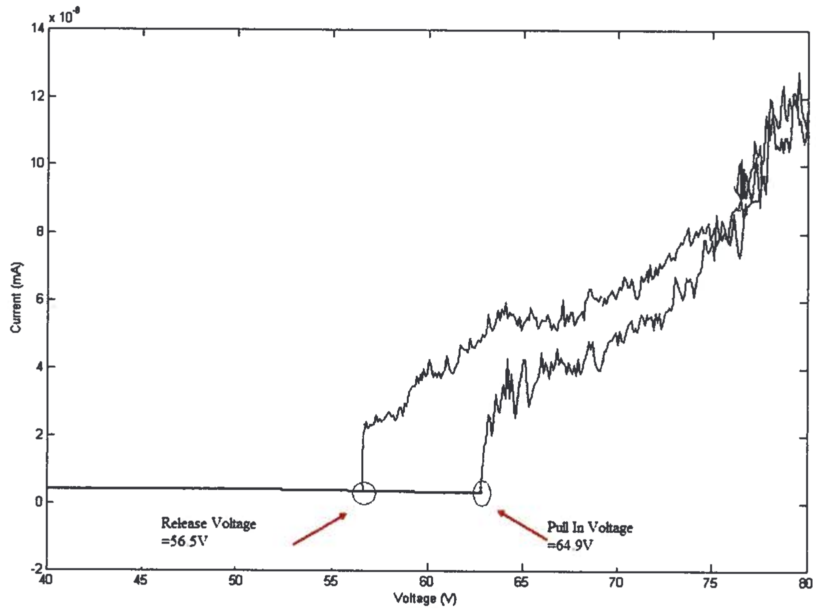


Figure 4-4. Experimental verification of the pull-in voltage and the release voltage

The last test is resonance frequency test. A schematic of the set-up of the oscillator characterization using the LDV is as shown in the Figure 4-5. Both DC bias and AC signals are applied on the accelerometer through probes and contact pads, and both continuous and pulsed signals can be used to actuate the device. The vibrations are measured by the LDV on top. Both the actuation signal and the vibration signal are monitored by an oscilloscope (Figure 4-6).

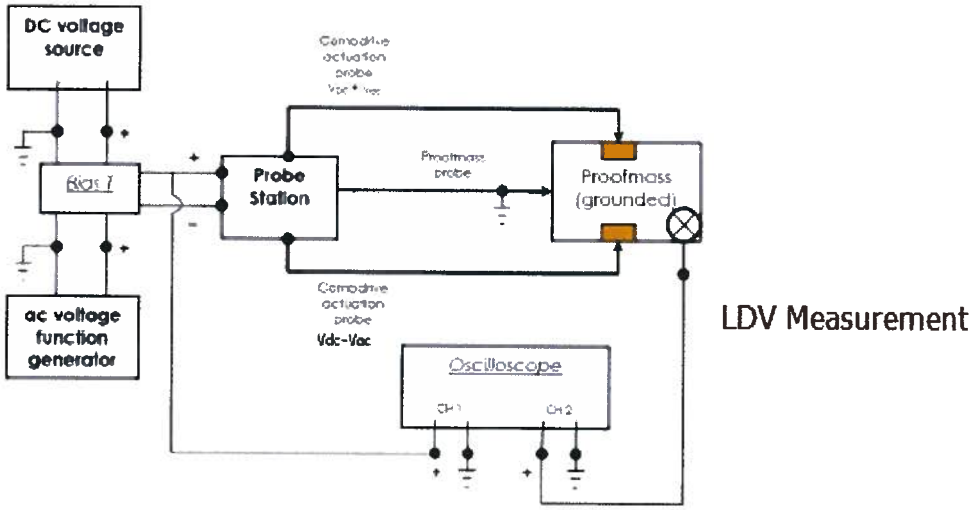


Figure 4-5. Schematic layout showing the characterization of the accelerometer using the LDV Set up[20]

The sensor is driven with a varying frequency AC signal from one end of the drive or sense electrode and then the output is taken from the other end of the electrode.

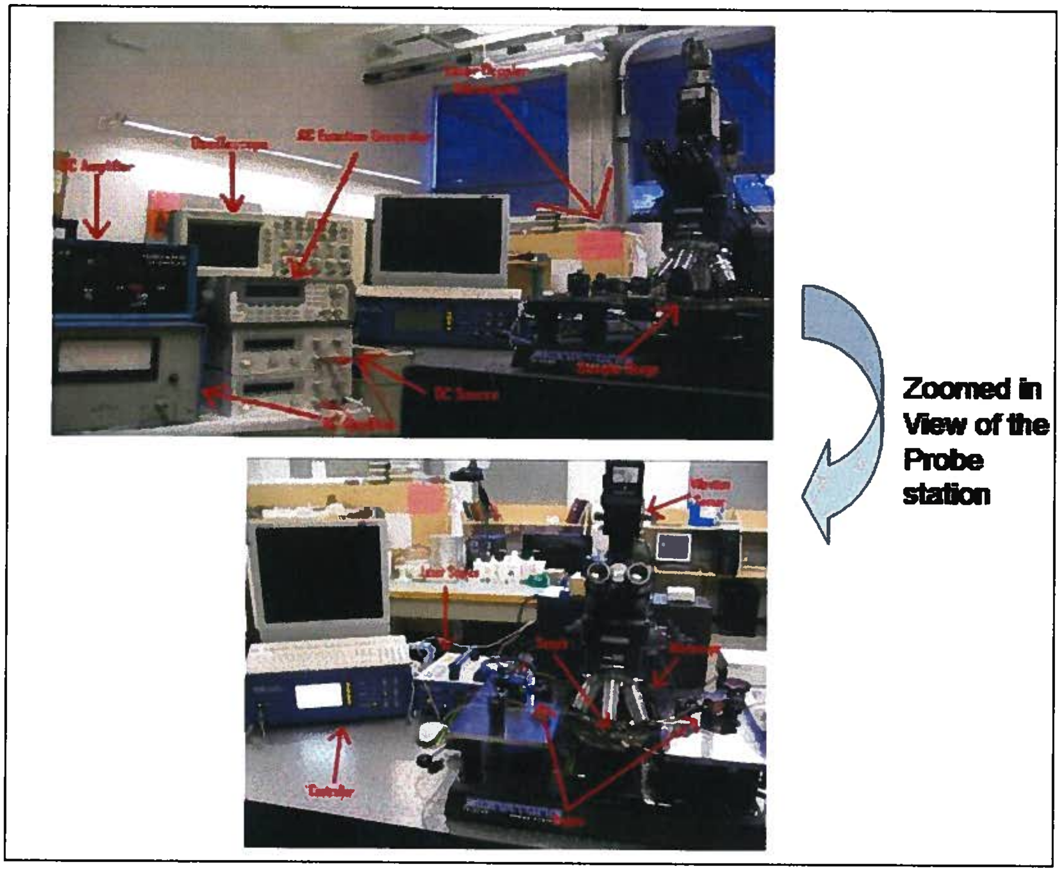


Figure 4-6. AC Measurement Set up using a Linear Doppler Vibrometer (LDV)

## 4.2. The Pull-In Phenomenon

At the beginning of the chapter, pull in results are shown.This section explains the concept of pull-in in detail.The mathematical description of the 'pull-in' phenomenon which can be defined as *the loss of stability at a given state of the system and the stability studies allows, for a given structure and dimensions, the computation of the evolution of the equilibrium points towards the instability and the voltage at which stability is lost.* Pull-in can be examined at two different levels i.e. static and dynamic and this concept is discussed at both the levels.

### 4.2.1. Static Pull-In

This is caused while considering that pull-in is solely due to electrostatic action. Here the inertial and the damping effects are neglected and the variation in the voltage is considered slow enough so that the equilibrium is obtained anytime by the static components[21].

### 4.2.2. Dynamic Pull-In

This is a more accurate analysis as it takes into account the inertial and the damping effects and the additional effect of external acceleration.

### 4.2.3. Pull-in Voltage Based Operation Model

The basic phenomenon is the loss of stability of the equilibrium position. The device under analysis follows the equilibrium principle [14]:

$$F_{inertia}+F_{damping}+F_{elastic}+F_{electrostatic} = 0$$

The device can be analyzed using a dynamic system approach where the system is described by a set of equations. Basically after obtaining the governing equations, analysis of the stability is performed. Let us consider a simple lumped model for analysis as shown in figure 4-7.

The device allows two distinct modes of operation.The first mode is the asymmetric mode where $V_1$=V and $V_2$=0.This is the simplest possible case and it is the most frequently encountered on electrostatic actuation.The second mode is the symmetric mode where $V_1=V_2=V$ corresponds to the case where the two fixed plates on either side of a movable plate.The structure is operated symmetrically which implies that in the zero voltage position the spacing between the two fixed electrodes and the movable plate is equal and both are actuated at the same voltage.

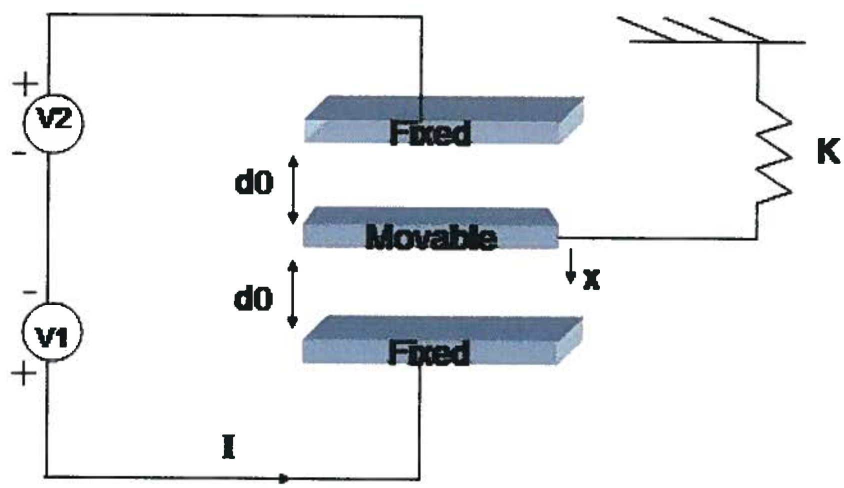


Figure 4-7. Lumped model of the accelerometer for pull-in analysis.Here for Asymmetric mode(V1=V and V2=0) and for Symmetric mode(V1=V2=V)

#### 4.2.3.1. Asymmetric Mode of Operation

The asymmetric mode is the classic situation of a parallel-plate.Two parallel plates are placed separated by a distance $d_0$. The movable plate has 1 DOF varies the inter plate distance.

At the equilibrium position, the elastic force becomes $F_{elastic} = -kx$ and balances the electrostatic force,

$$F_{electrostatic} = \frac{1}{2}C(x)V^2\frac{1}{(d_0-x)} = \frac{1}{2}C_0V^2\frac{d_0}{(d_0-x)^2}$$

Solving the equation in Matlab we obtain the plot as shown in figure 4-8.

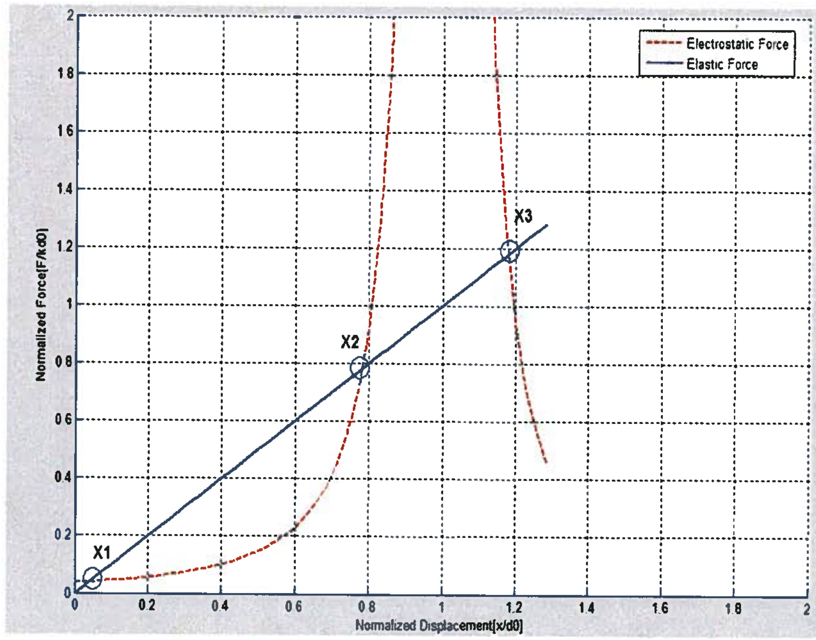


Figure 4-8. Variation of the system forces with x

Three equilibrium points can be seen (corresponding to the zeros of the third order polynomial).Two of them lie in the region $0<x<d_0$.The third one though mathematically correct, is impossible to reach from a physical point of view since it is situated beyond the achievable mechanical displacement.

Considering the other important points $X_1$,$X_2$, around position $X_1$, a small increment of x, causes a larger restoring force ($F_{elastic}$) as compared to the push-away on electrostatic force($F_{electrostatic}$) and vice versa when x decreases.For the unstable solution $X_2$,a small disturbance on the equilibrium position makes the pull away force larger than the restoring force, pushing the displacement even further away from the initial equilibrium.

For small values of V, equilibrium exists and the system is stable.To determine the point of instability, we further analyze the net force equation:

$$F_{net} = F_{electrostatic} + F_{elastic} = C_0 d_0 \frac{V^2}{2(d_0 - x)^2} - kx$$

when differentiated w.r.t 'x',

$$\frac{\partial F_{net}}{\partial x} = C_0 d_0 \frac{V^2}{(d_0 - x)^3} - k$$

For a system to be stable,

$$\frac{\partial F_{net}}{\partial x} < 0 \Rightarrow k > C_0 d_0 \frac{V^2}{(d_0 - x)^3}$$

At the threshold of stability $F_{net}$=0 and the critical point $x_{critical}$ is defined by,

$$k = C_0 d_0 \frac{V^2}{(d_0 - x)^3} \Rightarrow x = C_0 d_0 \frac{V^2}{2k(d_0 - x)^2} \Rightarrow x_{critical} = \frac{1}{3} d_0$$

Hence the pull in voltage ($V_{pi}$) which is necessary to reach the critical deflection $x_{critical}$ can be obtained as,

$$V_{pi} = \sqrt{\frac{8 d_0^{\,2} k}{27 C_0}}$$

For voltage levels higher than the pull-in voltage, the elastic force can no longer compensate for the electrostatic force and the movable plate will collapse or stick towards the fixed one.That is why in the accelerometer, to prevent such a short circuit to occur, a mechanical stopper is designed and placed such that it prevents this collapse to occur. The figure 4-9 shows the triangular shaped sharper edges of the stopper.This is designed so with the intention of decreasing the contact area so that the mass does not stick to the stopper during pull-in.

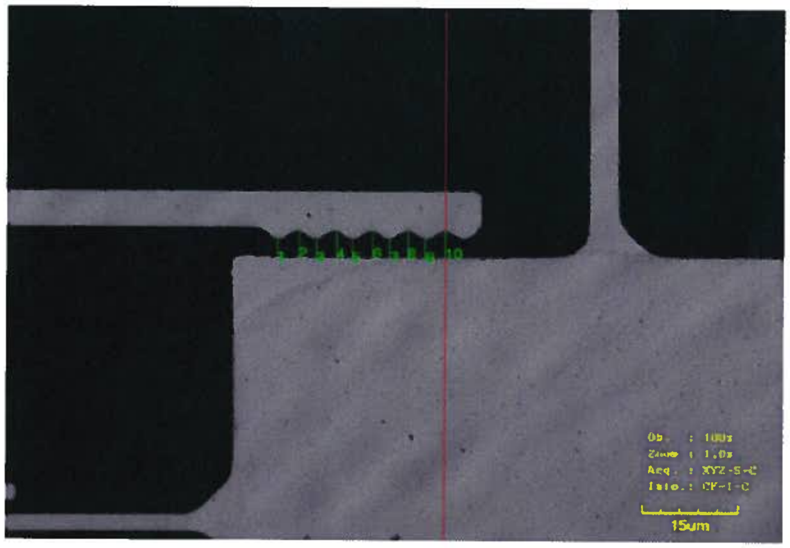


Figure 4-9. SEM picture showing the zoomed view of the stoppers

#### 4.2.3.2. Symmetric Mode of Operation

In this case the two fixed plates on the either side of the movable plate are equidistant. Hence one can assume that the pull-in in the symmetric mode would have a larger pull-in voltage as compared to the asymmetric mode.In the asymmetric mode, the electrostatic force is counteracted by the elastic beam force until the movable plate collapses at the pull-in threshold. However in the symmetric case, the electrostatic fields in the first approximation are balanced.Since the difference between the electrostatic forces is balanced by the elastic force in the symmetric mode, the pull-in is expected to be more abrupt and has a larger value.

Using the principle that the dynamic equilibrium is obtained when the elastic forces balance out the electrostatic forces,

$$F_{electrostatic1} = C_0 d_0 \frac{V^2}{2(d_0 - x)^2}$$

$$F_{electrostatic2} = -C_0 d_0 \frac{V^2}{2(d_0 + x)^2}$$

The determination of the static equilibrium positions results in a polynomial equation of the 4th order of x.

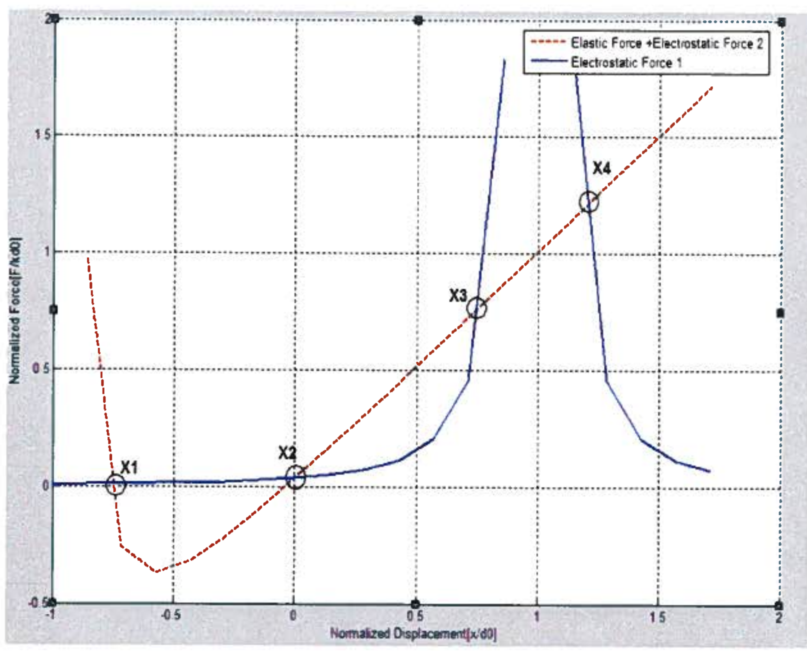


Figure 4-10. Variation of the symmetric system forces with x

The plot shows four equilibrium points for the small voltage applied. A stability analysis of the 3 points of consideration ($X_1$,$X_2$,$X_3$) reveals the existence of one stable point $X_2$ and the other two unstable points $X_1$ and $X_3$ and $X_4$ is physically beyond possible as it falls out of range ($x>d_0$). Performing further analysis the net force is given by,

$$F_{net} = -C_0 d_0 \frac{V^2}{2(d_0+x)^2} + C_0 d_0 \frac{V^2}{2(d_0-x)^2} - kx$$

and the derivative of the w.r.t 'x',

$$\frac{\partial F_{net}}{\partial x} = C_0 d_0 \frac{V^2}{(d_0-x)^3} + C_0 d_0 \frac{V^2}{(d_0+x)^3} - k$$

The equilibrium point $X_2$, which in the symmetric mode is a constant (x=0), is stable for,

$$\frac{\partial F_{net}}{\partial x} < (0, V) \Rightarrow 2C_0 \frac{V^2}{d_0^2} - k < 0 \Rightarrow V < \sqrt{\frac{kd_0^2}{2C_0}}$$

The other two points $X_1$ and $X_3$ are unstable for the above condition and are stable afterwards.

In this analysis the pull-in voltage is a function of the initial capacitor gap which in turn is determined by the acceleration the device is experiencing. If the device is continuously actuated using a ramp voltage and the pull-in voltage is measured, the changes in the pull-in voltage are proportional to the external acceleration.The differential capacitor scheme used in this design allows pulling the structure to pull-in at both sides of the capacitor. If this is done alternatively, the difference in the pull-in voltages gives the measure of the external acceleration the device is experiencing.This method increases the linearity. Second, any drift in time of the pull-in voltage or changes with temperature are cancelled out, which means that no calibration is needed.

### 4.2.4. Pull-In Time Based Operational Model

In this approach the dynamic behaviour of the pull-in phenomenon based on time is analyzed.The operating principle is that when pulsed voltages $f_1$and $f_2$ are applied alternately with voltages higher than the pull in voltage, the structure pulls in up to the stopper position.These originates two pull in times $\tau_1$ and $\tau_2$ corresponding to the travel time between the stoppers.If there is no external acceleration $\tau_1 = \tau_2 = \tau_0$.

Considering the movement of mass between the stoppers,

$$m\ddot{x} + b\dot{x} + kx = \frac{\varepsilon_0 \varepsilon_r}{2(d_0 - x)^2} A V^2$$

*where* V the driving voltage, A the area of the electrode, $d_o$ the initial electrode gap and x the displacement. To keep the device working in the pull-in mode, the driving voltage must be higher than the minimum pull-in voltage and the previous pulse voltage should be held long enough to make sure that the initial condition is
$\dot{x} = 0$

The characteristic equation is given by,

$$\ddot{X} + 2\zeta\dot{X} + X = \frac{\tilde{F}}{(1 - X)^2} + \tilde{a}$$

*where*

$$X = \frac{x}{d_0} \qquad \dot{X} = \frac{d}{d\tau}x \qquad \ddot{X} = \frac{d^2 x}{d\tau^2} \qquad (\tau = \omega t)$$

Also according to definition,

$$\tilde{a} = \frac{ma}{kd_0} \ll 1 \qquad \text{and} \qquad \tilde{F} = \frac{\varepsilon_0 \varepsilon_r A V^2}{2kd_0^{\ 3}}$$

When damping is 0, analytical pull in time can be obtained. Hence the differential pull-in time, can be given by the equation,

$$\Delta\tau = 2s\tilde{a} + \frac{17}{4}n\tilde{a}^3 + \tilde{a}^3 \qquad (\Delta\tau = \tau_2 - \tau_1)$$

*where*

$$s = \int_{-\lambda}^{\lambda} (\lambda + X)^{-\frac{1}{2}} \left( (\lambda - X) + \frac{2\tilde{F}}{(1 - X)(1 + \lambda)} \right)^{-\frac{3}{2}} dX$$

$$n = \int_{-\lambda}^{\lambda} (\lambda + X)^{-\frac{1}{2}} \left( (\lambda - X) + \frac{2\tilde{F}}{(1 - X)(1 + \lambda)} \right)^{-\frac{7}{2}} dX$$

This shows that the pull in time is proportional to the acceleration. A pull-in analysis was conducted using the CoSolve module in CoventorWare. A voltage trajectory is specified, and the displacement is calculated for each voltage up to the pull-in voltage, which is the greatest voltage for which an equilibrium position can be found. At each point of this trajectory the mechanical solver MemMech and the electrostaticsolver MemElectro are employed. In this section, the settings for MemElectro, MemMech, and CoSolve are specified. This analysis is shown in figure 4-11.

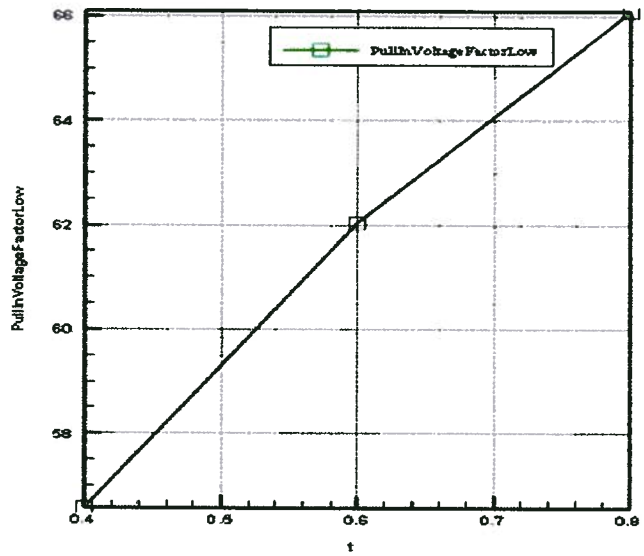


Figure 4-11. Pull-in Voltage variation with time (seconds)

Further analysis on pull-in was done in Matlab. This is shown in figure 4-12. The metastability state occurs when a step input voltage with a higher value than the static pull-in voltage is applied. Since the duration of the metastable region changes with the external acceleration, the pull-in time can be used as a measure of the acceleration. If the structure is constantly actuated with a squared voltage with a period larger than the pull-in time duration, the acceleration is sampled with a frequency equal to the squared voltage with a period larger than the pull-in time duration, the acceleration is sampled with a frequency equal to the squared voltage frequency (Nyquist relation[21]).

When the stability is lost the device moves towards the counter electrode with a certain motion in a well defined amount of time. Pull-in time can be defined as the time the device takes the time the device takes from moving to the stable fixed position to the time it hits the stopper. The "pull-in" is actually the motion of the device during the pull-in time. Figure 4-12 shows both the cases: under damped state and damped state. In the under-

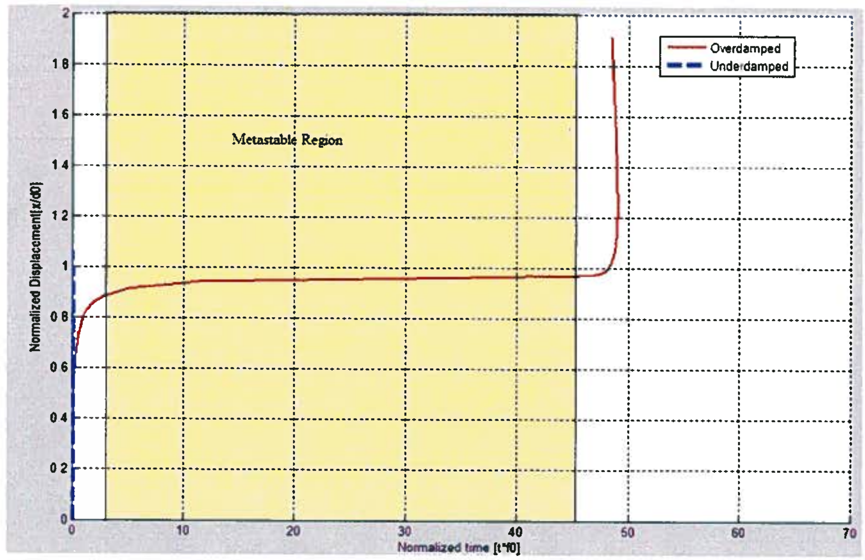


Figure 4-12. Pull-in Displacement-Metastable Region

damped case, the structure rapidly crosses the gap till it hits the stopper. For the over-damped case 3 regions are identified:

- A first region where the structure moves fast till it reaches pull-in. Here at the initial electrostatic force is compensated by the elastic and the damping forces.
- A metastable state which is characterized by almost 0 velocity. At this state the electrostatic force is the same as the elastic force which creates the equilibrium. The damping factor is one of the most important element in the first region and largely determines the duration of the metastable region.
- The third region where the structure hits the stopper. Due to the non linear behaviour of the electrostatic force, the elastic force cannot indefinitely compensate for the electrostatic force and hence pulls-in.

#### 4.2.4.1. Meta-Stable Region

The meta stable region is characterized by a very small variation of the displacement, $x_n$ around the static pull-in displacement ($x_{pi}$). If only the region around $x_{pi}$ is considered, a linearization of the equation of motion can be realized which results in a second order system. The linearized differential equation can be analytically solved and an expression for the pull-in time can be found.

The normalized non linear equation of motion is given by [14],

$$\frac{d^2 x_n}{dt^2} + \frac{\omega_o}{Q}\frac{dx_n}{dt} + \omega_o^2 x_n = a_n + \frac{4}{27}\frac{(\omega_o^2 V_n^2)}{(1-x_n)}$$

By approximating this equation using Taylors series in the interval that x is less than one third the distance, we can get the second order dynamic equation of the system. Hence if the device is made to operate in the meta stable region, the performance characteristics are better.

### 4.2.5. Simulink Model of the Pull-in Accelerometer

Figure 4-13 shows the simulink block diagram of the pull-in based accelerometer. The behaviour of the accelerometer is studies from the time a step input voltage is applied till pull-in occurs ($x=1/3d_0$).

The important aspect is the high sensitivity of the transition time to an external acceleration. This is due to the intrinsic behaviour of the metastable region which was explained in the earlier section. Since the region is best described by an equilibrium of

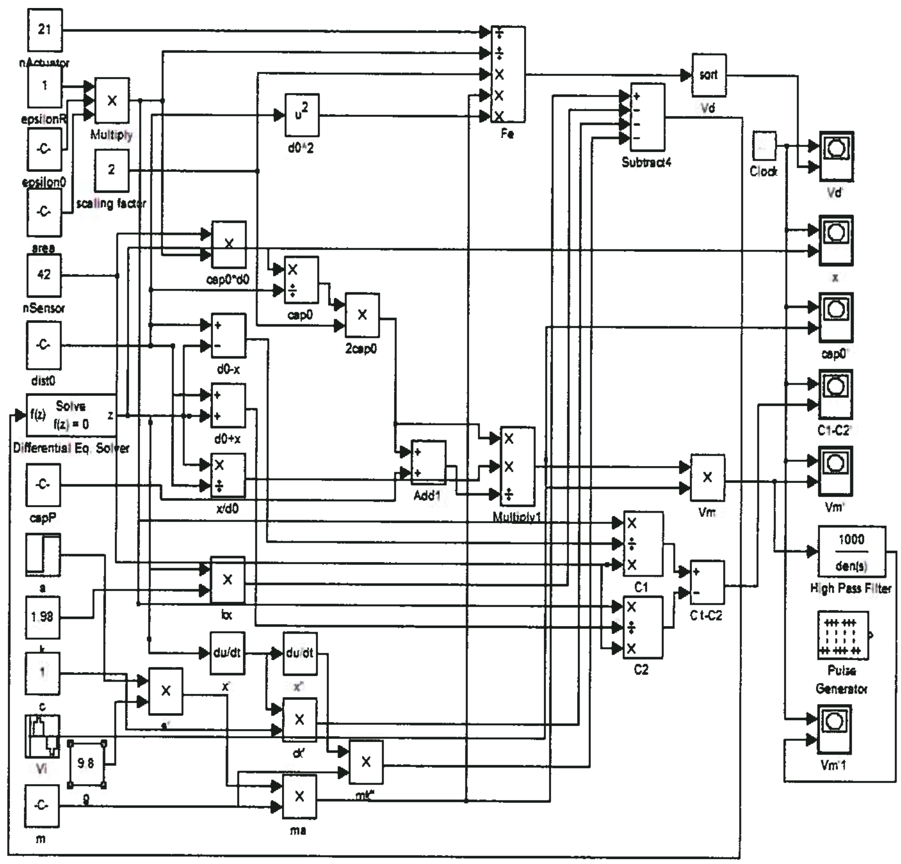


Figure 4-13. Simulink Model of the Pull-in accelerometer

forces, any small change acts as a pertubation to the metastable equilibrium, thus providing the means to achieve a very high sensitivity on the time domain.The figure 4-14 shows the simulated pull-in changes at the metastable region.

## 4.3. Hysteresis

The other important aspect associated with the pull-in phenomenon is called hysteresis. When pull-in occurs, there is an imbalance between the electrostatic and elastic forces and the resulting net force drives the movable part from reaching the stopper and

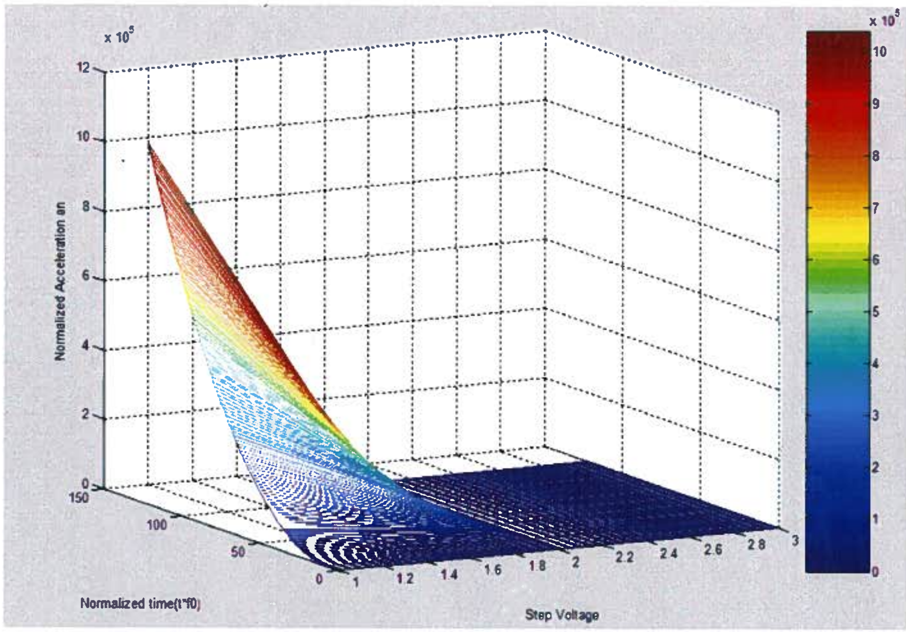


Figure 4-14. Simulated pull-in time changes with voltage and acceleration with respect to normalized time

thus avoiding the short circuit between the fingers. When the stopper is hit, a reaction force develops that helps in reaching an equilibrium state.

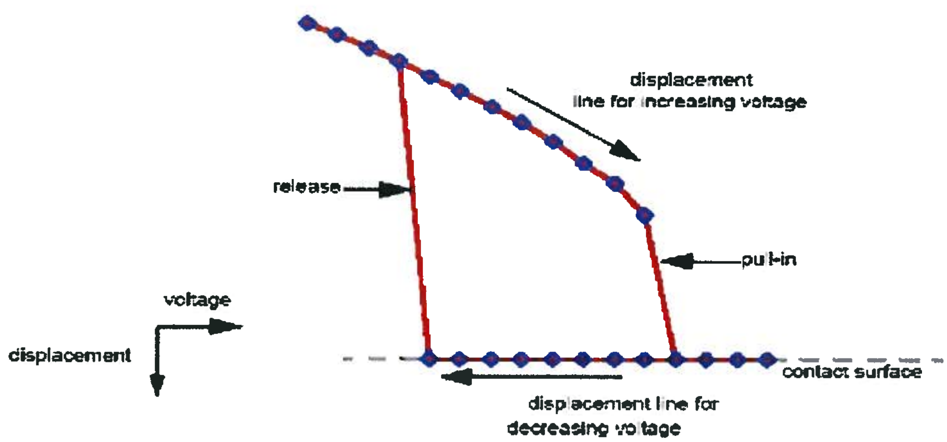


Figure 4-15. Mechanism of formation of Hysteresis

The hysteresis characteristics of the beam was analyzed by observing the effects of an increasing and decreasing voltage ramp on the beam response. Previously, the beam pull-in voltage was solved, where the growth of the electrostatic force was dominant over the linearly increasing mechanical restoring force, and the beam quickly snapped, or pulled-in, to the ground plane. Once the beam touched the contact surface, a release voltage can be solved, which is the voltage at which the electrostatic force exactly balances the spring force of the pulled-in beam. Between the pull-in and the release voltages, the beam has two valid solutions and exhibits what is known as hysteresis. The pull-in voltage is observed by a linearly increasing voltage ramp, while the release voltage is observed by a linearly decreasing voltage ramp. This is graphically demonstrated in figure 4-15.

CoSolve uses the trajectory function to solve for the hysteresis effect.A contact surface like the stopper must be defined for this analysis. A single voltage ramp is specified and CoSolve automatically generates the increasing and decreasing segments from this specification. Both pull-in and release voltages are observed in a single simulation pass. This is shown in Figure 4-16.

To get more accurate results. this process needs to be iterated for the different values of x and using smaller trajectory steps to find more accurate pull-in and release values.

## 4.4. Damping

Damping is any effect, either deliberately engendered or inherent to a system, that tends to reduce the amplitude of oscillations of an oscillatory system.Usually in case of

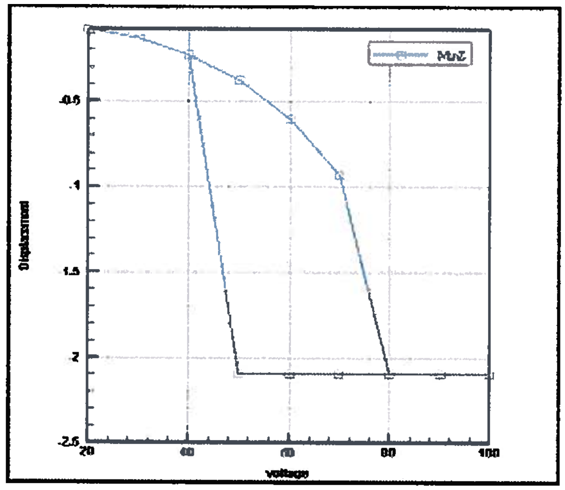

Figure 4-16. The hysteresis loop obtained from Covent ware to measure pull in and release

MEMS air damping is one of the critical factors considered while determine the performance (mainly dynamic due to the large surface area to volume ratio of the moving parts) of the system.For some of the MEMS devices the energy consumed by the air damping parts must be minimized so that the motion of the moving parts can be maximized with a limited energy supply.

There are mainly two types of damping[14]:

- Squeeze Film Damping
- Slide Film Damping

### 4.4.1. Damping Analysis

Let us first analytically calculate the damping coefficient and then verify the same using simulations.

#### 4.4.1.1. Squeeze film Damping

The movement of a parallel-plate type device where the gap size of the plate changes in a oscillatory manner, squeezing the trapped fluid out and sucking it in, gives origin to squeeze film damping. Fluid (usually air) is trapped between the movable electrode and the fixed one, resulting in squeeze-film forces that can not be neglected.

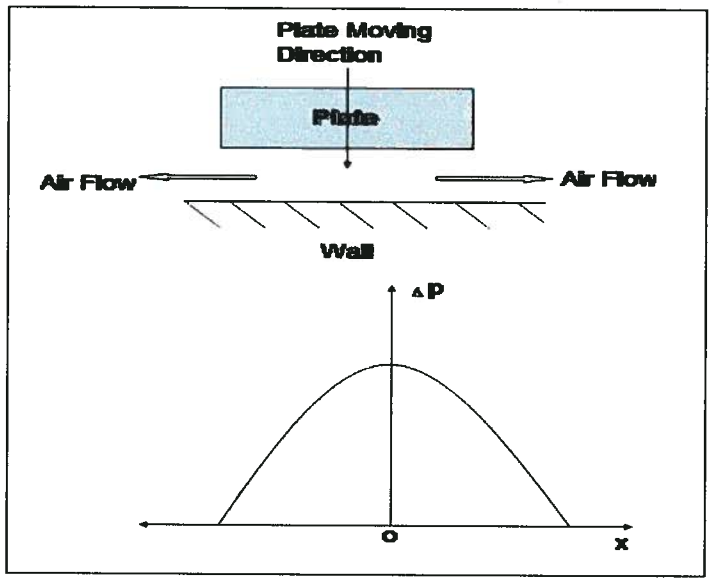


Figure 4-17. Pressure built up by Squeeze Film motion

When a plate is parallel to a substrate and moving towards the substrate, the air film between the plate and the substrate is squeezed so that some of the air flows out of the gap. Therefore, an additional pressure $\Delta p$ develops in the gap due to the viscous flow of the air as shown in the above figure. On the contrary, when the plate is moving away from the substrate the pressure in the gap is reduced to keep the air flowing into the gap.In both cases, the forces on the plate caused by the built up pressure are always against the movement of the plate. The work done by the plate is consumed by the viscous flow of the air transformed into heat. The air film acts as a damper and the damping is called squeeze film damping.

The damping force of the squeeze film air damping is dependent on the gap distance; the smaller the gap, the larger the damping force. When the plate of substrate s very far from the substrate, the pressure built up is negligible and the damping force will be reduced to a 'drag force'.

The relation between velocity, pressure, density and viscosity for an isotropic Newtonian Fluid (usually air) with a laminar gas flow can be calculated using the Navier Stokes Equation and the Continuity Equation [14].The following assumptions are made:

1. *Curvature:* The surface of the plate and the substrates are parallel and the motion is perpendicular to the surfaces. The critical dimension is the film thickness which is considered uniform.

2. *Isothermal:* Since volumes are small and surface areas are large, the thermal contact between the solid and fluid is very good in MEMS devices. Further such materials also have a very large heat capacity. Hence the gas film is considered isothermal and therefore the density is proportional to absolute temperature.

3. *Inertia:* Since the inertial forces are small when compared to viscous forces for typical MEMS dimensions, the gas inertia can be neglected. The contribution of the gas inertia can be considered small when the Reynolds number with respect to squeeze motion is small and the condition for this is that $\rho\omega\eta^2/h \ll 1$,where $\omega$ is the frequency of movement, $\rho$ is the density, $\eta$ is the viscosity of the gas and h is the thickness of the film.

With these assumptions in mind the Naviers Stoke's equation can be simplified into the compressible gas film Reynolds equation in a 2D is:

$$\frac{\partial}{\partial x}\left(\frac{h^3\rho}{\eta}\frac{\partial p}{\partial x}\right)+\frac{\partial}{\partial y}\left(\frac{h^3\rho}{\eta}\frac{\partial p}{\partial y}\right) = 12\frac{\partial}{\partial t}(\rho h)$$

where p is the pressure, r is the density, h is the viscosity of the gas and h is the film thickness. Since $\rho p^{-n}$ is a constant and for a isothermal process n=1, the density can be replaced with pressure.

As the damping in an accelerometer is usually changed with the displacement, the influence of the variable damping is also analysed. For the different damping ratios the gain (fF/g) was plotted in matlab.From the output graph that we obtain. we determine that the gain increases with damping and the saturates when the damping ratio $\zeta$ is larger than 1.This corresponds to the dominant damping in the system is supposed to be the squeeze film damping .

From the principles[22,23,24], it can be established that sensing attributes to the squeeze film damping. When a damping analysis was done in Conventorware, the following results was obtained.For squeezed-film physics, DampingMM used in CoventorWare bases macro model extraction on a 2D finite element solution of the linearized Reynold's equation.

Using the settings as Temperature =300K for temperature and 1 atmospheric pressure, the damping and spring forces where estimated.It is found that the damping is highest

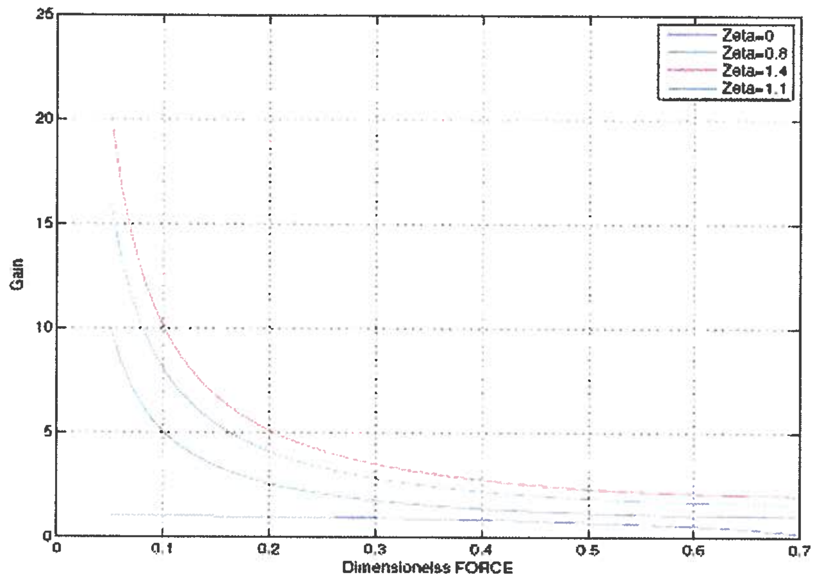


Figure 4-18. Variation of gain with different damping ratios

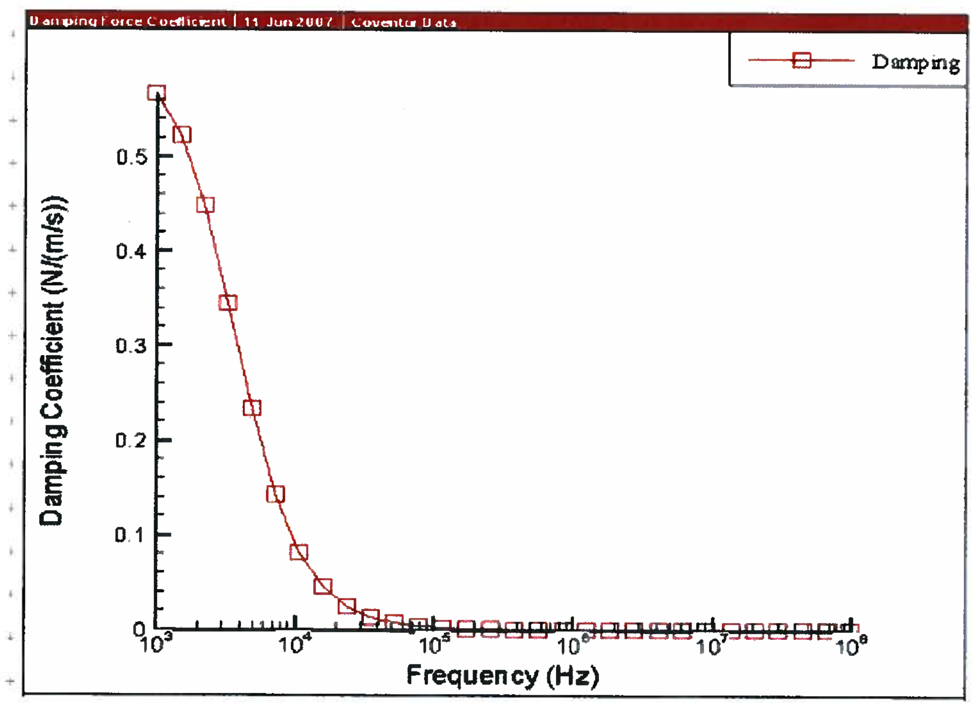


Figure 4-19. Graph showing a variation in the Damping Coefficient with respect to varying Frequency

between $10^3$ Hz and $10^4$ Hz and then slowly decreases where as the spring forces become a constant around $10^4$ Hz. This is shown in figure 4-20.

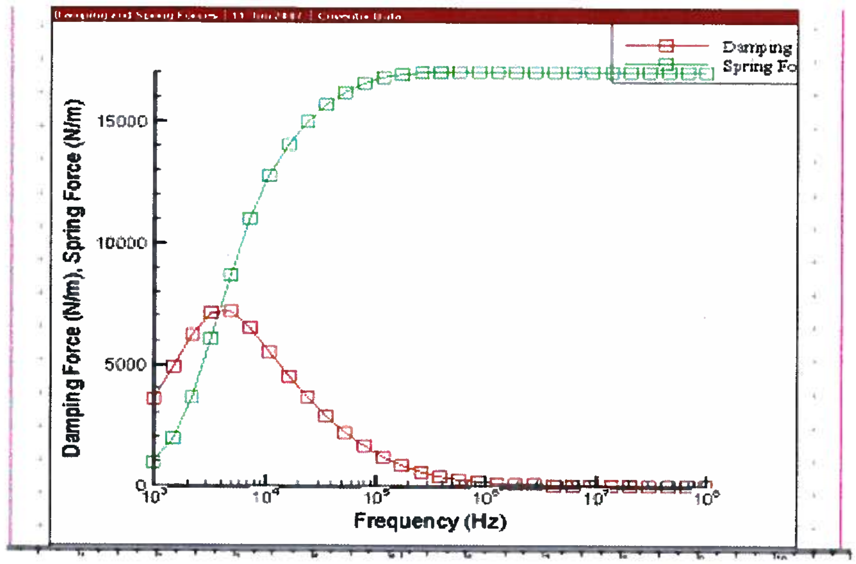


Figure 4-20. Damping and Spring Forces in case of Squeeze Film Damping

#### 4.4.1.2. Slide Film Damping

Also called the rarefied damping, it is not very significant when compared to the squeeze film damping. It is contributed by the actuation fingers which move sideways in the X direction. The figure 4-21 explains the concept of slide film damping.

The equation is given by

$$C_{\text{side film}} = N\mu p\frac{A}{d_0}$$

*where* N is the number of fingers, m is the viscosity, p is the pressure and A is the area between the plates and $d_0$ is the distance between the plates.

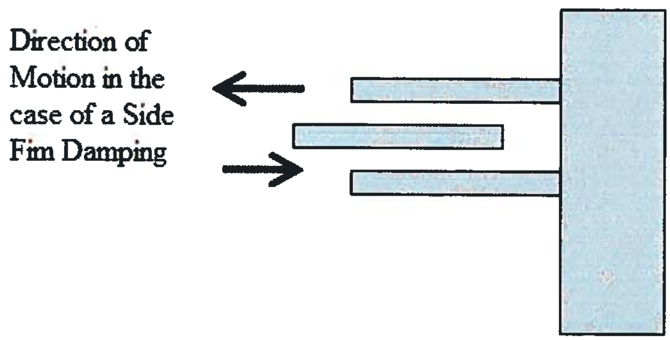


Figure 4-21. Slide Film Damping

Hence for a total of 40 fingers,

$$C_{\text{slide film}} = 40 \text{ x } 2.4 \text{ x } 10^{-9} = 96 \text{ x } 10^{-9} F$$

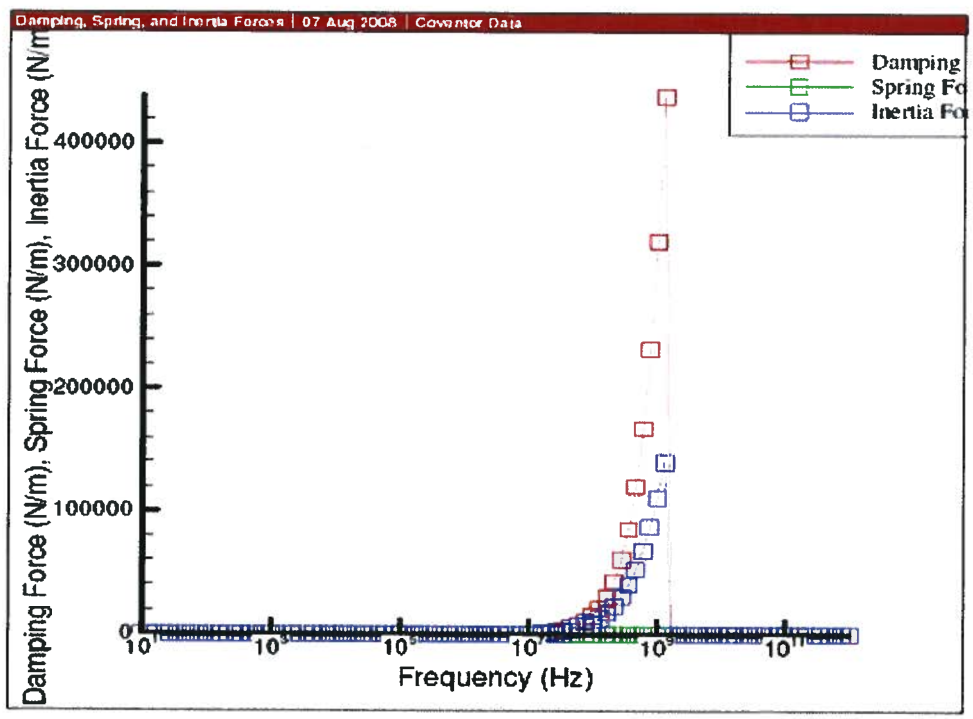


Figure 4-22. Slide Film Damping

Since this is very small in comparison with Squeeze Film damping, its effect is not very significant. The figure 4-22 shows the simulation done using Coventorware to verify the slide film damping.

## 4.5. Noise Analysis

For any given inertial sensor the main computational aspects of noise are[25,26]: equivalent force noise.

- equivalent acceleration noise imposes a lower threshold in the minimum level of detectable acceleration.
- equivalent displacement noise.
- equivalent capacity variation noise to compare with the resolution of the capacitive readout.

We rely on the general accelerometer equation, augmented with the mechano-thermal noise force:

$$\left(m\frac{d^2x}{dt^2} + b\frac{dx}{dt} + kx\right) = F_{ext}(t) + F_{noise}(b, t)$$

Here, $F_{noise}(b,t)$ represents the random contribution of the different noise-generating processes. Because we assume a thermal equilibrium between the accelerometer and the surroundings, the energy lost toward the environment through the dissipative friction (b coefficient) must equal in average the energy gained through the noise force.

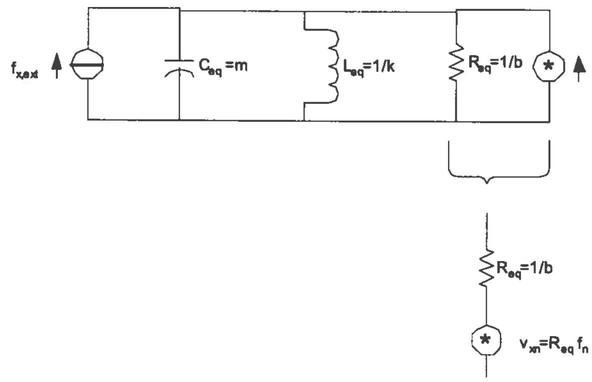


Figure 4-23. General Model of an Accelerometer

#### 4.5.0.1. Equivalent noise force:

As shown before, the spectral noise force distribution is white noise:

$$\sqrt{\overline{F_n^{\,2}}(f))} = \sqrt{4k_BTb}\ [\mathrm{N}/\sqrt{Hz}]$$

In a frequency bandwidth, the total noise force will be (assuming b(f)=ct):

$$\sqrt{\overline{F_n^{\,2}}(f))} = \sqrt{4k_BTb\Delta f}\ [\mathrm{N}/\sqrt{Hz}]$$

#### 4.5.0.2. Equivalent noise acceleration

The equivalent acceleration noise is therefore:

$$a_n = \frac{f_n}{m} \Rightarrow <A_n^{\,2}(f)>=\frac{F_n^{\,2}(f)}{m^2} = \frac{4k_BTb}{m^2} = \sqrt{\overline{A_n^{\,2}}(f))}$$

For the total acceleration noise in a bandwidth,

$$\sqrt{\overline{A_n^{\,2}}}(f) = \frac{\sqrt{4k_BTb\Delta f}}{m}\left[\frac{m}{s^2}/\sqrt{Hz}\right]$$

### 4.5.0.3. Equivalent noise displacement

From the equivalent electrical network, it results

$$Z = \frac{1}{sm + \frac{k}{s} + b} = \frac{s}{s^2 m + bs + k} \Rightarrow V_x(s) = F(s)\frac{s}{s^2 m + bs + k}$$

$$X[s] = \frac{F[s]}{m}\frac{1}{s^2 + \frac{\omega_0}{Q} + \omega_0^{\,2}} \Rightarrow x_{static}\frac{1}{\frac{s^2}{\omega_0^{\,2}} + \frac{1}{Q}\frac{s}{\omega_0} + 1}$$

In terms of noise, one has:

$$X_n^2[\omega] = A_n^2[\omega]\left(\left|\frac{1}{s^2 + \frac{\omega_0}{Q} + \omega_0^{\,2}}\right|\right)^2$$

Assuming the white noise input of the acceleration, the total noise displacement (maximum noise power can be obtained by integrating over all bandwidth) will be:

$$\overline{x_n^2} = \int_0^\infty X_n^2[\omega]d\omega = \frac{2k_BT}{\pi m}\frac{1}{\omega_0^2}\left(\frac{1}{Q}\right)\int_0^\infty \frac{1}{(1-y^2)^2 + \frac{1}{Q^2}y^2}dy$$

$$\frac{k_BT}{k}\frac{2}{\pi Q}\int_0^\infty \frac{1}{(1-y^2)^2 + \frac{1}{Q^2}y^2}dy$$

If the processed bandwidth is limited (to the signal bandwidth), then the equivalent displacement noise becomes:

$$\sqrt{\overline{x_n^2}} = \sqrt{\frac{k_BT}{k}\frac{2}{\pi Q}\int_{\omega_L}^{\omega_H} \frac{1}{(1-y^2)^2 + \frac{1}{Q^2}y^2}dy} \text{ [m]}$$

The spectral power function for different values of the quality factor Q was plotted (Figure 4-23). For $0<Q<1/2$, there is no local maximum except for $y=0$ ($\omega=0$).The integral becomes different more as Q tends to 0. For Q tending to 0, the damping is so high, that the transfer function becomes 0 (all-stop filter). No signal could pass either.The maximum sensitivity is around resonance ($\omega=\omega_0$), and the maximum value is $Q^2$. As far as $Q>1/2$, the structure will preserve a local maximum at $\omega=\omega_0<1$, corresponding to the natural damped resonance frequency (So it behaves like a damped oscillator). At $Q=1/2$, the local maximum coincides with $y=0$. For $Q<1/2$, the over damping “kills” the resonant behaviour, and no local maximum except for $\omega=0$, could be observed.

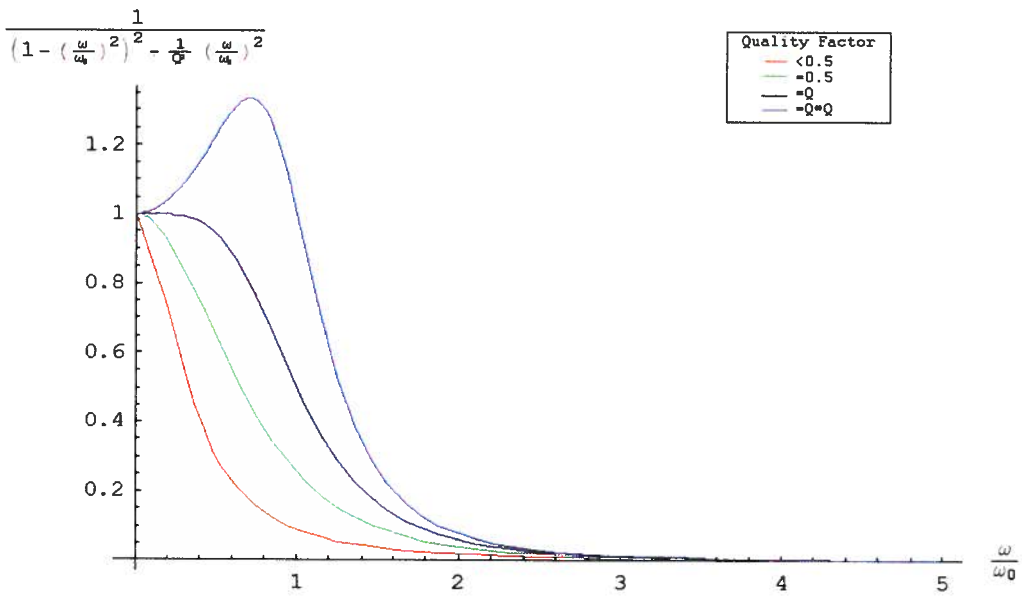


Figure 4-24. Spectral Power Function for different Values of Q

The physical interpretation is that for Q<1/2 the vibratory degree of freedom x disappears, and the structure behaves simply as a sharp ($2^{nd}$ order) low-pass filter.

#### 4.5.0.4. Equivalent Capacitance Noise:

The relation between capacity and displacement is non-linear, but it may be linearized for small variations:

$$C = \varepsilon\frac{A}{d_0 - x} = C_0\left(\frac{1}{1-\frac{x}{d_0}}\right) \approx C_0\left(1+\frac{x}{d_0}\right)$$

It results for the equivalent capacitance noise:

$$\sqrt{\overline{\delta C_n^2}} = \frac{C_0}{d_0}\sqrt{\overline{x_n}^2} \leq \frac{C_0}{d_0}\frac{k_B T}{k}$$

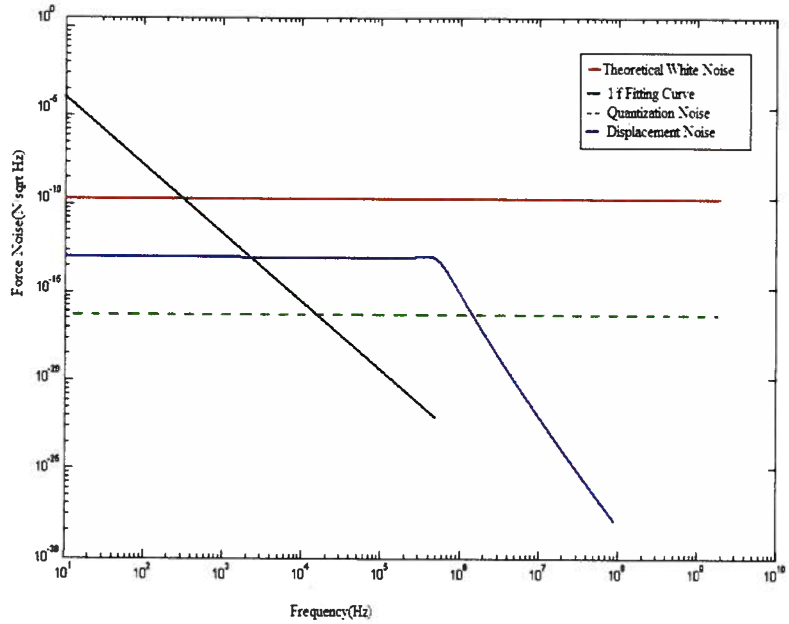


Figure 4-25. The Different Force Noises of the accelerometer model

### 4.5.1. Noise based Optimization

A design for high sensitivity accelerometer needs to take also into account the noise shaping induced by damping phenomena. Noise is defined as the minimum acceleration detected by the accelerometer. Both the mechanical and electrical parts contribute to the noise.The existing scientific literature analyzes the mechano-thermal noise in microstructures based on the assumption of a constant damping coefficient [27,28]. This might be a correct assumption for low-frequencies, but fails to consider the more complex behavior of gas damping as the operating frequency increases, which is the case for resonators and resonating sensors. There are nevertheless detailed models of the combined elasto-damping action of the gas upon the movable plate in the case of squeeze-film damping [22,23,24], but without considering its impact on noise analysis. The present work bridges these two aspects and presents a noise analysis and optimization process based on simulated behavior of a MEMS accelerometer. The damping force is defined by the equation[14]:

$$F_d = \frac{64\sigma PA}{\pi^6 h_0} \sum_{m,n=odd} \frac{m^2 + \left(\frac{n}{\beta}\right)^2}{(mn)^2\left[\left(m^2 + \left(\frac{n}{\beta}\right)^2\right)^2 + \frac{\sigma^2}{\pi^4}\right]}$$

*where* $A=wl$ is the surface area, $b=l/w$ and the squeeze number s is given by,

$$\sigma = \frac{12\eta_{eff} w^2}{P h_0^2}\omega$$

For lower frequencies the damping force depends linearly on the velocity of the plate and the film behaves as a pure damper. At higher frequencies the relation becomes non linear and the spring forces increases and the film acts like a spring. There is a particular frequency at which the damping and the spring forces are equal and this is called the cut off frequency which is given by the relation,

$$\omega_c = \frac{\pi^2 P h_0^2}{12\eta_{eff}}\left(\frac{1}{l^2} + \frac{1}{w^2}\right)$$

A very suitable approach to model the solution of the linearized Reynolds is presented in Figure 4-26 where the damping force can be represented by a network of frequency independent spring-damper elements as shown.The first capacitor represents the

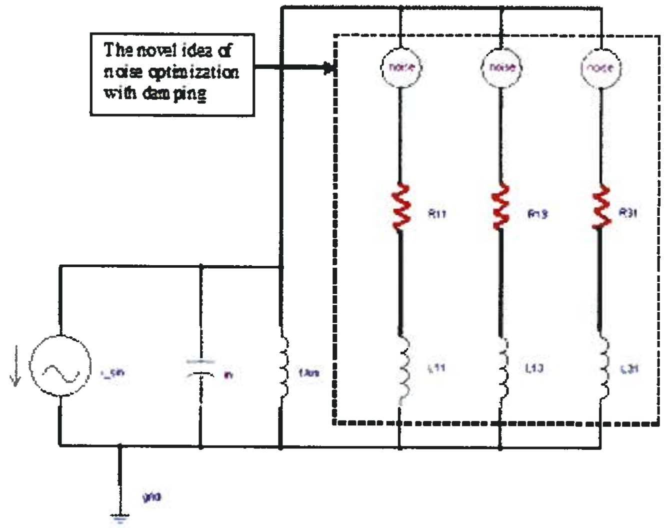


Figure 4-26. Gas-Film Damping model with noise optimization[29]

mass, and the next branch represents the spring stiffness. The following parallel branches of resistors are modelled from damping and the inductors correspond to the noise.

The design and optimization flow is illustrated in Figure 4-27, as implemented in CoventorWare software suite. Extensive finite element analysis of gas damping for small vertical displacements of the movable part lead to the equivalent gas damping and spring constants, $b(j)$ and $k_d(j)$. The resulting complex admittance curve $Y_d(j\omega)= b(j)-jk_d(j)$ whose frequency-dependent magnitude is then introduced in the equivalent circuit representation of the MEMS device. The frequency-dependent conductance $b(j)$ is the source of the mechano-thermal noise limiting the signal-to-noise ratio of the sensor. It generates an equivalent noise force with a spectral density given, for thermodynamic equilibrium, by the Nyquist relation[21].

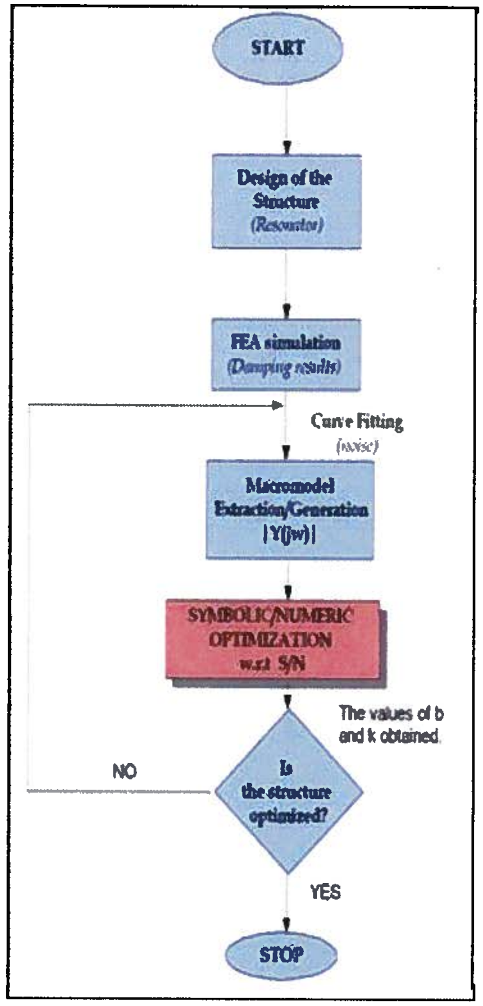


Figure 4-27. Flow chart representing the tool for Noise optimization of a MEMS resonant structure

Two categories of macro models have been implemented for performing the noise analysis. The first one uses interpolation functions for synthesizing *b(j)* and $k_d(j)$ in the frequency domain. It allows a detailed noise and small signal AC analysis of the equivalent device macro model, but it is not for time-domain (transient) simulations. Therefore a second model is synthesized from simulated data, valid for both time and frequency analysis domains. Mathematica was used for the generation of a macro model represented in

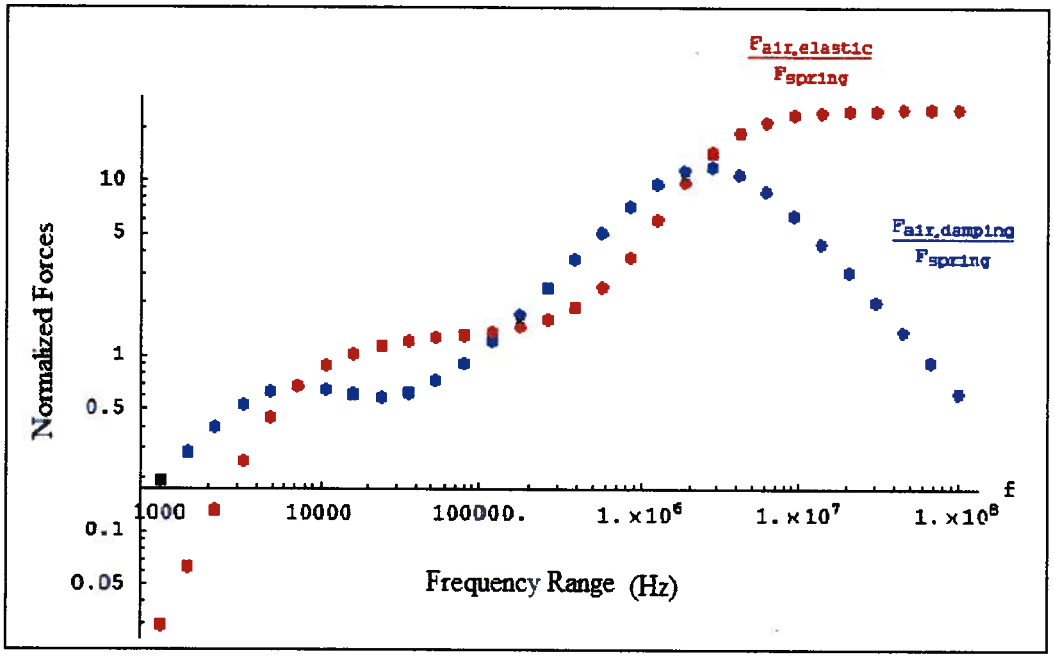


Figure 4-28. Normalized air induced forces

terms of lumped circuit elements with constant values, based on the general squeezed-film damping theory[22]. The equivalent gas admittance $Y_d(j\omega)$ is used for performing the noise analysis of the structure and compute the equivalent input and output noise sources. Their frequency dependence, shaped by the presence of the elastic component in $Y_d(j\omega)$. A signal-to-noise ratio optimization procedure, illustrated in the flow diagram from Figure 4-27, exploits the spectral noise shaping of the equivalent input noise source, and tunes the mechanical suspensions to an optimal value.

Figure 4-28 shows the normalized force forces with the change on frequency.As expected both will tend to 0 as the frequency tends to 0. The presented detailed noise analysis and optimization procedures are applicable to any general micro-electromechanical structures and allow a structured designed process targeting a maximum attainable signal-to-noise ratio performance.

There are two possibilities for a more rigorous noise analysis:

(i) considering a frequency-variable admittance

$$Y_d[j\omega] = b[j\omega] - j\frac{k_d[j\omega]}{\omega}$$

*where* b and $k_d$ are given as Interpolating Function objects (interpolated from the simulated/measured data).

(ii) approximating $Y_d[jw]$ with a finite set of branches of impedance

$$Z_{mn} = \frac{1}{b_{mn}} + \frac{j}{k_{mn}}$$

The next step is to determine the values of $b_{mn}$ and $k_{mn}$ for different values of m and n. This value was then curve fitted with the original values of b and k obtained from the damping simulation in CoventorWare 2006 (Figure 4-29).

This is followed by the calculation of the admittance curve. The equivalent gas admittance $Y_d(jw)$ is used for performing the noise analysis of the structure and computes the equivalent input and output noise sources. Their frequency dependence, shaped by the presence of the elastic component in $Y_d(jw)$, is shown in figure 4-30.

The frequency-dependent noise analysis offers a more accurate description and further insight than the white noise approximation. In the case of inertial resonant sensors like accelerometers, it suggests the optimum frequency range of operation in order to

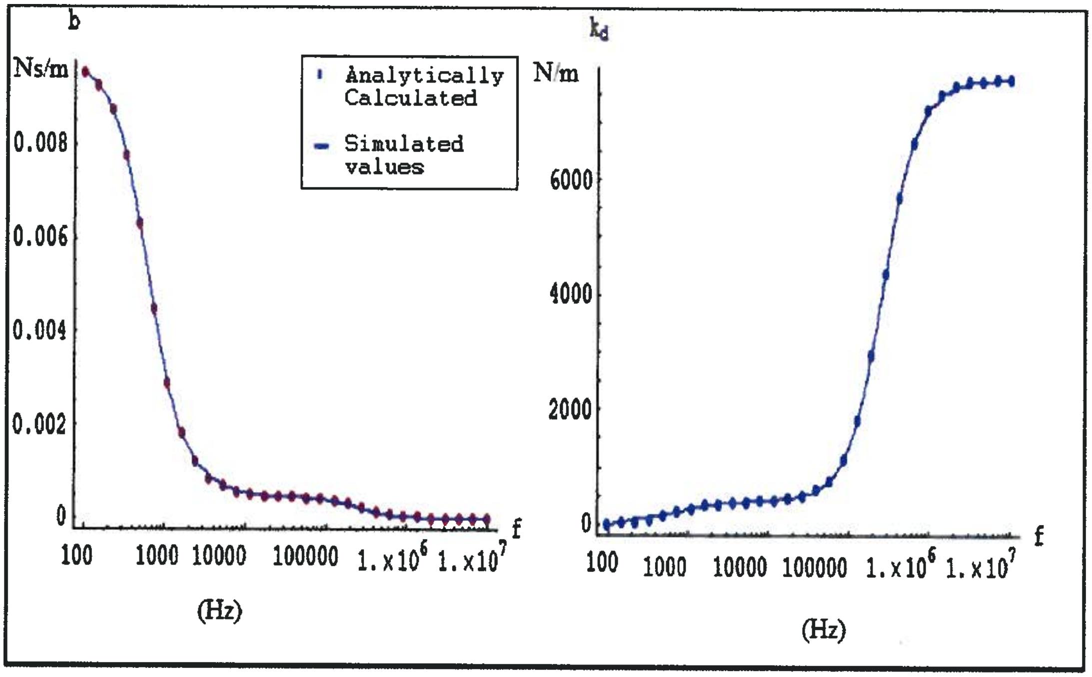


Figure 4-29. The comparative study of the damping and spring constants simulated Vs. Analytically determined using the noise Model

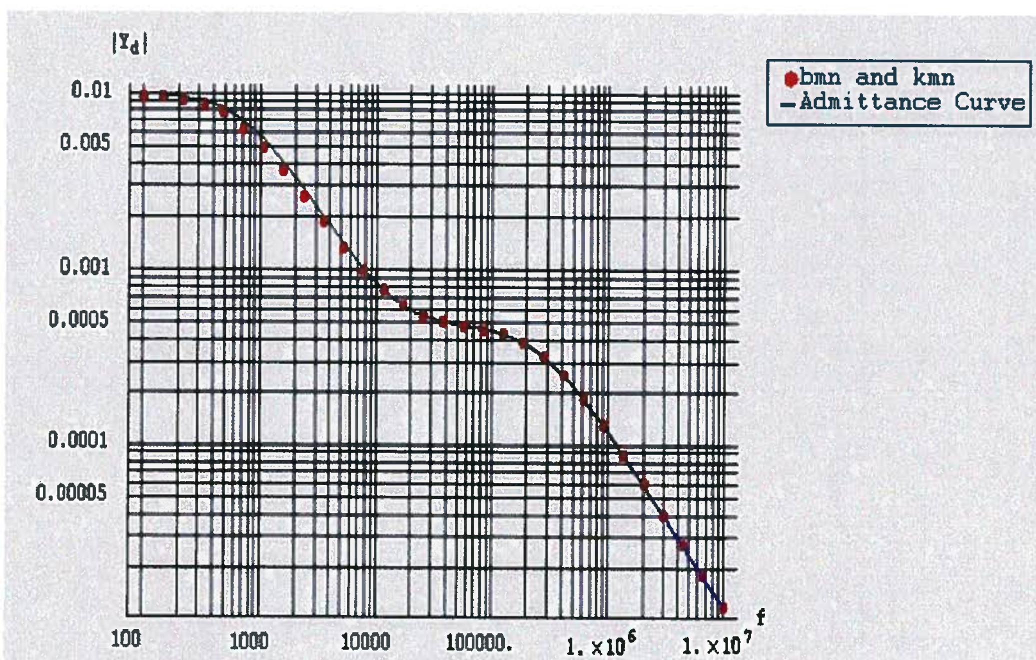


Figure 4-30. Admittance Curve Fitting

achieve both a large output signal and a low noise. The optimization is made with respect to several design criteria:

- A good SNR in terms of output displacement – a matching between the noise induced in the mechanical domain and the equivalent electrical input noise is desired.
- A good sensitivity to input inertial signals, that is, the amplitude of the resonance peak to be as high as possible.
- Bandwidth requirements – different operating bandwidths are necessary for different applications.
- Cross-sensitivities to excitations along other orientations, etc.

A signal-to-noise ratio optimization procedure, exploits the spectral noise shaping of the equivalent input noise source, and tunes the mechanical suspensions to an optimal value. The Signal to Noise Ratio (S/N) is frequency independent if given in terms of the input acceleration which is formulated as

$$\frac{S}{N} = \frac{|A_{ext}(j\omega)|}{|A_{noise}(j\omega)|} = \frac{m|A_{ext}(j\omega)|}{\sqrt{4k_B T b(j\omega)}}$$

In figure 4-31 two different values of resonant frequencies are plotted, one which considers no damping and noise into effect and the other curve is one which considers the damping and stiffness coefficient derived from the from the noise and damping based macro model which was explained earlier.

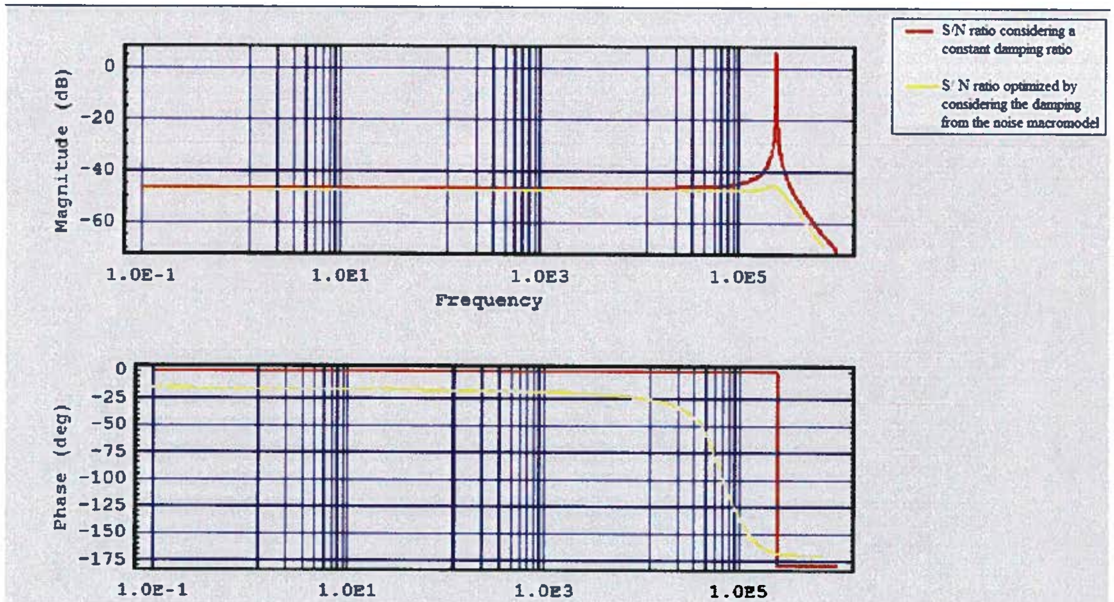


Figure 4-31. S/N curve based on noise based optimization

# 5 APPLICATIONS

## 5.1. Applications

In the past few decades, accelerometers have found themselves being adopted into a wide variety of disciplines. Since they are one of the most earliest MEMS sensor designed, researchers have been constantly trying to find newer and convenient applications for them. Based on the characteristics of the given accelerometer two such applications are discussed in this chapter.

### 5.1.1. Minimally Invasive Surgery

The application of micro electromechanical systems (MEMS) to medicine can be classified into three types, i.e. diagnostic micro systems, surgical micro systems and therapeutic Microsystems [31]. The accelerometer designed for this thesis will help to broaden further on the road presented above in the field of Surgical micro systems by bringing a modern approach to the design of a MEMS sensor cluster to help in navigated surgery. It adds a concrete application challenge to the research program envisaged above.

#### 5.1.1.1. Present State of Art

The research activity of MEMS in the field of surgical applications is creating technological advances in that field. The most primitive and traditional technique is the "Open Surgery" in which the surgeon has a full and direct view of the surgical area, and is able to put his hands directly into the patient [31]. As mentioned by the Spine Universe Web Founder, Stewart G. Eidelson, M.D.,"Open procedures require larger incisions, muscle stripping, more anesthesia, operating time, hospitalization and, the patient usually needs more time to recuperate". This enables the surgeon to come into contact with organs and tissue and manipulate them freely. This is the traditional surgical technique and most surgeons were trained in this manner. While the large incision gives the surgeon a wide range of motion to do very fine controlled operations, it causes a lot of trauma to the patient [31].

During the last decade minimally invasive surgery has become the leading method for many surgical interventions. Unlike open surgery, Minimally Invasive Surgery (MIS) only needs small incisions in the patient's body (Figure 5-1). Hence MIS benefits patients because of less pain, less trauma and shorter healing periods [32]. Medical navigation systems are mainly used for monitoring the position of surgical instruments relative to patient body.

Some optical navigation systems have presently a limited applicability (e.g. in neurosurgery), but their use is hindered by the high cost and the need of a direct line of sight between the surgical instrument and a video-camera. Though MIS has many advantages, it also has a lot of disadvantages as well. During the operation, the surgeon must not only look at the video image of the surgery but also maintain a correlation between his hand and

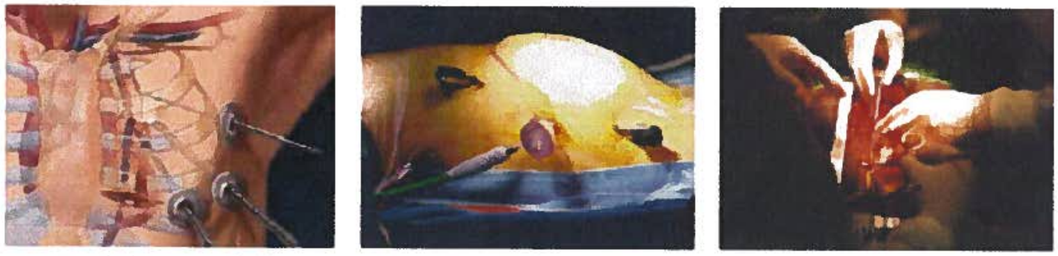

(a) Schematic MIS (b) Minimally Invasive (c) Open Surgery

Figure 5-1. Open Vs. Minimally Invasive Surgery[33]

tool. This sometimes distracts and necessitates the presence of an assistant who helps the surgeon in handling the camera and to perform the surgery successfully. There is a possibility of errors occurring as the image produced is only 2D and can give improper images which can lead to the tremor or hand trembling of the surgeon.

This has given rise to the third generation of surgical procedures, known as the "Computer Assisted Surgery" or "robotic surgery (Figure 5-2). This technique marks several improvements such as a 3D stereoscopic vision system and related tools to simulate the natural eye-hand coordination, motion scaling (translate large movements into precise micro-movements) and improved accuracy.

Hence coupling the advantages of the above two system, we find it preferable to use a MIS assisted with Computer Aided Surgery. In such a system, the view the surgeon has of the surgical area is not ideal, and the position of surgical instruments outside of the camera view is not known. Ideally the surgeon would like to know the position and orientation of each of his instruments. Computer-aided surgery has enabled the surgeon to overlay magnetic resonance imaging (MRI) or computed axial tomography (CAT) scan images

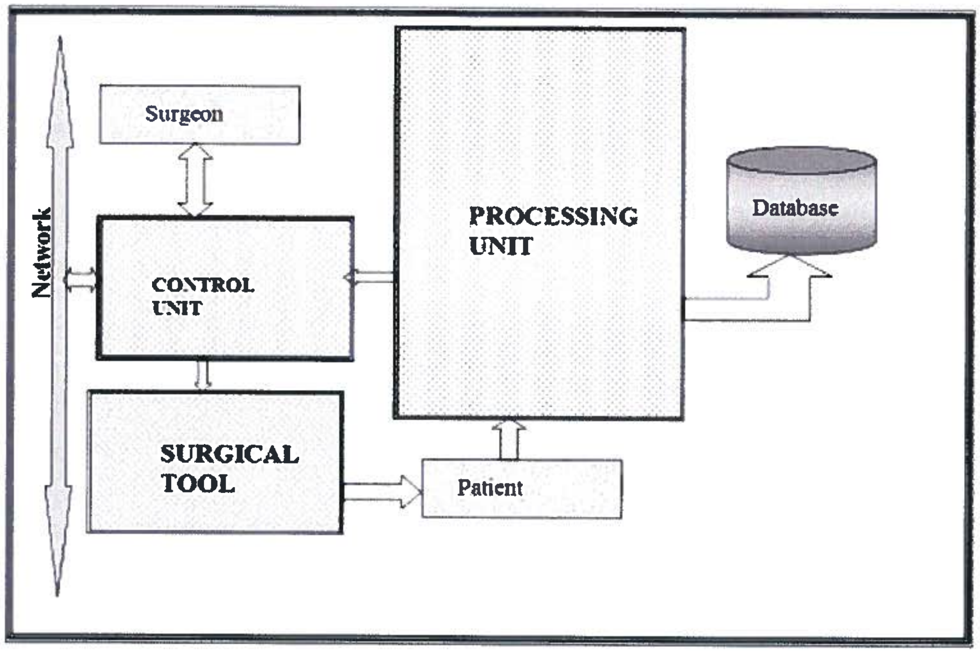


Figure 5-2. Scheme of the computer-assisted surgery scenario

of the patient with position and orientation data taken during surgery to create 3-D models which the surgeon can use to better visualize the surgical procedure. Computers can be used to simulate the procedure beforehand allowing the surgeon to practice difficult operations ahead of time [31]. One such system also called the Da Vinci system has been illustrated in Figure 5-3.

The current techniques use optical system to place markers on the ends of the surgical instruments which are located outside of the body as well as on specific locations on the patient's body. A computer registers the location of the surgical tools with the reference markers on the patient so that images of the patient's body can be aligned with the surgical tools. The images are viewed through cameras. The markers must not interfere with the surgery in any way and therefore, should be as small and lightweight as possible. While

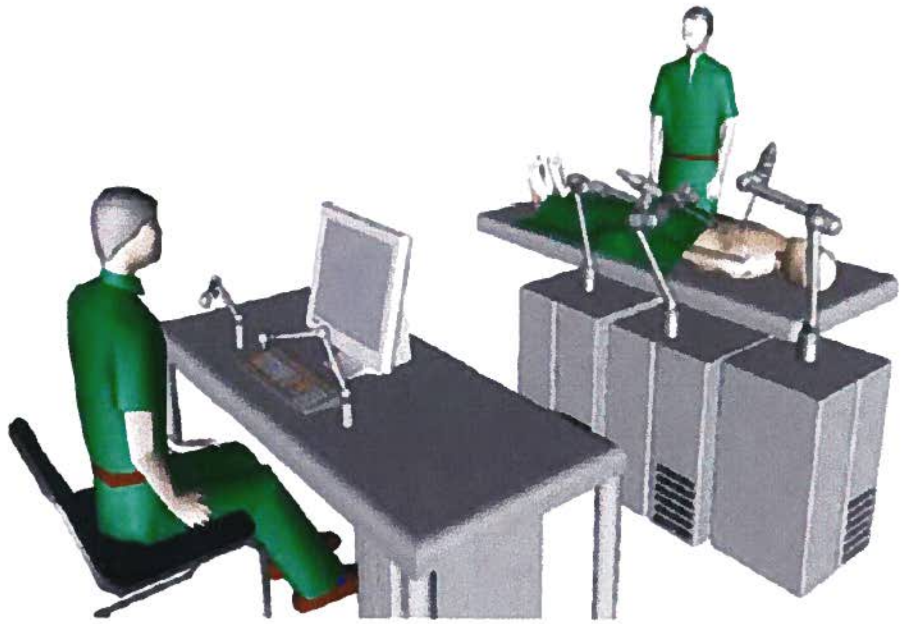

Figure 5-3. Da Vinci Surgical System for Minimally Invasive Surgery

these systems are wireless and do not have cords which can get tangled on the surgeon or on the surgical tools, there must be an unobstructed path from the markers to the camera systems. The surgeon must be careful not to block the markers himself or with other surgical instruments. Precision is compromised because the location of the surgical tips is extrapolated and does not take into account bending of the surgical tools [31]. Markers on the outside of the body do not take into account compression of the tissue. MEMS-based acoustic tracking systems have been developed to address these issues [32].

In such a kind of system, inertial sensors like accelerometers and gyroscopes are used for detecting the position and orientation of the surgical tool. The signal outputs can be integrated to determine or predict the distance travelled by a surgical tool. Conventional MEMS accelerometers have accuracies in the mg range (100-1000 times less than the acceleration due to gravity) which are not sufficient for measuring accurately the relatively small displacements made during surgery [31].Hence the main aim of this project is to design an efficient and more accurate accelerometer (micro range) based inertial navigation Unit which will enable the easy movement of the surgical tool during surgery.

To develop more accurate inertial sensors, it is essential to understand the drawbacks in the current sensors used and to modify them before they can be integrated into surgical tools. A computer-assisted system for surgery is the combination of a "smart" instrument with an embedded or external controller making use of imaging and sensing as tools to guide operation, either indirectly (by providing the surgeon with enhanced information on the anatomy or structure of the operating site) or directly (by providing the controller with such information for real-time adaptation to the environment). Hence it is very essential to have a system that guides the surgery in the most accurate method possible [31].

Additional Developments in the field of Surgery also include the developments of Catheters, Stents and guide wires. All this has led to a state of "Virtual Reality" where the surgeon can perform the entire surgery with the help of only computers and assistive robotic tools. This doesn't mean that the robots have replaced surgeons, but they only aid the surgery to take place more accurately. Further it also reduces the pressure from the surgeon so that he can be more relaxed and just concentrate on one thing at a time (i.e. manipulating the surgical tool).

Hence we can conclude that a high precision based system if developed will benefit the surgeon (the complexity in locating the affected are is minimized) and the patient (the time of surgery will be reduced) required during the navigation of the surgical tool in the body of the patient and for the surgeon to have a 3 dimensional view of the operation. One can consider the simplest inertial sensor, i.e the accelerometer for the design of such motion based a unit.Usually a conventional Micro Inertial Unit will consist of accelerometers and gyroscopes [34, 35].The accelerometer is chosen over a gyroscope in this case because it's more convenient, simpler and cheaper than a gyroscope. To enable the faster movement of the instrument, the micro-inertial measurement unit (IMU) attached to the instrument to track its position. Its local high accuracy measurement could complement the global positioning information supplied by the optical sensing system. The MEMS-based unit will comprise accelerometers together with associated electronics. The type of accelerometer chosen should provide a high sensitivity, good DC response, low drift, low temperature sensitivity, low-power dissipation, and a simple structure.

There are three types of surgical planning that involve navigation systems. One makes use of volumetric images, such as computed tomography, magnetic resonance imaging, or ultrasound echograms. Another makes use of intraoperative fluoroscopic images. The last type makes use of kinetic information about joints or morphometric information about the target bones obtained intraoperatively. Systems that involve these planning methods are called volumetric image-based navigation, fluoroscopic navigation, and imageless navigation, respectively [20].Depending on the type of the surgery, the corresponding type of navigation principle will be applied. Such kinds of devices are used in Computer Assistive Surgery (CAS).

Usually for the design of such kind of systems, the most important design factors include the proper positioning of the sensor. The sensor used can be optical or magnetic but it has been found that optical sensors are more accurate than the magnetic ones.More-oever if one uses any metallic tool, the magnetic sensor can cause disturbances and distortions in positioning.

Table 5-1. Analysis of the Present and Future Parameter Differences in MIS

| S.No | Parameters | Current System | Future System |
|---|---|---|---|
| 1 | Sensitivity | 100-200mV$g^{-1}$ | 100-200mV$g^{-1}$ |
| 2 | Frequency | 2kHz | 10kHz |
| 3 | Resolution | milli g | nano g |
| 4 | 3 DB Bandwidth | 6kHz | 6-10kHz |
| 5 | Size | 5-10 g | 10-100mg |
| 6 | Accuracy | milli range | micro range |
| 7 | Degrees of Freedom | 2 | 3-6 |
| 8 | Drift | 0.5% | 0.2-0.5% |

Once the optical waveguide source illuminates the fingers, they begin to oscillate. These then produce a vibratory motion that is detected by the accelerometers in the 3 D direction and the output is displayed. The optical sensor also gets activated and it tires to sense the position of the affected area where an incision is being made. The entire unit then travels along with the surgical instruments. This entire movement is captured by the 3D Laparoscopic Cameras and enables the surgeon to trace the progress of the surgery. Since images can be viewed continuously and the degree of freedom of the motion is about 3 or higher the accuracy and the resolution increases.

An optical camera is stationed in the operating room to receive signals from special digitized instruments equipped with light emitting diodes (LEDs). During surgery the camera receives and sends the signals to a high-speed computer. The signals are received from both the instrument (its position) and the patient (anatomy).

There are various other methods suggested in improving the trends in robotic assisted surgical system. One such example is illustrated below (Figure 5-5).

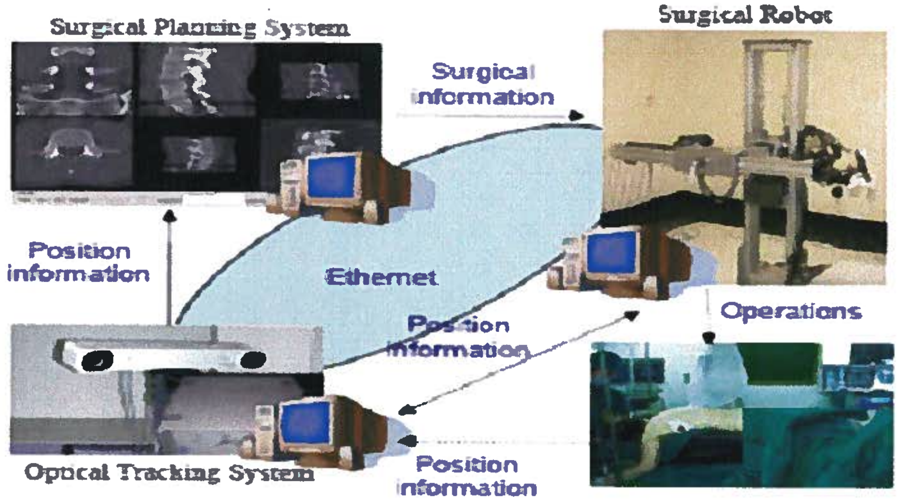


Figure 5-4. Schematic Representation of a Robotic Surgery[31]

# 6 CONCLUSION AND FUTURE WORK

Based on the results and study we can say MEMS accelerometer was designed with the following specifications.

Table 6-1. Comparison of the simulated and the Numerical values

| Characteristics | Numerical | Simulations |
|---|---|---|
| Resonant Frequency | 7.192 kHz | 8.8kHz |
| Quality Factor | 11.9 | 17.6 |
| Open loop Sensitivity | 2.12mV/g | 6mV/g |
| Pull-in Voltage | 44.29V | 72.4 |
| Release Voltage | 28.9V | 49.5 |
| Bandwidth | 604.37 Hz | 500 Hz |

When compared to the goal characteristics we find that the sensitivity of the accelerometer can still be improved. Also one method of doing so is by increasing the proof mass and a future suggested method is by having a dual mass accelerometer. Having two masses oscillate with the same amplitude increases the sensitivity of the device.

Figure 6-1 shows a simple solid model of the proposed new design. The differential concept will still remain.The only difference will be the presence of two masses. The sesing mechanism will be transverse. The degree of freedom can be increased to 2 by

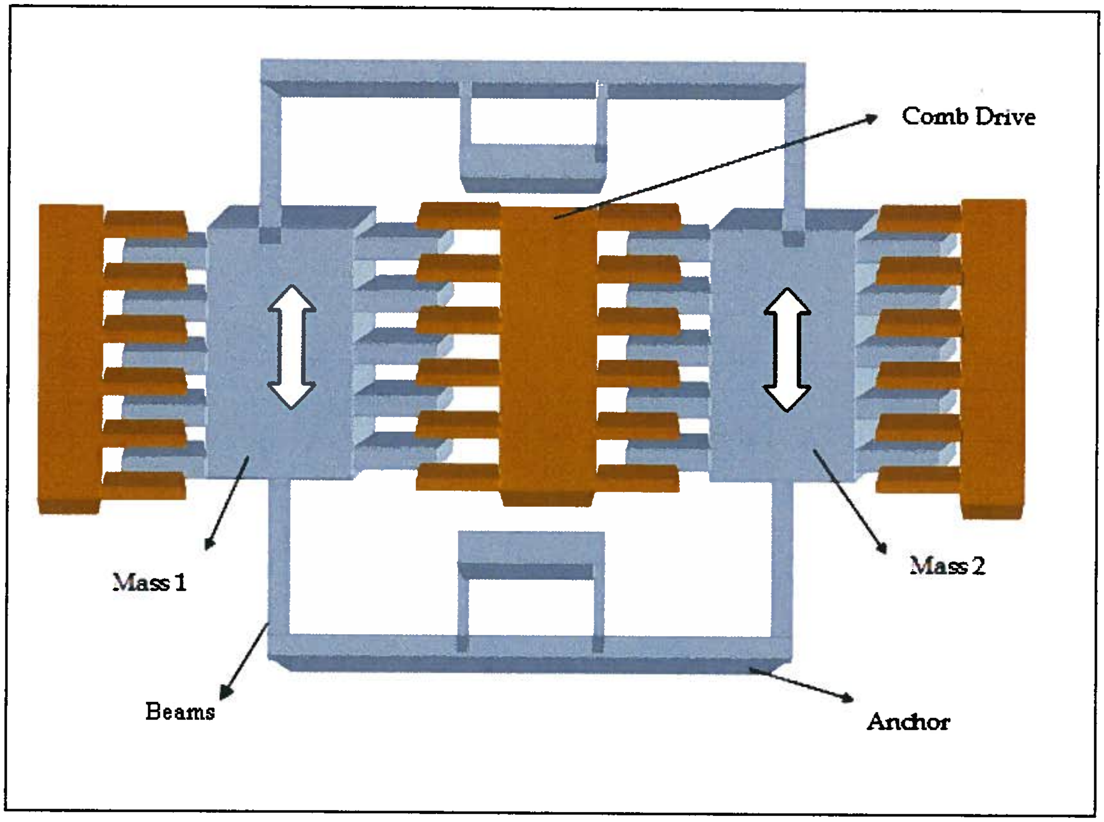


Figure 6-1. A proposed design to increase the sensitivity of the accelerometer

having the mass oscillate in 2 directions. The main advantage of such kinds of dual mass accelerometers is that it reduces the cross sensitivities and increases the sensor sensitivity with increased mass.However the non linearities of the device can increase and these have to be accounted for in the design.

## 6.1. Read Out Circuit

One of the ongoing works with respect to the accelerometer model is the design of a read out circuit for the accelerometer design.Most of the readout circuits in the literature of capacitive sensors are designed to detect changes in the voltage on the plates of the capacitor. The problem with this approach is the different sources of noise in circuits. Sources for noise include resistors and amplifiers. Noise causes the readout circuit to give false results since the output would be a combination of the noise and the actual voltage from the sensor. Depending on the type and source of noise, there are different techniques either to reduce the noise or cancel it. Still, as more and more resolution is demanded from the readout circuit, the magnitude of the noise becomes more significant and introduces higher error in the read value.

The method adapted the oscillator circuit concept to read the capacitance value. An oscillator circuit produces a periodical output signal whose frequency depends on the elements- capacitors, resistors, and inductors- in the circuit. We chose this approach because frequency measurements are one of the most accurate measurements we can make with available technology. Furthermore signal processing algorithms are becoming more and more effective.

There are many oscillator circuit configurations, they produce different periodic signals- that is a triangle, saw tooth, or square wave output- and have different components. We chose the famous 555 timer circuit for the following reasons:

- The circuit does not contain an inductor, which reduces the size of the circuit and minimizes potential interference and noise.
- It is available as an IC which produces more accurate results and it is also easily assembled and integrated.
- And the most important reason for choosing the 555 timer circuit is because it produces a square wave output, the significance of which will be explained later.

The fact that the 555 timer circuit does not include an inductor also makes the frequency of the output signal solely dependent on the capacitor, in our case it is the capacitive sensor, in the circuit. In addition the vast range of applications of the 555 timer circuit has contributed to the advancement in the accuracy of the available ICs. Finally, the fact that the 555 timer circuit produces a square wave output, when wired in the Astable circuit configuration, is significant for our project since a square wave can be easily digitized. A digitized signal is easier to work with and would allow for the use of digital signal processing algorithms which are highly advanced.

### 6.1.1. Principle of operation

Figure 6-2 shows the configuration of the Astable circuit. Since there are two sets of sensing fingers, two 555 timer circuits are used. Also this also helps in noise cancellation.Theoretically the noise in the circuit is additive in nature. Thus by using two timer circuits that are as similar as possible- so that the noise would be the same for both- we can cancel the noise.

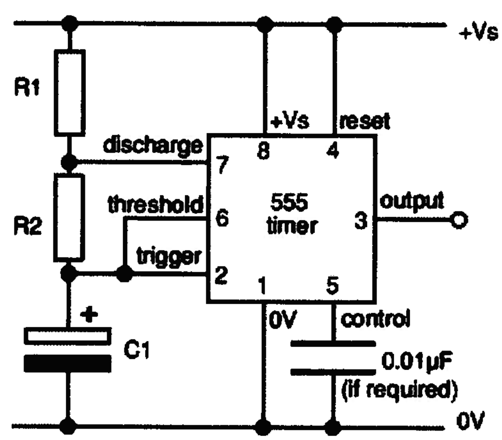


Figure 6-2. Pin Configuration of a 555 Timer

When the system is stationary, i.e. $\Delta C = 0$, the frequency of the output signal of the timer circuit, $f_0$, is:

$$f_0 = \frac{1.44}{C_1(R_1 + 2R_2)}$$

So, the timer circuits connected to $C_{1,2}$ would have the following frequencies:

$$f_{1,2} = \frac{1.44}{(C_1 \pm \Delta C)(R_1 + 2R_2)}$$

Putting the product of the two signals through a low pass filter would let only the component with low frequency, namely the  component of the product. It should be noted that the previous derivation although was for sinusoidal signals, the same concept would apply for a square wave. To measure the frequency of the component that goes through the low pass filter using the following steps the following facts should be considered:

- There is a high-speed square wave counter running with known frequency and period.
- The rising edge of the square wave from the filter is detected.
- The detection of the rising edge would set a counter to count the number of rising edges, which is equal to the number of periods, of the high speed square wave.
- The counter would stop counting when the falling edge of the square wave from the filter is detected, store the count, and reset the count to zero.
- The stored count, times the period of the high speed square wave, gives exactly one half of the period of the square wave from the filter.

Knowing the period would allow the calculation of $\Delta C$.

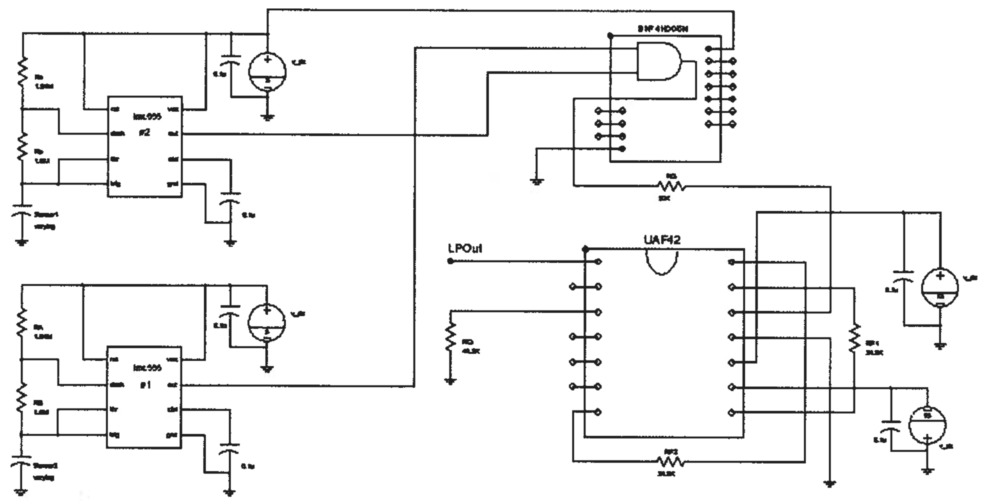


Figure 6-3. Saber Schematic of the Read Out Circuit

One other future method was to use an alternative readout method. Analog Devices manufactures a capacitance to digital converter IC. The AD 7746 is a 24 bit capacitance to digital converter and it should provide the required accuracy and resolution.

The analysis and implementation of the read out circuit is still incomplete.This is an ongoing research project which is under implementation by one of my colleagues. There is also a research project on designing gyroscopes as well. The accelerometer along with the gyroscope and the read out electronics will be a part of the IMU.

# Bibliography


[1] Chen Weiping, Huo Mingxue, Lin Yumin, Liu Xiaowei, Zhang Ruichao,"*A Novel Z-axis Capacitive Accelerometer using SOG Structure*" Proc. IEEE ,6th International Conference on Electronic Packaging ,pp. 105-107, September 2005.

[2] Stephen Beeby,Graham Ensell,Michael Kraft,Neil White," *MEMS Mechanical Sensors*", Microelectromechanical Series. Norwood,MA: ARTECH HOUSE INC. 2004,pp. 176-190.

[3] Gerold Schropferyk, Sylvain Ballandrasy, Michel de Labacheleriey, Pascal Blind and Yannick Ansel, "*Fabrication of a new highly-symmetrical, in-plane accelerometer structure by anisotropic etching of (100) silicon* ",Journal of Micromechanics and Microengineering,Vol.7,pp.71-78,June 1997.

[4] Texas Instruments ,"Accelerometers and how they work",2005. [online].Available :http://www2.usfirst.org/2005comp/Manuals/Acceler1.pdf

[5] D. L. DeVoe and A. P. Pisano, "*A fully surface-micromachined piezo-electric accelerometer,*" in Tech. Dig. 9th Int. Conf. Solid- State Sensors and Actuators (Transducers'97), Chicago, IL, June 1997, pp. 1205-1208.

[6] SB Boron, [Online].Available at http://www.sbboron.com/airbags

[7] James T.Suminto, "*A Simple High Performance Piezoresistive Accelerometer*", Tech. Digital Transducers 1991,San Francisco,pp-104.

[8] Tapani Korhonen,"*Three-dimensional Hall effect accelerometer for recording head movements of freely moving laboratory animals*"Physiology and Behavior Volume 49, Issue 3, March 1991, pp. 651-652.

[9] K.L. Phan, A. Mauritz and F.G.A. Homburg "*A Novel Elastomer Based Magnetoresistive Accelerometer*",14th International Conference on Solid-State Sensors, Actuators and Microsystems ,pp. 1479-1482,June 2007.

[10] A.M. Leung, J. Jones, E. Czyzewska, J. Chen, and B. Woods,"*Micro-machined Accelerometer based on Convection Heat Transfer*",Proc. of IEEE,11th Annual International Workshop on MEMS, pp. 627-630,Januar

1998.

[11] C. Yeh and K. Najafi, "*A low-voltage bulk-silicon tunneling based microaccelerometer*," in Tech. Dig. IEEE Int. Electron Devices Meeting (IEDM), Washington, DC, Dec. 1995, pp.593-596.

[12] N. C. Loh, M. A. Schmidt, and S. R. Manalis, "*Sub-10 cm interferometric accelerometer with nano-g resolution*," J. Microelectromech.Syst., vol. 11, pp. 182-187, June 2002.

[13] Mehmet Akif Erismis,"*MEMS Accelerometers and Gyroscopes for Inertial Measurement Units*"M.S Thesis,Middle East Technical University,September 2004.

[14] Luis Alexandre Rocha, Dynamics and Nonlinearities of the electromechanical coupling in inertial MEMS, (Ph.D.thesis),TU DELFT, Jan 2005.

[15] Xiaowei LIU , Haifeng ZHANG , Guangming LI , Weiping CHEN , Xilian WANG,"*Design of Readout Circuits Used for Micro-machined Capacitive Accelerometer*",Proc. IEEE,2nd International Conference on Nano/Micro Engineered Molecular Systems ,January 2007.

[16] Babak Vakili Amini and Farrokh Ayazi,"*A 2.5-V 14-bit ÓÄ CMOS SOI Capacitive Accelerometer*",IEEE Journal of SOLID STATE CIRCUITS, vol.39, no. 12, December 2004.

[17] S. E. Lyshevski, Mems and Nems: systems, devices and structures (CRC Press LLC, USA,2002)

[18] Matej Andrejašic,"MEMS Accelerometers" Faculty for mathematics and physics University of Ljubljana,March 2008.

[19] MEMSCAP,SOIMUMPS [online].Available :http://www.memscap.com/mumps/documents/SOIMUMPs.dr.v4.pdf

[20] Yiyi Zeng,"Design of a MEMS-based optical accelerometer with large measurable range and high sensitivity",(M.A.Sc. thesis),The University of British Columbia ,Vancouver,Canada,April 2008.

[21] Edmond Cretu,"Inertial MEMS Devices Modeling,Design and Applications",(Ph.D.thesis),TU DELFT,October 2003.

[22] Timo Veijola, *Analytical model for perforated squeeze-Film dampers*,Proceedings of DTIP 2006, Stressa, April 2006, pp 36- 41.

[23] Minhang Bao,Heng Yang," S*queeze film air damping in MEMS*", Sensors and Actuators,A136(2007) 3-27.

[24] Sarne Hutcherson and Wenjing Ye, "*On the squeeze film damping of micro-resonators in the free molecule regime*", Journal of MEMS, 14(2004) pp.1726-1733.

[25] Zoran Djuric',"*Noise Sources in Microelectromechanical Systems*",PROC. 22nd INTERNATIONAL CONFERENCE ON MICROELECTRONICS (MIEL 2000), VOL 1, NIS, SERBIA, 14-1 7 MAY, *2000.*

[26] L A Rocha, E Cretu and R FWolffenbuttel,"*Measuring and interpreting the mechanical–thermal noise spectrum in a MEMS*",JOURNAL OF MICROMECHANICS AND MICROENGINEERING,15 (2005) S30–S38.

[27] Felix.A.Levinzon, "*Fundamental Noise limit of piezoelectric Accelerometers*", IEEE Sensors, Vol.4, No.1,Feb 2004,pp 108-.111.

[28] Thomas B.Gabrielson, "*Mechanical -Thermal noise in micromechanical acoustic and vibration sensors*" ,IEEE transaction on electron devices, vol.40, No.5, May 1993

[29] Mrigank Sharma, Akila Kannan, Edmond Cretu, "*Noise-based Optimisation and Noise analysis for Resonant MEMS structures* ", Proc. of DTIP 2008 (Symposium on Design, Test, Integration and Packaging of MEMS/ MOEMS), Nice, France,9-11 April,2008.

[30] Paolo Dario, Maria Chiara Carrozza, Antonella Benvenuto and Arianna Menciassi, "*Micro-systems in biomedical applications*",Journal of Micromech. Microeng. 10 (2000), pp. 235–244, December 1999.

[31] Keith J. Rebello," *Applications of MEMS in Surgery*", Proceedings of the IEEE vol. 92, No. 1, pp. 43- 55,January 2004.

[32] Paolo Dario, Blake Hannaford, and Arianna Menciassi," *Smart Surgical Tools and Augmenting Devices, IEEE Transactions on Robotics and Automation*", VOL. 19, NO. 5, October 2003.

[33] William R. Mayfield , The heart Surgery Forum [Online]. Available http://www.hsforum.com/stories/storyReader$1418.

[34] J. H. Chen, S. C. Lee, D. B. DeBra, "*Gyroscope Free Strapdown Inertial Measurement Unit by Six Linear Accelerometers*", Joumal of Guidance, Control and Dynamics, Vo1.17, N0.2, pp. 286-290, March-April1994.

[35] W. T. Ang, P. K. Khosla, and C. N. Riviere, "*Design of All-Accelerometer Inertial Measurement Unit for Tremor Sensing in Handheld Microsurgical Instrument,"in IEEE Intl. Conf Robotics Automation*",pp. 1781-1786, Sep 2003.

# Appendix A

# First Appendix

### Simulink Model

The simulink model of the accelerometer is shown in figure 3-12 in chapter 3. The main model can be split to be consisting of 4 sub models:

A1.

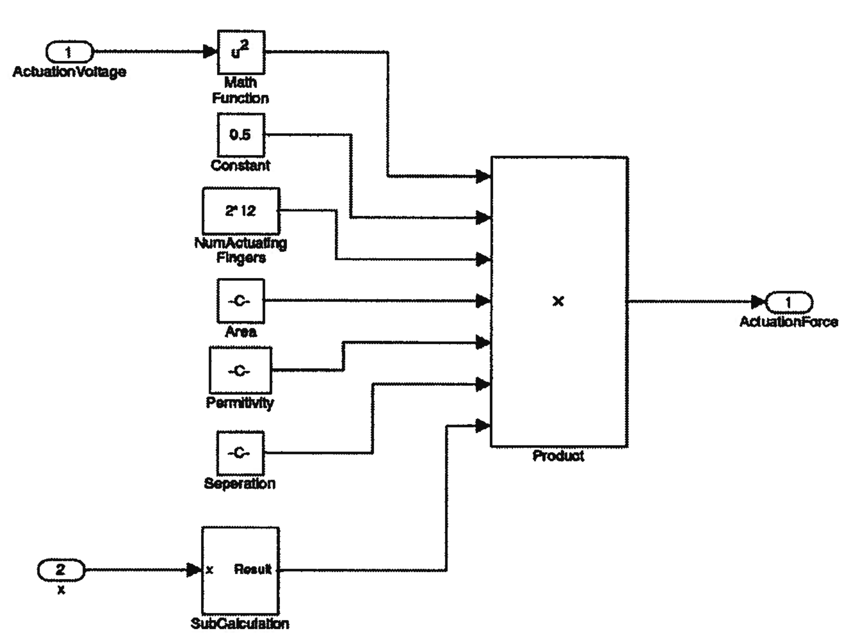


Figure 0-1. Sumulink Model to calculate the Actuation Force

A2.

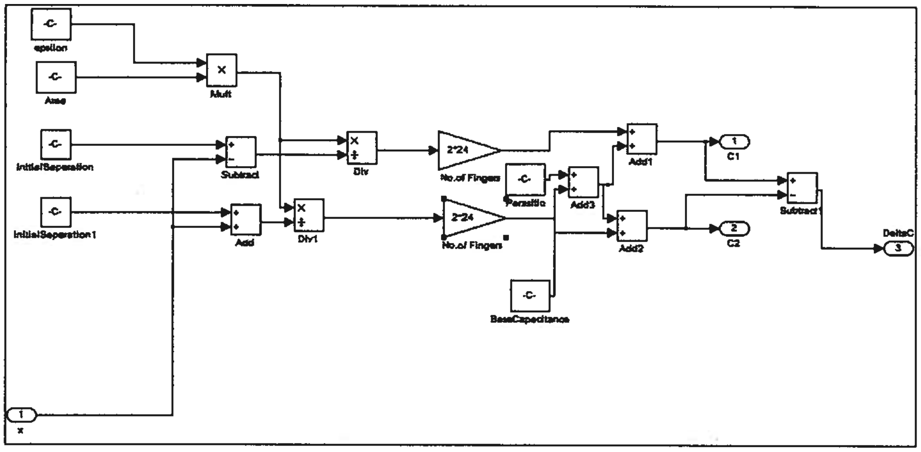


Figure 0-2. Simulink Block showing Non Linearized Capacitance Calculation

*A3.*

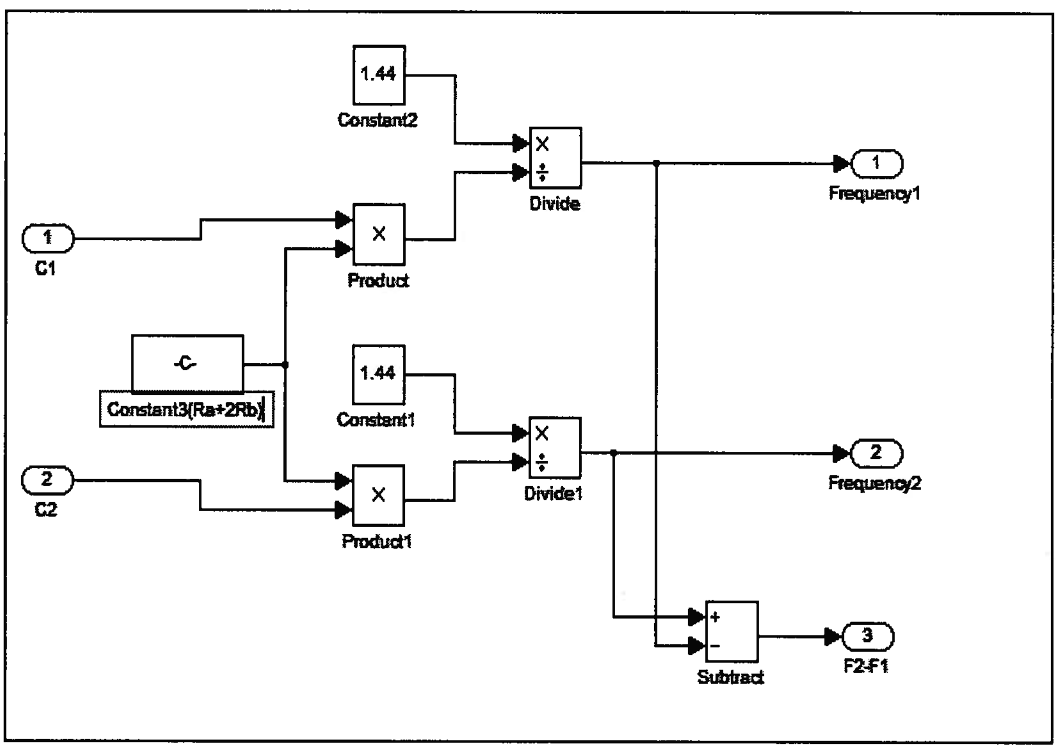


Figure 0-3. Determination of Frequency Variation

*A4.*

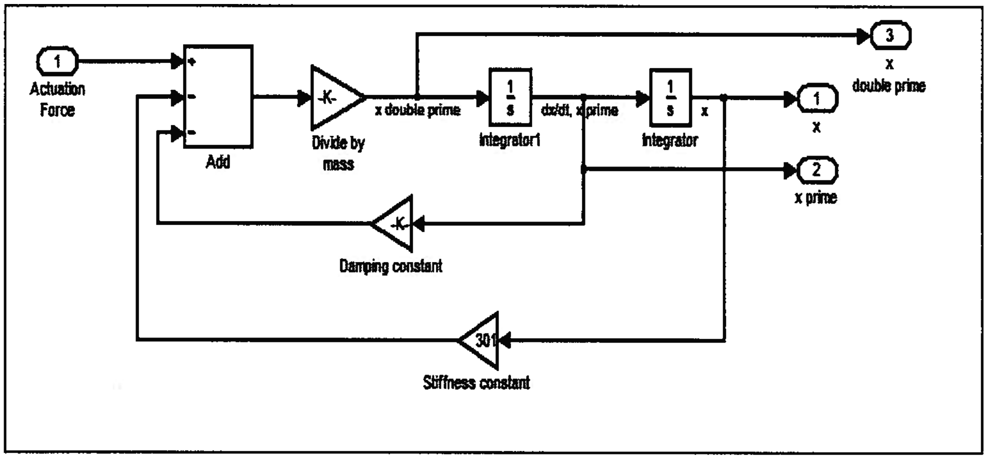


Figure 0-4. Determination of Output Acceleration